

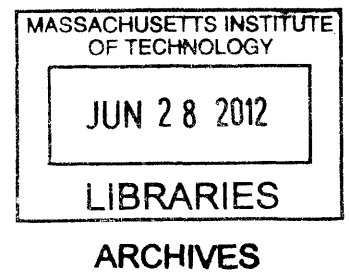
Multi-probe Robotic Positioner for Cryoablation in MRI

by  
Faye Y. Wu

B.S. Mechanical and Manufacturing Engineering (2009),  
Massachusetts Institute of Technology

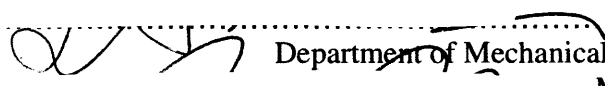
Submitted to the Department of Mechanical Engineering in Partial Fulfillment of the  
Requirements for the Degree of

Master of Science in Mechanical Engineering  
at the  
MASSACHUSETTS INSTITUTE OF TECHNOLOGY  
JUNE 2012



© 2012 Massachusetts Institute of Technology.

All rights reserved

Signature of Author.....  
 Department of Mechanical Engineering  
May 31, 2012

Certified by.....  
Dan D. Frey  
Associate Professor of Mechanical Engineering and Engineering Systems  
Thesis Supervisor

Certified by.....  
Conor James Walsh  
Research Affiliate  
Assistant Professor in Mechanical & Biomedical Engineering, Harvard University  
Thesis Co-Supervisor

Accepted by.....  
David E. Hardt  
Chairman, Department Committee on Graduate Students

**Page left intentionally blank**

# **Multi-probe Robotic Positioner for Tumor Ablation in MRI**

by

Faye Y. Wu

Submitted to the Department of Mechanical Engineering on May 31st, 2012 in Partial Fulfillment of the Requirements for the Degree of Master of Science in Mechanical Engineering

## **ABSTRACT**

This thesis describes the design of a guidance device for faster and more accurate targeting of multiple probes during cryoablation and other percutaneous interventions performed in closed bore magnetic resonance (MR) imaging systems. The device is intended to be mounted onto a Siemens 110 mm MR loop coil that rests on the patient and contains a cable driven two-degree-of-freedom spherical mechanism that orientates the intervention probes about a remote center of motion located 15 mm above the skin entry point. A carriage, pulled by strong and low stretch cables, can position up to three intervention probes as it travels on a rotating hoop. Its motion is constrained by a custom designed roller bearing to minimize friction. A thumbscrew fastened latch allows a probe to be engaged in a guide that constrains the probe along a specific trajectory. The probe can also be disengaged from its track, freeing it to move with respiration and enabling the guide to be repositioned for another probe to be inserted. Compact MR compatible piezoelectric motors are used to actuate the system. A prototype was built from 3D printed ABS plastic as a proof of concept. Bench level evaluation demonstrated that each component of the device performs according to the design specifications. The device performance was characterized by analyzing still images taken before and after movement, which yielded sub-degree accuracy, sub-degree repeatability near vertical position, and an incremental step resolution of at least 0.5 degree. Upon further developments of the registration and calibration modules in 3D slicer to interface the robot with image data, evaluation of the device in MRI will be performed.

Thesis Supervisor: Dan D. Frey, PhD

Title: Associate Professor of Mechanical Engineering and Engineering Systems

Thesis Co-Supervisor: Conor James Walsh, PhD

Title: Research Affiliate in Mechanical Engineering Department; Assistant Professor in Mechanical & Biomedical Engineering, School of Engineering and Applied Sciences, Harvard University

Page left intentionally blank

## **ACKNOWLEDGEMENTS**

I would like to thank my advisors, Professor Dan Frey and Professor Conor Walsh, for their guidance and help during my two years of Master's study at MIT.

Dr. Kemal Tuncali from the Brigham and Women's Hospital gave me a lot of clinical advice and helped me determine the functional requirements and design parameters of the device. He is also generous enough to let me scan prototypes in the AMIGO MRI scanner at BWH. Dr. Rajiv Gupta from the Mass General Hospital further provided me with important clinical feedback and allowed me to test my prototype in his CT scanner. Dr. Nobuhiko Hata and Atsushi Yamada from BWH are working on the registration module in 3D slicer to be used with my device in the near future.

I built my project upon the work of Xuefeng Chen and Steven Obiajulu, who started as UROPs at MIT.

Professor Greg Fischer, Hao Su, and Greg Cole from the WPI Automation and Interventional Medicine Lab developed the MRI compatible controller and software I am using to drive my device.

From the Wyss Institute at Harvard, Meysam Torabi basically took care of transforming the software provided by WPI into one that can be used for the project. Michael Wehner gave me a lot of inputs on mechanical design and cable drives, and he helped me with testing many components of the device. James Waver taught me how to use the Objet 3D printer and is always willing to squeeze my print job in on a short notice.

I would also like to thank Professor Alex Slocum for giving me design reviews and Dr. Barbara Hughey for lending me the Logger Pro force sensor to conduct bench level experiments with.

Everyone in my research group (Robust) at MIT, Shane Colton, Greg Tao, Lennon Rogers, Daniela Faas, Amelia Servi, Rachael Batzer, Mark Jeunnette, and Charles Guan, has given me valuable feedback, pointed me to the right person to talk to, and encouraged me to continue strive when things don't work out as expected.

Ernesto Martinez from the MIT Media Lab helped me with the cable tensioning design. Ray Browne from BCY gave me free Dyneema cables to test the device with.

Mark Belanger, Josh Dittrich from the MIT Edgerton Shop and David Dow from LMP are all wonderful resources that I relied on to manufacture the device.

Finally, the support and love from my mom, my grandma, and all of my friends really pushed me to go forward. I would not be where I am right now without them. Thank you!

Page left intentionally blank

# TABLE OF CONTENTS

ABSTRACT.....	3
ACKNOWLEDGEMENTS.....	5
TABLE OF CONTENTS.....	7
LIST OF FIGURES .....	9
LIST OF TABLES.....	18
Chapter 1 Introduction .....	19
1.1    MRI Guided Cryoablation .....	19
1.2    Motivation and Related Work.....	22
1.3    Contribution .....	27
1.4    Thesis Organization .....	27
Chapter 2 System Design Process.....	28
2.1    Robot Functional Requirements .....	28
2.2    Strategy and Concept Selection .....	31
2.2.1    Device Mounting Module.....	31
2.2.2    Probe Guidance Module .....	36
Chapter 3 Detailed Design .....	40
3.1    Low Friction Bearing.....	40
3.1.1    Bearing Design Selection.....	41
3.1.2    Detailed Bearing Design.....	45
3.1.3    Force and Movement Bench Level Evaluation.....	49
3.2    Cable Driven Actuation .....	51
3.2.1    Cable Testing and Selection.....	51
3.2.2    Cable Attachment and Tensioning.....	55
3.2.3    Hoop Detailed Design.....	59
3.2.4    System Modeling Analysis .....	63
3.2.5    Movement Bench Level Evaluation.....	66
3.3    Actuator and Encoder Selection.....	67
3.4    Base.....	71
3.4.1    MRI Coil-Mounting Design.....	71

3.4.2	Hoop Attachment .....	73
3.4.3	Actuator and Encoder Attachment .....	75
3.4.4	Registration Marker Placement.....	80
3.5	Needle Holder .....	82
3.5.1	Probe Track Design.....	82
3.5.2	Needle Preload and Release.....	85
3.5.3	Needle Holding and Releasing Bench Level Evaluation.....	86
Chapter 4	Prototyping and Control Implementation.....	88
4.1	Hardware Manufacturing .....	88
4.2	System Kinematics.....	91
4.3	Electrical Wiring and Motor Control.....	98
4.4	Final Work Flow .....	102
Chapter 5	Device Characterization and Evaluation .....	104
Chapter 6	Conclusions and Future Work.....	114
REFERENCES	.....	112
APPENDIX A	.....	115
APPENDIX B	.....	115
APPENDIX C	.....	115



## LIST OF FIGURES

Figure 1-1 Current work flow for cryoablation procedure.....	22
Figure 0-2 Large MRI compatible devices for positioning probes. Left: InnoMotion pneumatic robot from Innomedic [9]. Middle: The light puncture robot (LPR) is attached to a frame that rests over the patient [10]. Right: MR-guided microwave thermoablation device [11]. These devices are not designed to place multiple probes.....	24
Figure 0-3 Robopsy has a small footprint and can actively rely the angle required for the device from the medical image software. This device is CT compatible and can place a single probe [12].....	24
Figure 0-4 MRI compatible robots designed for specific usage. Left: Mr. Bot from John Hopkins contains interchangeable end effector, allowing it to perform various interventions related to transperineal prostate procedures [13]. Middle: MRI compatible device for treating prostate brachytherapy developed at WPI is driven with custom built MRI compatible motor controller [14]. Right: Robot designed at University of Minnesota for breast biopsy uses telescopic rods to actuate movement while keeping ultrasonic motor away from imaging bore.....	26
Figure 0-5 Passive MRI compatible device. Left: Small footprint plastic device that uses thumb screw tightened flexure to hold and release multiple probes [16]. Middle: SeeStar device can sit on the patient and support a single biopsy needle [source <a href="http://www.apriomed.com">http://www.apriomed.com</a> ]. Right: Simplify is a needle support device similar to SeeStar but employs a different mechanism [source <a href="http://www.neorad.no">http://www.neorad.no</a> ].....	27
Figure 2-1 MR imaging coil must be placed on top of patient prior to scanning in order to produce useful data for diagnosis and interventional procedures [ <a href="http://www.siemens.com">http://www.siemens.com</a> ].....	30
Figure 2-2 Initial strategies of device mounting module. (1) Mounting the device to the patient. (2) Mounting the device to the MRI bed. (3) Mounting the device to a large rectangular MRI imaging coil. (4) Mounting the device to a frame outside of the MRI [16].....	33

Figure 2-3 Device mounting module concepts. (1) Concept 1 uses a belt to wrap the device on the patient. Telescoping legs resting on the bed would provide extra stability. (2) Concept 2 attaches to the side of MRI bed and can accommodate for patient size/cancer location with a telescoping arm. (3) Concept 3 also connects to MRI bed, with curved telescoping arm to provide reach and structural support. (4) Concept 4 secures the device and imaging coil with a belt or pre-curved plastic.....34

Figure 2-4 Bench level prototype of the device mounting module. Left: The prototype is made of two curved stainless steel bands and a sheet of ABS. Middle: The flexible band naturally wraps around the body and can rigidly support the device (acrylic model). Right: Side view of the prototype.....35

Figure 2-5 Device is designed to accommodate a large 4-channel Flex Loop Interface (loop coil). Left: Loop coil from Siemens is small and contains a large window in the middle [<http://www.siemens.com>]. Right: Example design to allow attachment of the device to the loop coil (device is shown in transparent green).....36

Figure 2-6 Probe guidance module concepts. (1) Concept 1 is the classical 2 bar-3 joint linkages design. An end effector on the tip of the free end of the linkage holds the probe in place (2) Concept 2 has half of a circular arm that spins about the base. The end effector would be clamped on the arm and slide along it, providing the second degree of freedom. (3) Concept 3 is the full circular arm version of concept 2. (4) Concept 4 is a pivoting hoop, also with the end effector sliding on top of the hoop.....38

Figure 2-7 A rough sketch of the device incorporating both design modules. The base (green) would cover the loop coil and contain registration markers. The pivoting hoop and carriage would provide the 2 DOF motion needed to orient ablation probes.....39

Figure 3-1 Simple device model which defines the angle between the centerline of the carriage and the hoop as  $\theta$ .....42

Figure 3-2 Vee groove roller bearing design. Four rollers are required to kinematically constrain the bearing.....42

Figure 3-3 Roller coaster type bearing design would require 6 to 8 rollers to constrain bearing motion properly.....43

Figure 3-4 Bearing riding on a triangular prism would require a minimum of 3 rollers.....43

Figure 3-5 Bench level prototype of roller bearing riding on triangular prism. Left: A model of the three-roller bearing design was made, with a straight triangular prism substituting for the hoop. Right: A model of the bearing was made to fit on a curved triangular prism. Even though the bearing is kinematically constrained, the bearing tends to pivot to the side.....44

Figure 3-6 Roller bearing design incorporated into the carriage. Left: CAD of the completed carriage. Right: cross section view of the carriage riding on the hoop that contains a triangular profile (red).....45

Figure 3-7 Top view of the carriage riding on the hoop. The rollers are positioned to evenly distribute force, constrain the motion of the bearing, and avoid jamming.....46

Figure 3-8 FEA result of the carriage. The maximum stress in the carriage is 128 KPa and the deformation in the holes is about 0.58  $\mu\text{m}$ .....47

Figure 3-9 Hertz Contact Stress plotted as a function of  $n$ , where  $n$  is the ratio between the depth below contact area and the half width of the contact area.....49

Figure 3-10 Bench level test of the roller bearing with Logger Pro force sensor.....50

Figure 3-11 Example plot of the bench level test for the bearing prototype. A maximum force of 2.71 N was measured, with a standard deviation of 0.011 N.....50

Figure 3-12 Kevlar, Dyneema, and Nylon cables are stretched in the Instron Advanced Mechanical Testing System. Dyneema exhibited high yielding strength and low stretch, ideal for the MRI compatible cable driven system.....52

Figure 3-13 Bench level creep test was conducted on Dyneema cable over the course of three days.....53

Figure 3-14 Bench level experiment was conducted to measure the coefficient of friction between the Dyneema cable and a 3D printed part.....54

Figure 3-15 Force measured with Logger Pro to calculate the coefficient of friction between the Dyneema cable and a 3D printed part. With an average of 12 N, the coefficient is calculated to be about 0.57.....55

Figure 3-16 Schematics of the cable drive system.....55

Figure 3-17 Driving pulley contains two layers, separating the outgoing and incoming cables to decrease friction.....56

Figure 3-18 A knot-in-hole design allows for the slippery Dyneema cable to be attached to the carriage and the driving pulley.....57

Figure 3-19 FEA result of driving pulley. The maximum stress is about 4.8 MPa and maximum deflection is 0.002  $\mu\text{m}$ .....58

Figure 3-20 The cable tensioning mechanism uses a bolt to finely control movement of the tensioning pulley, which is held in a plastic holder with a dowel pin. Left: Top view of the mechanism. Right: Side view of the mechanism .....58

Figure 3-21 Hoop Design. Left: The hoop has a pocket for attaching the driving pulley on the right leg, a pocket to attach the hoop hub on the left leg, and a pocket for the cable tensioning mechanism. Right: Hoop dimensions .....60

Figure 3-22 Hub side of the hoop. Left: The hoop has a triangular cross section, with the tips flattened to minimize material usage. Right: The hoop contains a rectangular pocket to hold the tensioning mechanism. An aluminum hub is designed to interface with the hoop for better alignment and support.....61

Fig 3-23 Cable groove design on the driving pulley side of the hoop. Left: The leg contains a pocket for positing the driving pulley and two grooves of different depths that span outward. Middle: Cross section view of the leg, where the shallow cable groove aligns with the upper notch in the double pulley. Right: Cross section view of the leg, where the deeper cable groove aligns with the lower notch in the double pulley.....62

Figure 3-24 FEA result of the hoop under 10 N of load from probe insertion. The max stress calculated is 1.86 MPa, and the max deflection is 0.054 mm.....62

Figure 3-25 Free Body Diagram of the cable drive system.....63

Figure 3-26 Minimum torque required to move the cable system as the carriage moves along the hoop.....66

Figure 3-27 Bench level test was conducted on a large scale hoop and carriage model. The actuated movement exhibited no backlash and required relatively low force.....67

Figure 3-28 Non-magnetic actuators. Left: Shinsei ultrasonic motor. Right: LEGS rotatory piezoelectric motor.....70

Figure 3-29 Encoder module from US Digital is used with the piezoelectric motor to perform closed loop position control. Left: Optical Encoder module. Middle: 1” diameter encoder disk. Right: Incremental differential encoder cable driver.....71

Figure 3-30 The device contains a thin walled base and mounts onto a loop coil. Here, the device is shown mounted on top of an imaging phantom.....72

Figure 3-31 Anchors on the side of the base are designed for attaching the robot to patient.....72

Figure 3-32 FEA analysis of the anchors on the base. Maximum stress is found to be 1.9 MPa, and the maximum deflection is 0.018 mm.....73

Figure 3-33 The hoop attachment features. Right: The hoop is attached to the base via flexure fingers around a cylindrical hole. The rectangular platform constrains the hoop axially. Middle: Left leg attachment. Right: Right leg attachment.....74

Figure 3-34 FEA conducted on the hoop attachment components. The maximum stress caused by needle insertion force on the bottom of the mating feature is about 222 KPa. The maximum deflection is about 0.006 mm. The maximum stress caused by the snapping fit in the finger is 4.64 MPa and the max deflection is 0.018 mm.....75

Figure 3-35 The assembly and attachment of electronic components on the base. The motor attaches to a removable casing and the shaft is extended with a flexible coupling. Encoder module is subsequently mounted on the extension shaft, with the other end of the shaft connect to the hoop or the driving pulley.....76

Figure 3-36 Misalignment clamp on coupling is used to connect an extension shaft to the motor shaft [<http://www.mcmaster.com>]. This type of coupling holds onto a shaft with integral clamp and won’t damage the shafts like a set screw.....76

Figure 3-37 Slots for encoder disk and misalignment coupling are made on the rectangular platform to provide clearance for the parts to rotate without interference....77

Figure 3-38 The encoder has very rigid geometric attachment constrains. The disk must be placed a maximum 0.025” away from the inner edge of the encoder module [28].....78

Figure 3-39 PinPoint Fiducial marker used for registration. Left: The fiducial shines brightly in MR image to work as registration markers. Right: The 6 mm spherical marker from Beekley [<http://www.beekley.com>].....80

Figure 3-40 Fiducial marker placements in the base. Fiducial placed between the top layer and the middle layer is illustrated in solid lines and fiducial between the middle layer and the bottom layer is indicated with dotted lines. The distance between any two points is unique, enable registration algorithm to pick up the position and orientation of the device.....81

Figure 3-41 A prototype base embedded with registration markers as tested in MRI and CT to obtain images for analyzing registration algorithm and implementing the registration module into medical imaging software. Left: MRI scan. Right: CT scan.....81

Figure 3-42 Probes are positioned to allow insertion along the incision.....82

Figure 3-43 There are three tracks on the carriage separating the probes in order to prevent them from intersecting or colliding. A thumbscrew and latch combination is used to preload and lock the probe in place.....83

Figure 3-44 Two designs to align the needle tracks with the remote center of motion. Left: The hoop is bent so the carriage wall holding the probe coincides with the x-z plane. Right: Needle tracks point radially inward to keep a straight hoop profile. For simpler hoop design, the tilted need track idea was selected.....84

Figure 3-45 The cross sectional area of a needle (or needle track) changes as the needle rotates.....85

Figure 3-46 Needle release and preload mechanism. Left: The latch contains bumps to preload the needles in the holder. Right: Once the latch is opened, the probes are released simply by actuating the carriage to the next position.....86

Figure 3-47 Probe holding and releasing test proved that the needle holder can keep the probe in place, guide its trajectory, and free it from restriction when insertion is completed. Left: Close up view of needle holder and the probe. Right: Probe held in place by needle holder.....87

Figure 4-1 Cables are attached to both sides of the top carriage wall with double figure-eight-knot locked in 90 deg holes. The knot is on the vertical wall of the bearing, allowing most of the force of the cable to transmit to the direction of the carriage's motion.....90

Figure 4-2 3D printed prototype of the device.....91

Figure 4-3 A model of the two degree of freedom spherical mechanism. (a) The arc rotates by an angle of  $q_1$  and (b) the carriage rotates by an angle of  $q_2$ .....92

Figure 4-4 Device coordinate system. X-axis is along the center of the motor shaft. Y-axis is along the direction of the base anchors. Z-axis points up vertically.....92

Figure 4-5 Angle compensation for probes placed in other tracks.....94

Figure 4-6 Close up of angle compensation. The carriage needs to rotate backward by  $\delta q_2$  in this case to account for track shift.....95

Figure 4-7 Parasitic motion of the carriage during hoop movement is caused by cable passively wrapping on the driving pulley.....96

Figure 4-8 The largest probe insertion angle,  $\beta$ , would occur when the target is at the top edge of the lesion.....97

Figure 4-9 Block diagram of system architecture.....99

Figure 4-10 Screen shot of the registration and calibration module inside of 3D slicer to work with the robot. It is currently being developed at BWH.....100

Figure 4-11 MRI Compatible controller set up and electrical connection to motor. Left: The controller (black box) is equipped to run 5 sets of motor/encoder combo independently. The interface box (blue) can receive image data from another computer running 3D slicer. It then runs the Java software to convert target points into motor angles and sends command to the controller to actuate the motor and read encoder data. Right: the motors and encoders are plugged into a PCB board that interfaces with the controller.....100

Figure 4-12 Java user interface for converting target points into motor angle and monitoring robot movement.....101

Figure 4-13 The encoder cable needs to be rewired to interface with the PCB board of the controller. Left: Pin output of the encoder differential driver [<http://www.usdigital.com>]. Right: PCB layout, M for motor input pins, and E for encoder input pins.....101

Figure 4-14 Close up view of the robot with electrical wiring in place.....102

Figure 5-1 2D images taken with digital camera were used to evaluate the performance of the device. Left: Schematic of the test set up. Right: A digital camera is placed approximately 4 ft. away and zoomed on the robot for least 3D effects in the image. Markers are put on the robot for tracking purposes.....104

Figure 5-2 Image J was used to analyze the picture took with camera to determine the actual angle of the device has moved.....	105
Figure 5-3 Accuracy test result of the hoop movement. Both the encoder and camera data are compared with the command angle.....	106
Figure 5-4 Accuracy test result of the carriage movement.....	106
Figure 5-5 A rotation error in the hoop and the carriage would cause a large error in the probe tip.....	108
Figure 5-6 Hoop movement repeatability test.....	110
Figure 5-7 Carriage movement repeatability test.....	111
Figure 5-7 Hoop movement resolution test.....	114
Figure 5-8 Carriage movement resolution test.....	114
Figure A-1 Plane contact sliding bearing bench level test.....	120
Figure A-2 Redesign of the plane contact sliding bearing to allow for more adjustments in the bearing wall position and preload the bearing to desired stiffness.....	121
Figure A-3 Ball placement for point contact sliding bearing.....	122
Figure A-4 Cross sectional view of the point contact sliding bearing. Nylon balls are imbedded into the bearing walls to provide the point contact needed.....	123
Figure A-5 A non-recirculating ball bearing utilizes Vee and flat grooves to constrain its motion [32].....	124
Figure A-6 In a non-recirculating ball bearing, the balls and the retainer would move half the distance of the total travel [32].....	125
Figure A-7 Prototype non-recirculating bearings, preloaded with bolts and springs. A piece of aluminum sheet metal serves as retainer for the glass balls. Left: Bearing machined out of Delrin. Right: 3D printed bearing of similar dimension.....	126
Figure A-8 Bench level set up to test the force required to move the Delrin non-recirculating ball bearing.....	127
Figure A-9 Example force measurement of the Delrin non-recirculating ball bearing. Average force required to move the bearing is 3.64 N, with a maximum measurement of 4.43 N.....	127



Figure A-10 Example force measurement of the 3D printed non-recirculating ball bearing. Average force required to move the bearing is 2.65 N, with a maximum measurement of 3.1 N.....128

Figure A-11 Force test of the non-recirculation ball bearing on a curved hoop with an Advanced Mechanical Testing System from Instron.....129

Figure A-12 Example force measurement of the non-recirculating ball bearing. A total of 10 trials were conducted and the average force was 12.5 N.....130

## **LIST OF TABLES**

Table 2-1 Pugh Chart for device mounting module strategy evaluation.....	33
Table 2-2 Pugh Chart for device mounting module concept evaluation.....	35
Table 2-3 Pros and cons of probe the positioning strategies.....	37
Table 2-4 Pugh Chart for probe guidance module concept evaluation.....	38
Table 3-1 Dyneema cable Creep test result.....	53
Table 3-2 Comparing specifications between actuators from Shinsei and Piezomotor....	70
Table 5-1 Encoder accuracy results.....	107
Table 5-2 Accuracy test results.....	107
Table 5-3 Probe tip error.....	109
Table 5-4 Hoop repeatability test results.....	111
Table 5-5 Carriage repeatability test results.....	112
Table 5-6 Hoop movement resolution test result.....	113
Table 5-7 Carriage movement resolution test result.....	113

# Chapter 1

## Introduction

### 1.1 MRI Guided Cryoablation

Percutaneous procedure, such as biopsy and ablation, can be used to diagnose and treat cancer. It is minimally invasive, requiring only a small incision for needle insertion. It is simple to operate, needing only to place probes in a tumor. Furthermore, it has a fast recovery time, allowing patients to be discharged either the same day or the day after the procedure. To ensure the accurate placement of probes, a percutaneous procedure is usually performed with image guidance provided by Computed Tomography (CT), Ultrasound, or Magnetic Resonance Imaging (MRI). Due to its high soft tissue contrast and lack of harmful radiation, MRI has the potential to more effectively guide and monitor interventions.

Cryoablation is one of the interventions that can be used in conjunction with MRI to treat lesions. Unlike other thermal ablation treatments, cryoablation can be monitored with MRI in real time without compromising the image quality of the scan [1]. This procedure involves controlled freezing of tissue by pumping cryogen into ablation probes. Intracellular ice formation in the vicinity of the probe tip induces cell trauma, disrupts cellular metabolism, coagulates blood, and ultimately results in cell death. The damage caused by freezing is not cancer specific; however, ablating all of the surrounding tissue and blood vessels has shown to help eradicate cancer due to inadequate blood supply in the affected area [2]. Cryoablation is traditionally performed

with liquid Nitrogen filled probes that are as large as 6 mm in diameter. The recent development of smaller gauge probes that utilize pressurized Argon gas, which can cool to temperatures as low as  $-140^{\circ}\text{C}$ , allowed this procedure to truly become minimally invasive. A freeze-thaw-freeze cycle, where Helium gas is pumped into the probe for a short period of time between two long intervals of freezing treatment, must be used to reduce undesirable damage and ensure local tumor necrosis [3].

Visualization of the ice ball in MR images allows for direct comparison between the kill zone and the tumor margin, helping to ensure that the ice ball covers the whole affected area without encroaching on critical anatomy. Multiple probes may be placed at the same time, which produces an ice ball of larger volume than all the ice balls from individual probes combined, more effectively treating lesion of larger sizes.

Common applications of cryoablation include treating solid tumors found in the lung, liver, breast, kidney and prostate [4]. Recent interventional cryoablation studies have reported near 100 percent efficacy for kidney tumors up to 4 cm [5, 6]. Larger localized tumors would require more than one treatment, and, with a recurrence rate of 6%-10% in tumors of 8 cm, may be more suitably treated with surgery or radio frequency ablation [5, 7].

The current work flow of a MR image guided cryoablation is very tedious and inefficient, as illustrated in Figure 1-1. After using an initial MR scan to determine the location of a lesion, interventionist would approximate a probe entry site on the surface of the skin. A fiducial capsule, readily visible as a signal void on MR images, is then placed on the approximate entry point. A MR image coil, used to improve image quality, is strapped to the patient, with the fiducial capsule exposed at the center of one of the coil

windows. Another scan verifies the location of the fiducial capsule. If necessary, the fiducial capsule and the MRI coil are moved at this point to fine tune the probe entry site. A mark is made on the patient where the entry point is finalized. The capsule is then removed and the patient is prepared and draped in a sterile fashion. After injecting local anesthesia, a small incision about 5-6 mm long is made at the entry site, and clamps are used to open the cut further. An ablation probe is initially inserted through the entry site to a depth of about 60 mm to provide enough clearance between the probe handle and the imaging bore. The probe trajectory is checked with MR imaging and further insertion is made. Many small adjustments of the probe trajectory, while checking with MR image scans, are needed before the tip reaches the desired end point inside of the patient. Depending on the size and location of the lesion, multiple probes may be placed in this fashion. Finally, a local freezing of tissue surrounding the probe obliterates the lesion and completes the treatment.

A typical cryoablation procedure as described above takes about 2.5 to 3.5 hours to complete and half of the procedure time may be spent correcting the probe path [8]. Especially when the procedure is performed in a closed MRI where patients need to be taken out of the imaging bore for probe trajectory adjustment, a task as simple as inserting a probe along its planned trajectory becomes the most labor-intensive portion of the procedure. This process of placing probes by hand is fatiguing for the interventionist, wastes hospital resources, and may increase the risks to patients due to their prolonged exposure to anesthesia.

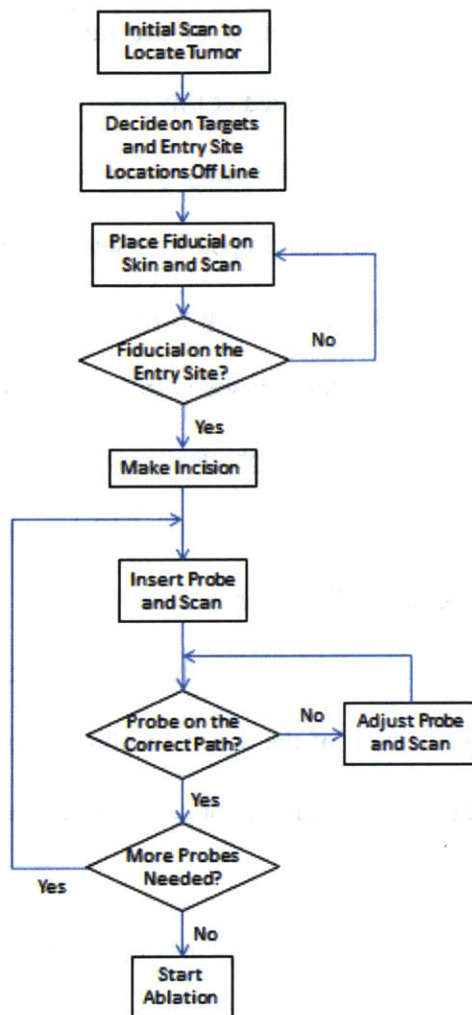


Figure 1-1 Current work flow for cryoablation procedure.

## 1.2 Motivation and Related Work

To solve the probe positioning problem, a number of devices have been developed in recent years for image guided percutaneous interventions. InnoMotion from Innomedic (Herxheim, Germany) is compatible with both MRI and CT [9]. The robotic system, as shown in Figure 1-2 (Left), attaches to a rigid arch that mounts to the scanner bed and extends over the patient. The arch angle allows the robot to be passively positioned at 0, 30, and 60 degrees to vertical, situating the robot close to the region of interest. Due to

RF noise and inductive heating of the electric power lines, the piezoelectric drives failed to work inside of MRI and were replaced with pneumatic cylinders instead. Software was developed for this system to integrate with image data and register the device. The probe is inserted manually without real-time tip tracking, which would hinder target accuracy and prolong operation time.

Another bed mounted device is the Light Puncture Robot (LPR) being developed in Grenoble [10]. This machine (Figure 2-2, Middle) rests upon the patient and straps to a frame on the bed. The position of the LPR with respect to the probe entry point is adjusted with the two translational motions of the frame. A sprocket set up transforms linear motion of pneumatic pistons into the three degree of freedom (DOF) rotary motion of end effector, which orients and inserts intervention probe. The LPR operates in both MRI and CT; but, without implementing a probe release mechanism, it can only guide the trajectory of a single probe.

Hata et. al. from the Brigham and Women's Hospital (BWH) reported a semi-active needle-guiding robot for MR-guided microwave thermoablation of liver tumor [11]. This device (Figure 2-2, Right) is mounted to the side of the scanner. It contains an active 2 DOF base stage and a passive needle holder with two unconstrained rotations. When the surgeon manually orients the needle to a desired direction, fiber optic encoders would measure this movement and actuate the base stage, driven by ultrasonic motors, to maintain the remote center of motion at the pre-defined tumor site. With the ultrasonic motors outside of the imaging bore, the robot can operate safely in MRI and achieve an average error of 0.7 ~ 0.3 mm at the needle tip. Just like the LPR, this semi-active robot also lacks the capability of placing multiple needles at the same time.

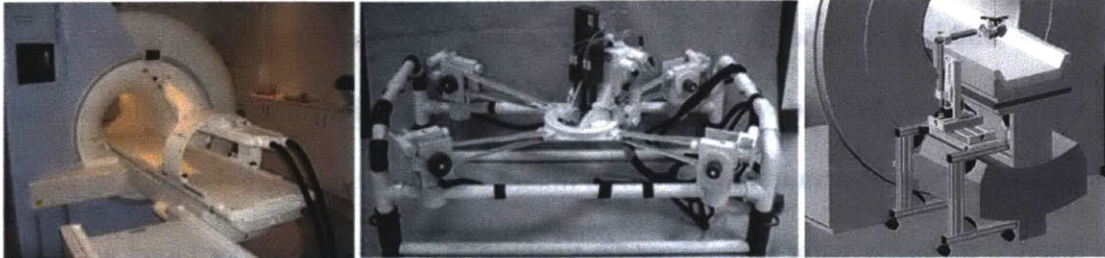


Figure 0-2 Large MRI compatible devices for positioning probes. Left: InnoMotion pneumatic robot from Innomedic [9]. Middle: The light puncture robot (LPR) is attached to a frame that rests over the patient [10]. Right: MR-guided microwave thermoablation device [11]. These devices are not designed to place multiple probes.

As opposed to large and expensive mechanisms hovering over the patient, Robopsy developed at MIT is an example of compact and inexpensive interventional robot [12]. As shown in Figure 1-3, the spherical mechanism contains a pair of concentric and cross-nested hoops to orientate the probe. A frictional drive, which rides on top of the hoops, is used to grip, insert, and release the probe, minimizing tissue laceration due to the patient's breathing. The device attaches directly to the patient via an adhesive pad and allows the whole robot to move passively with the patient's body, further preventing injury caused by inadvertent movement. Robopsy is designed to position a single probe. The device is actuated with four micro-motors and is thus limited to perform CT and Ultrasound image guided biopsy.

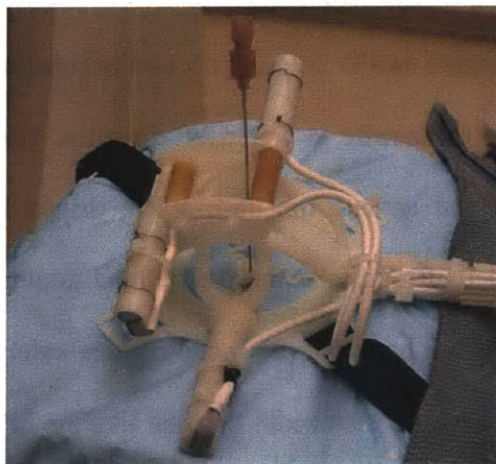


Figure 0-3 Robopsy has a small footage and can actively rely the angle required for the device from the medical image software. This device is CT compatible and can place a single probe [12].



For more specific applications, John Hopkins presented a fully automated MrBot (Figure 1-4, Left) to be compatible with all known types of imaging equipment [13]. Although it is only for transperineal prostate procedures, the interchangeable end effector enables the robot to perform various interventions, such as biopsy, serum injection, and brachytherapy. All components in the imaging room are electricity free: custom designed pneumatic stepper motors are used to drive MrBot, while fiber optic encoders send feedback to the controller box installed outside.

WPI has built a robot for the same targeted form of treatment [14]. In this case, MRI compatible piezoelectric motors actuate a six DOF probe placement mechanism (Figure 1-4, Middle), in addition to probe steering, for prostate brachytherapy. With a custom built MRI compatible controller, the device exhibited less than 2% signal to noise ratio (SNR) loss in a closed 3T MRI scanner, allowing the probe movement to be controlled and measured in MR image in real time.

University of Minnesota designed a system (Figure 1-4, Right) for breast biopsy and intervention under MR guidance [15]. It stabilizes the breast with compression and uses five telescopic rods to situate probes, keeping the ultrasonic actuators away from the imaging bore. Although the apparatus is able to place a probe in less than 50 s with sub-millimeter repeatability, when the target is more than 40 mm away from the rotation axis of the device, backlash in the rotating joints could incur errors of up to 5 mm at the tip. The three devices described above are designed for procedures that only require one probe, thus being able to release and position multiple probes was not part of the design functional requirement.

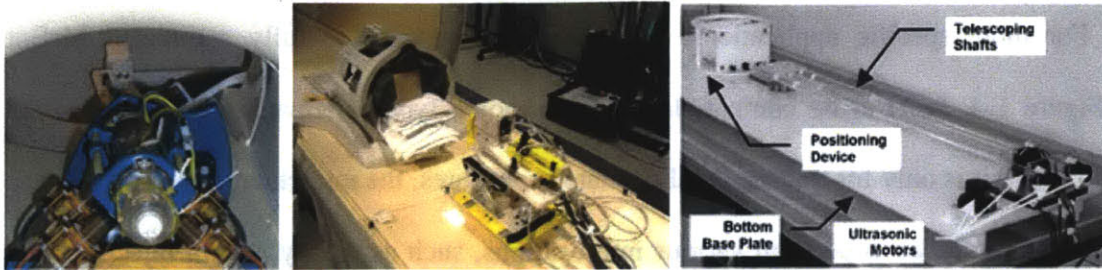


Figure 0-4 MRI compatible robots designed for single probe placement. Left: Mr. Bot from John Hopkins contains interchangeable end effector, allowing it to perform various interventions related to transperineal prostate procedures [13]. Middle: MRI compatible device for treating prostate brachytherapy developed at WPI. It is driven with a custom built MRI compatible motor controller [14]. Right: Robot designed at University of Minnesota for breast biopsy uses telescopic rods to actuate movement while keeping ultrasonic motor away from imaging bore [15].

A fully passive MRI compatible probe positioner was designed by Xuefeng Chen at MIT [16]. This device, shown in Figure 1-5 (Left), was completely made of 3D printed plastic, containing a half arc rotating on a circular base. The needle holder secures the probe with a flexure and releases the probe when a thumb screw is loosened. This system is designed to place multiple probes; however it is passive and did not actively control the pivoting angle of the probe. Other passive probe positioning systems, such as SeeStar from AprioMed (Londonderry, NH) and Simplify from NeoRad (Oslo, Norway), use two hoops to pivot a single biopsy needle (Figure 1-5, Middle and Right). While these systems offer needle support and are made of MRI compatible plastic, they are not linked to any imaging software. Physicians are still required to do the mental conversion between medical image and needle orientation. The alignment of probes is also performed manually in an iterative manner.

In summary, many devices for positioning and orientating interventional probes either are too large and expensive for clinical use, or, being passive, offered minimal assistance. Existing MRI compatible robots are mostly designed for specific procedures that would require single probe placement, while other more general designs can only operate in CT.



Figure 0-5 Passive MRI compatible device. Left: Small footprint plastic device that uses thumb screw tightened flexure to hold and release multiple probes [16]. Middle: SeeStar device can sit on the patient and support a single biopsy needle [source <http://www.apriomed.com>]. Right: Simplify is a needle support device similar to SeeStar but employs a different mechanism [source <http://www.neorad.no>].

### 1.3 Contribution

In view of the advantages and problems associated with available technologies for placing probes, there lies a clear need for an inexpensive, small footprint MRI-compatible system that enables rapid, precise, and accurate guidance for multiple probes. This thesis presents the design, demonstration, and evaluation of such a system. The device is designed primarily for cryoablation where multiple probes are required, but it can also be used for other image-guided percutaneous instrument insertions.

### 1.4 Thesis Organization

Having provided some background for the thesis, the remaining chapters focus on the design, manufacturing, and evaluation of the simple MRI compatible probe guidance mechanism. Chapter 2 defines the functional requirements of the device and compares various concepts developed during early stage of design. Chapter 3 details the design and bench level evaluation of each module. Chapter 4 describes the prototyping process, including the setup of electrical components, and defines the kinematics of the device. Chapter 5 reports the preliminary testing results of the mechanism. Chapter 6 provides conclusions and outlines opportunities for future work that builds on the work presented in this thesis.

# Chapter 2

## System Design Process

The challenges in performing MR image guided cryoablation intervention in a closed-bore magnet were identified based on conversation with Dr. Kemal Tuncali from BWH and observations of current methods. Each step of the procedure was analyzed to determine whether robotic assistance could offer significant improvement in placement of the ablation probe. The design approach was to select the minimum number of DOF required to address the probe placement problem. Many tasks were determined to be better performed manually to ensure safety of the patient and retain the work-flow clinicians are comfortable with. In this chapter, the functional requirements of the device are outlined in section 2.1. Early design strategies and concepts are compared in section 2.2.

### 2.1 Robot Functional Requirements

The typical lesion size suitable for treatment with cryoablation ranges from 10 to 50 mm in diameter. In general, vertical insertion is desired to limit the amount of tearing of tissue, but some tilting of the intervention probe is often necessary to avoid major anatomy, minimize incision length, and ablate cancerous tumors of greater size. Two to ten probes may be used during a procedure, but three probes are used on average. To ensure that the entire tumor reaches the minimal required temperature for ablation,  $-40^{\circ}\text{C}$ , it is recommended that the probe tips are embed in the tumor. For three probes, the tips should be placed less than 5 mm away from the edge of the tumor and spaced less than 17 mm from one another.

The robot is designed to work for the most common case, where the lesion is 25-30 mm in diameter. In this case, three 17 gauge probes (1.473 mm in diameter and 17.5 cm long) are placed, sharing the same probe insertion site on the skin, to reach an average depth of 125 mm and maximum tilt of 45 degrees from the normal of skin.

It was determined a total of three DOF (two actuated and one manual) are essential in the placement of multiple intervention probes, thus should be incorporated into the robot: the two actuated DOF for orientating the probe and the manual one for releasing the probe once insertion is completed. For safety of the patient, insertion of the probe is performed manually. As described by Walsh *et al.* [12], the part of the probe remaining outside of the body exhibits oscillatory motion due to respiration and muscle movement. Holding the probe still after insertion would cause undesirable laceration to tissue, therefore the clinician must be able to disengage the probe from the device to prevent such injury. The device should have a small footprint, minimizing the amount of occupied space inside of the imaging bore, and be mounted in such a way to provide a sufficiently stable platform for probe insertion.

Unique to MRI-guided procedures, a flexible MRI coil must be affixed to the patient over the region of interest to produce high quality images (Figure 2-1). Probes should enter the body from areas close to the coil, either through the window in the middle of the coil or immediately outside of it. Having a device that can accommodate the imaging coil not only optimally utilizes the small workspace inside of a closed-bore (maximum 700 mm), but also intuitively instructs the interventionists how the device should work, which is crucial for its clinical acceptance in the future.



Figure 2-1 MR imaging coil must be placed on top of patient prior to scanning in order to produce useful data for diagnosis and interventional procedures [<http://www.siemens.com>].

For MRI compatibility, only non-ferrous metals, including aluminum and beryllium copper, and plastics can be used to construct the device. Thermal and electrical conductance of the non-ferrous metals could induce image distortion and cause local heating; therefore the main structure of the device should be made of plastic and the parts constructed with non-ferrous metals should be small and placed at a reasonable distance away from the imaging bore. Furthermore, the actuators/sensors/electronics used to drive the device need to be operational and safe in a MRI environment.

The end goal of the device is to be able to accurately and precisely place probes. Taking into account needle bending, the maximum error at the tip of the probe should be within  $\pm 5$  mm from the target point. The device should use fiducial based registration in MR imaging software to allow for real time monitoring of its performance. Finally, the device should not cause harm to the patient and can be sterilized to clinical standards.

In summary, the functional requirements of the device are as follows:

1. MRI compatible
2. Position three probes (sharing one insertion site) with two actuated DOF

3. Staple small-footage mount that accommodates patient's movement and MRI imaging coil
4. Manually release probe after insertion
5. Device registration in imaging software
6. Probe tip end position within  $\pm 5$  mm of selected target
7. Safe
8. Sterilizable

## **2.2 Strategy and Concept Selection**

Based on the functional requirements mentioned above, two critical modules need to be designed: the device mounting module and the probe guidance module. The device mounting module is used to stabilize the whole device to the patient and provide registration assistance. The probe guidance module contains the mechanism for orientating multiple probes to the desired angles and the mechanism for releasing the probe when insertion is completed.

### **2.2.1 Device Mounting Module**

The design strategies considered for the mounting module include 1) mount the device to the patient, 2) mount the device to the MRI bed, 3) mount the device to the MRI coil, and 4) mount the device to a structure outside of the imaging bore. When mounting to the patient, the device can be small and potentially cheap in material cost. The device would follow the patient's breathing motion, result in accurate needle positioning and less chance of accidental harm. On the other hand, this strategy has the risk of providing an unstable base platform due to compliance of the body. More rigorous sterilization

procedures would be needed since the device is in direct contact with the patient. Additional consideration needs to go into the placement of the MRI coil.

When the device is mounted to the MRI bed, the base platform would be more stable and rigid compared to mounting to the patient. The geometry of the mounting module, however, would be limited to the type of MRI being used. Furthermore, this strategy cannot accommodate for a patient's breathing or small movements, which may result in extra error at the needle tip.

The device can also be mounted onto the MRI coil. Currently, the coil is strapped to the patient via Velcro and tape. The coil may provide the extra stiffness needed to stabilize the device and would still allow the device to move along with the patient to avoid error or harm. Also, sandwiching the MRI coil in between the patient and the device may help improve the image quality. However, since the device is not mounted directly to the patient, there is a risk of additional motion between the patient and the coil. More tension in the Velcro and tape are required to securely attach both the device and the coil to the patient. The thickness of the MRI coil may further complicate the geometry of the device.

Finally, mounting the device to an outside frame would make it easier to select actuators and materials. This strategy would increase the size, weight, and complexity of the device, and potentially increase the cost of manufacturing.

The mounting module strategies (Figure 2-2) are evaluated with a Pugh chart, as shown in Table 2-1. Mounting to the MRI bed is used as the datum strategy. Evaluation categories such as size, stability, and ability to move with the patient are considered. The Pugh Chart shows that because mounting the device to an external frame is larger in size,



more expensive, and may increase risk to the patient, it is significantly harder to optimize.

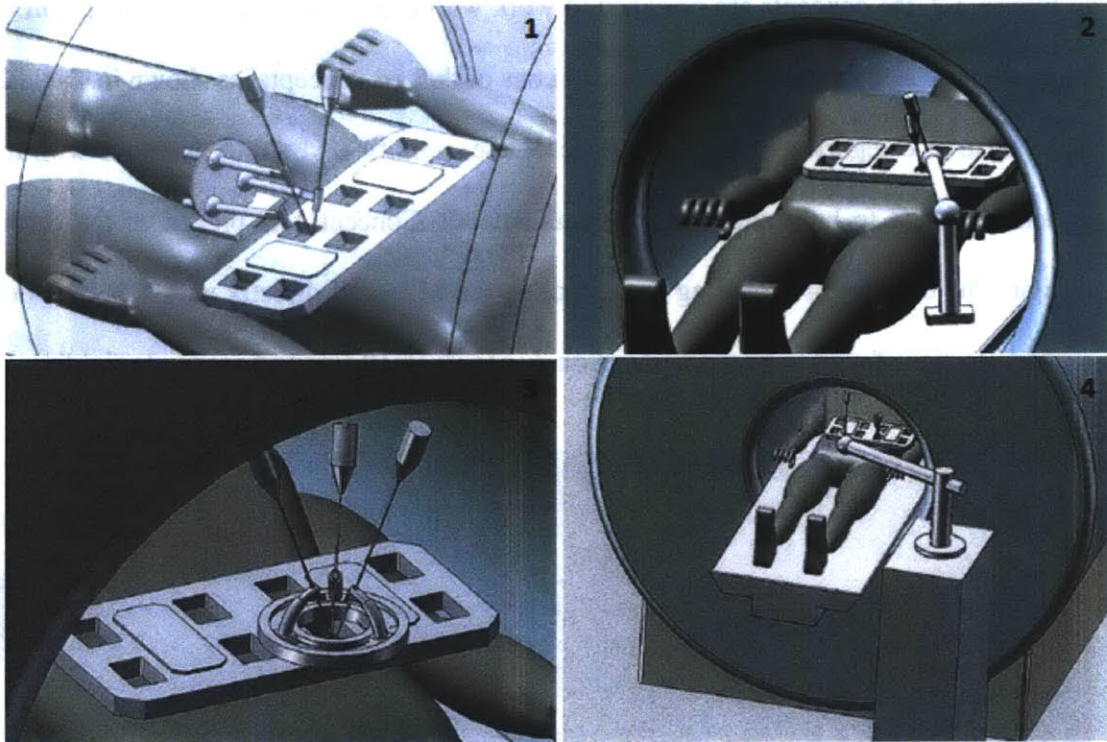


Figure 2-2 Initial strategies of device mounting module. (1) Mounting the device to the patient. (2) Mounting the device to the MRI bed. (3) Mounting the device to a large rectangular MRI imaging coil. (4) Mounting the device to a frame outside of the MRI [16].

Table 2-1 Pugh Chart for device mounting module strategy evaluation

	patient	bed	Image coil	external frame
Size and Weight	+	D	+	-
Stability	-	A	0	0
Move with Patient	+	T	+	0
Work in all MRI	+	U	+	+
Risk of failure	0	M	0	-
Total	2	0	3	-1

More detailed concepts for each of the other three strategies are modeled in SolidWorks 2010 (SolidWorks Corp., Santa Monica, CA) for further evaluation (Figure 2-3). Similar to Figure 2-2, the concepts are designed to work with a large rectangular imaging coil. A Pugh chart is used to compare the pros and cons of these 4 concepts, as shown in Table 2-2. Evaluation categories such as size, ease of use, rigidity, and ability to move with the patient are used to help with the selection process. Concept 1 is picked as the datum design. The concept of mounting the device to the MRI coil directly with a belt of pre-curved plastic is found to be the best option due to its small size and moderate rigidity.

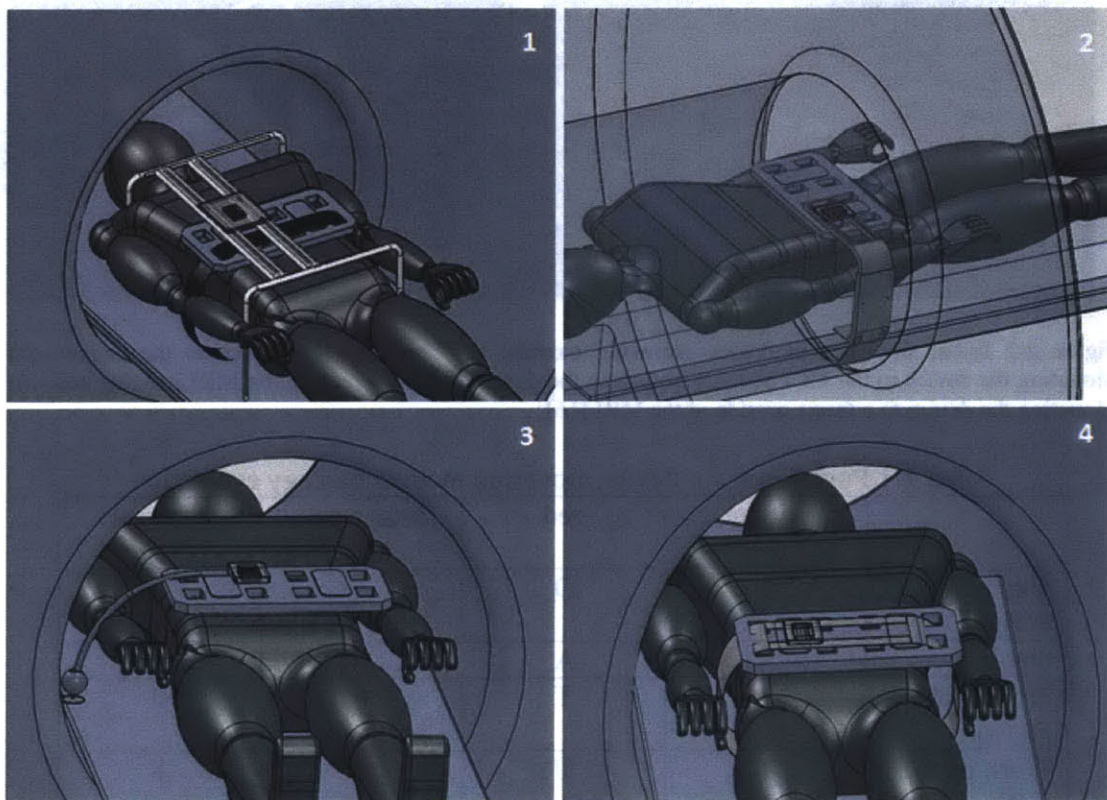


Figure 2-3 Device mounting module concepts. (1) Concept 1 uses a belt to wrap the device on the patient. Telescoping legs resting on the bed would provide extra stability. (2) Concept 2 attaches to the side of MRI bed and can accommodate for patient size/cancer location with a telescoping arm. (3) Concept 3 also connects to MRI bed, with curved telescoping arm to provide reach and structural support. (4) Concept 4 secures the device and imaging coil with a belt or pre-curved plastic.

Table 2-2 Pugh Chart for device mounting module concept evaluation

Concepts	Telescoping Frame	Side Mounted Arm	Curved Arm	Flexible Band
Size	D	+	+	+
Ease of Use	A	0	0	+
Rigidity	T	+	0	0
Move with Patient	U	0	0	+
Risk of failure	M	-	-	0
Total	0	1	0	3

A bench level prototype of the selected concept was made to verify the idea. Shown in Figure 2-4, the prototype is a thin sheet of pre-curved stainless steel band attached to an ABS plastic sheet with bolts. Tape was put on the sharp edge of the band to make it safer to wear. The curved band naturally wraps around the body and resisted loads (i.e. being pushed by hand) with sufficient force to stay in place. This experiment showed that concept 4 could become a physically viable option for mounting the device on a flat and somewhat flexible imaging coil. Further research would be needed to find a plastic with spring properties similar to that of stainless steel. Other attachment options include tying the device down with belt or tape, which is currently used for securing the imaging coil on the patient.



Figure 2-4 Bench level prototype of the device mounting module. Left: The prototype is made of two curved stainless steel bands and a sheet of ABS. Middle: The flexible band naturally wraps around the body and can rigidly support the device (acrylic model). Right: Side view of the prototype.

Discussion with Dr. Tuncali led to the discovery of the 4-channel Flex Loop Interface from Siemens (Munich, Germany), a.k.a. loop coil. This particular imaging coil, illustrated in Figure 2-5, contains a large window for probe insertion and occupies only a small area on the body, making it perfect for interfacing with a probe guidance robot. Procedures conducted by Dr. Tuncali with the loop coil yielded image of similar or better quality compared to the large rectangular coil normally used. This discovery confirms the selection of the image-coil-mounting strategy and calls for a concept that can accommodate a loop coil that has an outer diameter of 136 mm and a height of 19 mm (Figure 2-5, Right). Adhesive or Velcro, which are readily available in the MR imaging room, can be used to secure the device and the coil onto the patient.

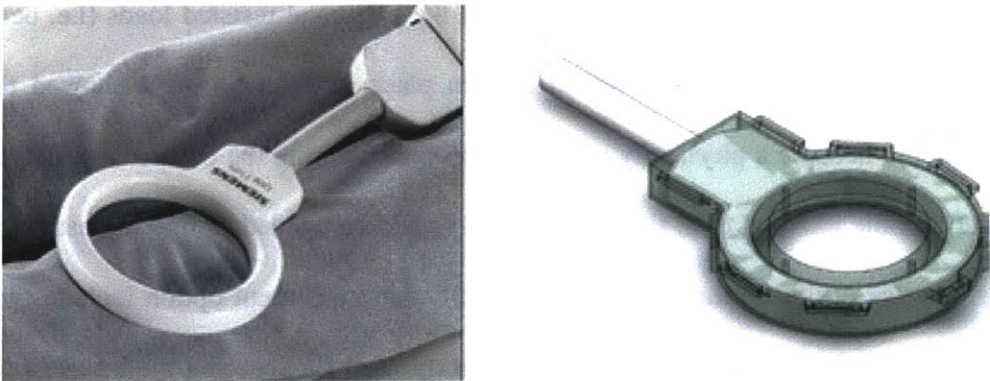


Figure 2-5: Device is designed to accommodate a large 4-channel Flex Loop Interface (loop coil). Left: Loop coil from Siemens is small and contains a large window in the middle [<http://www.siemens.com>]. Right: Example design to allow attachment of the device to the loop coil (device is shown in transparent green).

### 2.2.2 Probe Guidance Module

Two strategies are considered to allow for positioning of multiple probes: 1) multiple moving arms to position three probes at once, and 2) single moving arm to place one probe after another. With multiple arms, it would take less time to place all the probes; however, it would also require three times the number of actuators compared to a single

moving arm. The space for probe insertion may also be reduced with multiple arms in the way. A single moving arm design leaves more open space in the middle of the device for conducting operation after the device as mounted, such as making an incision, injecting local anesthesia, and applying warm saline to the skin close to the probe insertion site to prevent frost bite. On the other hand, placing one probe at a time would require moving the arm with the previously inserted probes in the way of the motion. To avoid the device colliding with already positioned probes, the order of probe insertion must be optimized. Table 2-3 evaluates the pros and cons of the two strategies. Because the single arm strategy is simpler, less expensive, and more flexible, this strategy is selected.

Table 2-3 Pros and cons of probe the positioning strategies

Strategy	Pros	Cons
Multiple Arms	<ul style="list-style-type: none"> <li>• Fast, position all probes at once</li> <li>• No probe collision</li> </ul>	<ul style="list-style-type: none"> <li>• Increased parts, more expensive and harder to manufacture</li> <li>• Limited work space for other operations</li> <li>• May not have full range of motion due to arm size</li> </ul>
Single Arm	<ul style="list-style-type: none"> <li>• Less parts, and smaller package</li> <li>• Cheaper and complicated to make</li> <li>• Large work space for other operations</li> </ul>	<ul style="list-style-type: none"> <li>• More time required for positioning</li> <li>• May experience probe collision (limited range of motion)</li> <li>• Require probe placement optimization</li> </ul>

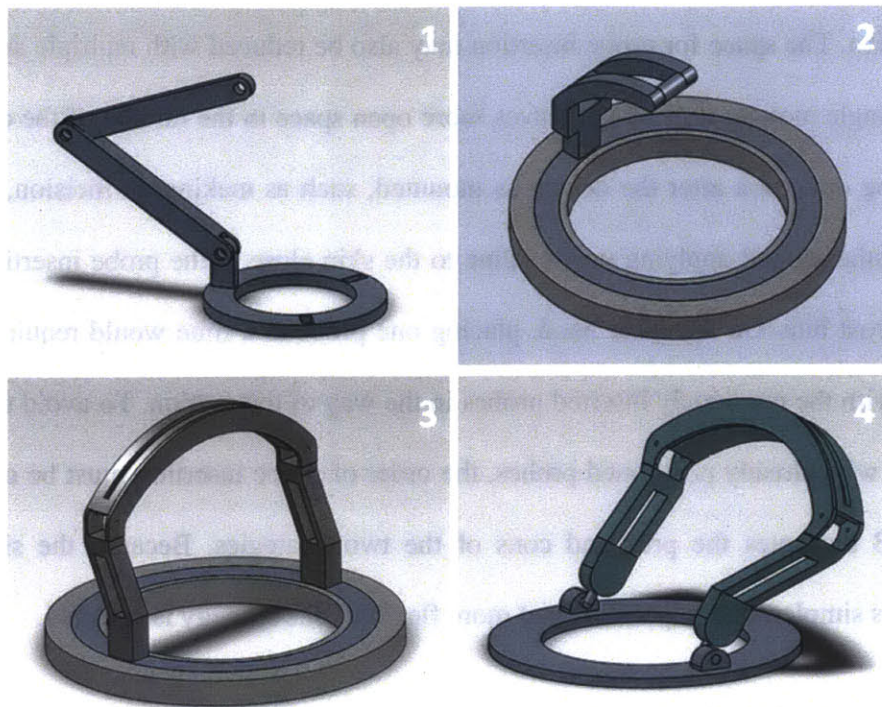


Figure 2-6 Probe guidance module concepts. (1) Concept 1 is the classical 2 bar-3 joint linkages design. An end effector on the tip of the free end of the linkage holds the probe in place (2) Concept 2 has half of a circular arm that spins about the base. The end effector would be clamped on the arm and slide along it, providing the second degree of freedom. (3) Concept 3 is the full circular arm version of concept 2. (4) Concept 4 is a pivoting hoop, also with the end effector sliding on top of the hoop.

A few rough concepts were sketched in Figure 2-6. Table 2-4 evaluates the concepts, with the 2 bar-3 joint design as the datum. Due to its intuitive use and simplicity, the concept with a pivoting hoop is found to be the best option to develop further into detailed design.

Table 2-4 Pugh Chart for probe guidance module concept evaluation

Concept	Linkage	Half Arm	Full Arm	Pivoting Arc
Size	D	0	-	-
Ease of use	A	0	0	+
Rigidity	T	0	+	+
Reach	U	+	+	+
Space for other operations	M	+	+	+
Moving Actuators	D	0	0	+
Total	0	2	2	4

Figure 2-7 is a rough sketch of what the whole device may look like. The hoop would rotate about a remote center of motion and a carriage, carrying the probes, would travel on top of the hoop. The base conforms to the shape and size of a loop coil. The strap anchors on the side of the base facilitate a secure belt attachment between the device, loop coil, and the patient. The base and motors can be covered with a plastic sheet, separating them from sterile hands or the incision. Fiducial markers may be embedded in the base and the hoop for registration purposes.

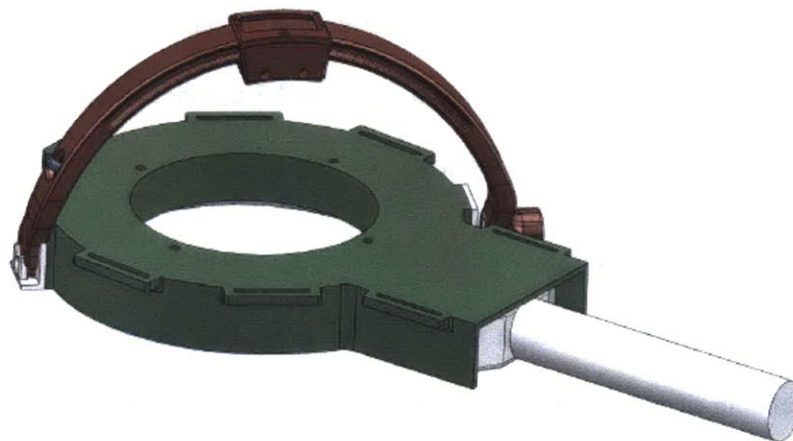


Figure 2-7 A 3D model of the device incorporating both design modules. The base (green) would cover the loop coil and contain registration markers. The pivoting hoop and carriage would provide the 2 DOF motion needed to orient ablation probes.

# Chapter 3

## Detailed Design

Given that the device contains two actuated DOF, mounts to an imaging coil, and must be constructed out of MRI compatible material, a cable driven system was designed. This chapter details the design of each component. Section 3.1 discusses the analysis and bench level evaluation of a custom designed low friction bearing. Section 3.2 models and examines the cable drive. Section 3.3 provides an overview of existing MRI compatible actuators. Section 3.4 illustrates the overall structure of the device, including fiducial marker placements and loop coil attachment. Section 3.5 outlines the design of the needle holder and the associated release mechanism.

### 3.1 Low Friction Bearing

The design concept of a carriage traveling on a rotating hoop was selected for its simplicity, freedom of movement, and multiple needle guidance capabilities. The motion of the carriage should be constrained to only allow 1 DOF (i.e. along the hoop), and the movement along the hoop should be smooth, requiring a low force input.

The functional requirements of the bearing based on reasonable estimates include:

1. Low friction- force required from the motor to move the carriage is less than 3 N.
2. Stiffness- with less than 10 N of load, the displacement of bearing in constrained directions is less than 0.1 mm (100,000 N/m).
3. Smooth motion- high frequency frictional noise fluctuation is within  $\pm 0.02$  N.
4. Speed and acceleration- limited to slow movement of about 1 cm/s and 1 cm/s<sup>2</sup>.



5. Compact size and light weight- bearing is smaller than 40 mm in each direction and weighs less than 300 g.
6. Manufacturability- easy to make, assemble, and adjust.
7. Material compatibility- bearing is made of plastic and other non-ferromagnetic materials.

Different types of bearing designs were explored, including sliding plane contact bearing, sliding point contact bearing, non-recirculating ball bearing, and roller bearing. The selected bearing was modeled, analyzed, and tested in a bench level experiment to confirm its functionality.

### 3.1.1 Bearing Design Selection

Many types of bearings were explored and experimented with (Appendix A). Due to the limitations of 3D printed parts, sliding bearings and non-recirculating ball bearings exhibited large friction or stiction. A roller bearing was selected in the end because the line contact would be less affected by the surface finish of a 3D printed hoop. It would also eliminate the need of using large number of rolling elements, as the case with recirculating ball bearing, and improve the stiffness of the bearing overall.

By first order analysis, the friction experienced by the roller bearing can be calculated with

$$F_{roll} = C_{rr}N = \sqrt{\frac{z}{d}} m_{bearing} g \cos \theta \quad (3.1)$$

where  $z$  is the amount of deformation on the surface of the hoop caused by the ball,  $d$  is diameter of the roller, and  $\theta$  is the angle between the carriage and the hoop (as defined in

Figure 3-1). With a 10 mm roller and a  $z$  on the order of  $1 \mu\text{m}$  (rubber tire rolling on concrete road [17]), the resulting rolling friction is about 0.03 N.

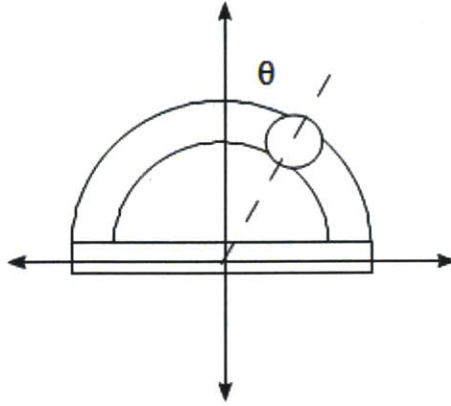


Figure 3-1 Simple device model which defines the angle between the centerline of the carriage and the hoop as  $\theta$ .

A few design concepts that kinematically constrain the carriage to the hoop are shown below. In the case of Vee groove rollers (Figure 3-2), four rollers are needed to constrain the carriage, with the single roller on the top right side being a floating roller to avoid jamming.



Figure 3-2 Vee groove roller bearing design. Four rollers are required to kinematically constrain the bearing.

Another idea is to use roller coaster type bearing, which is first designed by John Miller in 1919 (Figure 3-3). Here, six to eight rollers are needed to fully constrain the 5 DOF of

the carriage. This design is quite flexible: the roller can have a grooved shape to ride on a rail like hoop, such as the case with actual roller coasters; the rollers can also be flat when the cross section of the hoop is in the shape of a stop sign [18].

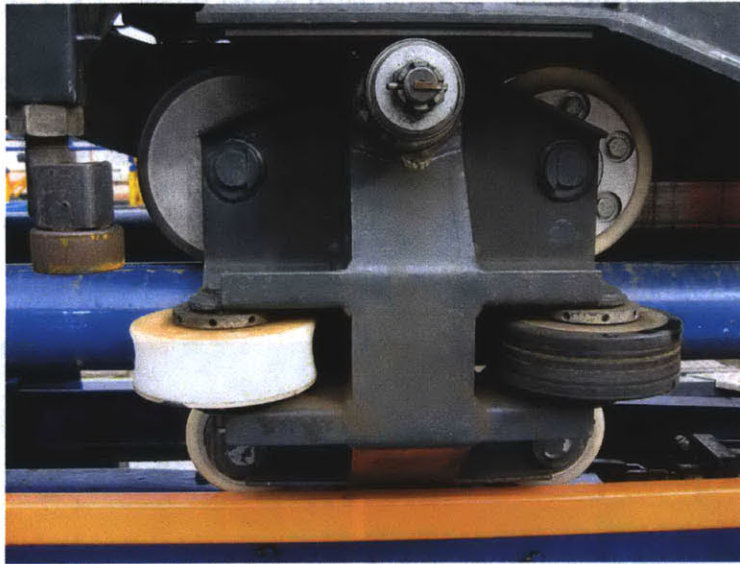


Figure 3-3 Roller coaster type bearing design would require 6 to 8 rollers to constrain bearing motion properly [<http://en.wikipedia.org>].

A third idea, as shown on Figure 3-4, would require a minimum of three rollers to kinematically constrain the bearing on a triangular prism. Here, flat rollers are used and no especial features are needed for the hoop. This means the bearing can be properly constrained with less precise placements of the rollers.

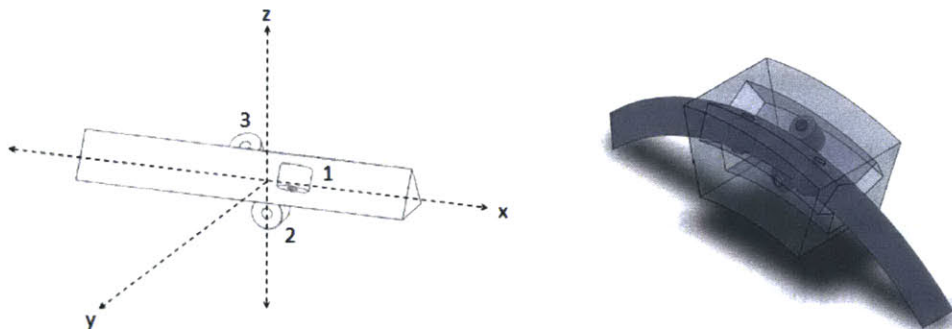


Figure 3-4 Bearing riding on a triangular prism would require a minimum of 3 rollers.

The triangular prism idea is easy to implement and test. The simple geometry also makes the imprecision often seen in 3D printed parts less influential to the overall performance of the bearing. Furthermore, the potential of using fewer rollers is an advantage in terms of device cost. A bench level model (Figure 3-5, Left), with straight triangular prism in place of the hoop, was constructed to validate this design. Due to limitations of 3D printing, when the rollers are put in the bearing, they are about 0.6 mm off from the surface of the prism in each direction. Teflon shim was taped to the triangular prism to compensate for the offset.

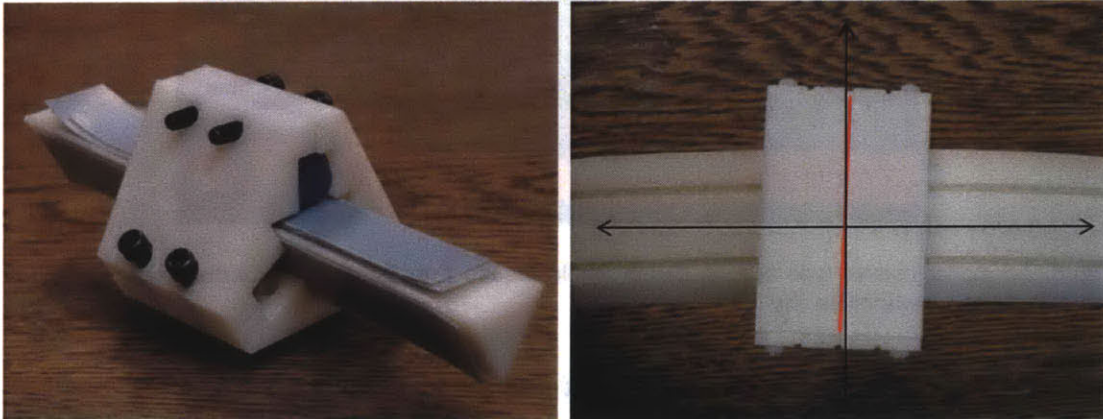


Figure 3-5 Bench level prototype of roller bearing riding on triangular prism. Left: A model of the three-roller bearing design was made, with a straight triangular prism substituting for the hoop. Right: A model of the bearing was made to fit on a curved triangular prism. Even though the bearing is kinematically constrained, the bearing tends to pivot to the side.

The prototype bearing moved easily when manipulated by hand, and it is observed that all three rollers were able to roll on the sides of the prism smoothly. Although the three-roller design kinematically constrains the motion of the bearing, it does not center the bearing on triangular prism, but tends to turn the bearing towards the side with no supporting rollers (Figure 3-5, Right). Modifying this design to accommodate 5 rollers would center the bearing on the prism, with 4 rollers on top and 1 roller on the bottom. The new bearing is able to maintain the stiffness and rolling motion seen in the 3 roller

prototype. Even though this final design is over constrained, the forces on the bearing are evenly distributed among the rollers, and the motion is felt to be smooth with low friction.

Based on the preliminary design and evaluations, the 5-roller design seems to be a viable option for a bearing that is MRI compatible and can travel on a curved 3D printed surface. In the next section, specifics of the bearing/carriage design are explored in detail.

### 3.1.2 Detailed Bearing Design

The bearing contains two side walls and a top wall (Figure 3-6). The side walls are designed to be identical for simplicity and intuitive assembly. The driving dimensions of the bearing are the distances between the surface of the hoop and the walls, as well as the thinnest part in the walls. For structural integrity, the thinnest part of a 3D printed material should be no smaller than 2 mm. Based on previous printing experience, 1.5 mm clearance between the hoop and the carriage wall is sufficient to avoid the two parts sliding on each other.

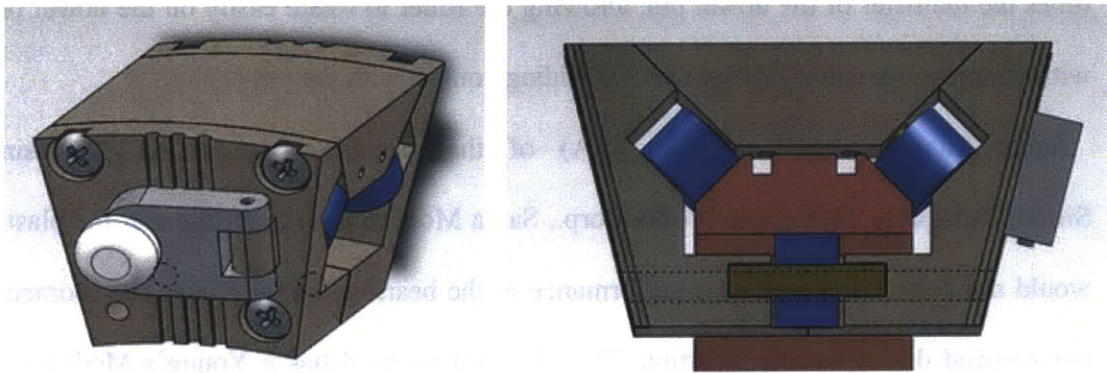


Figure 3-6 Roller bearing design incorporated into the carriage. Left: CAD of the completed carriage. Right: cross section view of the carriage riding on the hoop that contains a triangular profile (red).

The hoop profile is triangular, with the tips of the triangle flattened to decrease the amount of material used. To further minimize the size of the carriage and still keep a

stable contact without jamming, the horizontal distance ( $W$ ) between the two sets of rollers on top are 1.6 times the vertical distance ( $L$ ), as shown in Figure 3-7. The soft rollers can be preloaded to the hoop, improving the bearing stiffness and correcting for unevenness of the hoop surface.

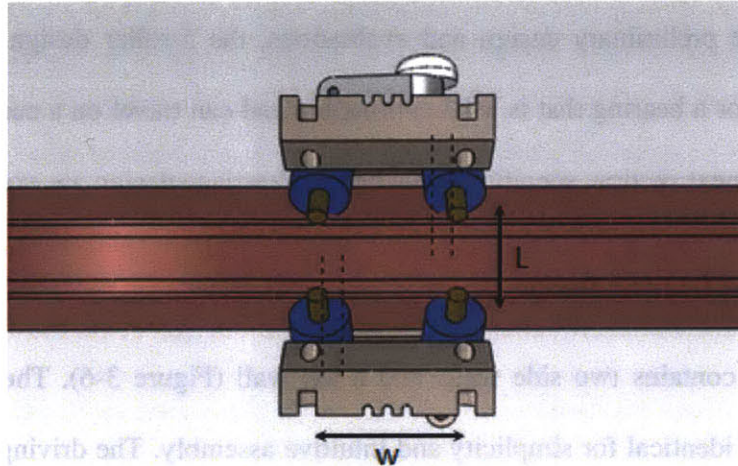


Figure 3-7 Top view of the carriage riding on the hoop. The rollers are positioned to evenly distribute force, constrain the motion of the bearing, and avoid jamming.

The smallest off the shelf Precision Urethane Idler Rollers available (McMaster Carr, USA), with 3/8" diameter, 1/4" width, and 1/8" ID bore, were installed in the bearing. The rollers ride on 1/8" diameter, 5/8" long brass dowel pins. The OD of the roller is three times the diameter of the dowel pin, allowing the roller to rotate easily on the dowel pin without losing too much energy from its sliding contact with the pin [19].

Static finite element analysis (FEA) of the carriage was carried out using SimulationXpress 2010 (SolidWorks Corp., Santa Monica, CA) to ensure that the plastic would not deflect and affect the performance of the bearing due the forces and moments experienced during needle insertion. The 3D printing resin has a Young's Modulus of 2.46 GPa and an Ultimate Tensile Strength of 45.7 MPa, which are similar to those of ABS and Nylon. Assuming worst case scenario, the carriage is held fixed to the hoop and all the forces from needle insertion, which is 10 N according to [12], is translated to the

holes holding the rollers. Figure 3-8 shows the result of the analysis. The maximum stress in the carriage is 128 KPa and the deformation in the holes is about 0.58  $\mu\text{m}$ , which are well within the limits of the 3D printed material.

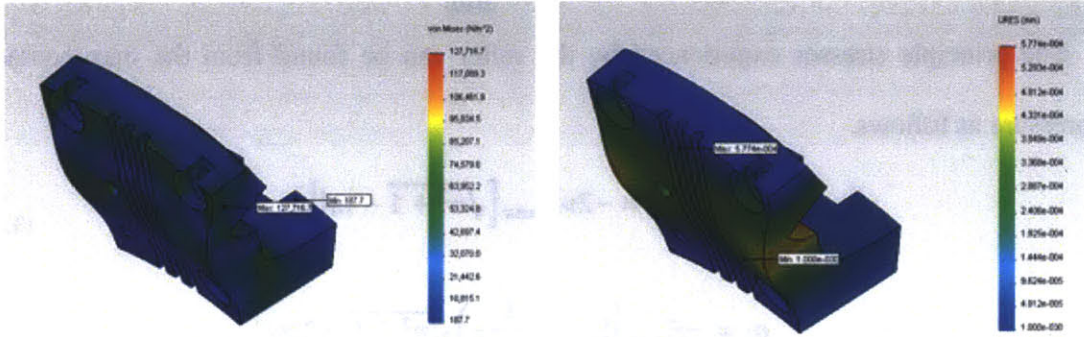


Figure 3-8 FEA result of the carriage. The maximum stress in the carriage is 128 KPa and the deformation in the holes is about 0.58  $\mu\text{m}$ .

First order analysis is used to approximate Hertz Contact Stress between the roller and the surface of the hoop. Knowing the material properties of the Urethane roller and the 3D printing resin, the equivalent modulus of elasticity can be calculated with

$$\frac{1}{E_{eq}} = \frac{1 - \nu_1^2}{E_1} + \frac{1 - \nu_2^2}{E_2} \quad (3.2)$$

At the contact point, the hoop is essential flat ( $R_2 = \infty$ ). Hence the equivalent radius is

$$\frac{1}{R_{eq}} = \frac{1}{R_1} + \frac{1}{R_2} = \frac{1}{R_1} \quad (3.3)$$

The contact area between the roller and the hoop is rectangular, and half of the rectangle width can be calculated from

$$b = \sqrt{\frac{4FE_{eq}}{\pi LR_{eq}}} \quad (3.4)$$

where  $b$  is the half width,  $F$  is the force applied to the roller, and  $L$  is the length of the roller. The maximum contact pressure is inversely proportional to the half width, and, with the equation below, is calculated to be 0.15 MPa.

$$P_{max} = \frac{2F}{\pi bL} \quad (3.5)$$

The principle stresses experienced by the roller can be found from the max contact pressure as follows.

$$\sigma_1 = -2vP_{max} \left[ \sqrt{n^2 + 1} - |n| \right] \quad (3.6)$$

$$\sigma_2 = -P_{max} \left[ \left( 2 - \frac{1}{n^2 + 1} \right) \sqrt{n^2 + 1} - 2|n| \right] \quad (3.7)$$

$$\sigma_3 = -\frac{P_{max}}{\sqrt{n^2 + 1}} \quad (3.8)$$

where  $n$  is the ratio between the half width,  $b$ , and the depth in the vertical direction below the contact rectangle,  $z$ .

$$n = \frac{z}{b} \quad (3.9)$$

Finally, Von Mises stress is calculated from the principle stresses.

$$\sigma_v = \sqrt{\frac{1}{2}[(\sigma_1 - \sigma_2)^2 + (\sigma_1 - \sigma_3)^2 + (\sigma_2 - \sigma_3)^2]} \quad (3.10)$$

Figure 3-9 shows the Von Mises stress as a function of  $n$ . The maximum stress in the contact area is about 0.08 MPa. This stress is small compared to the yield stress of the material, hence no significant pitting or fatigue will happen between the bearing and the hoop surface.



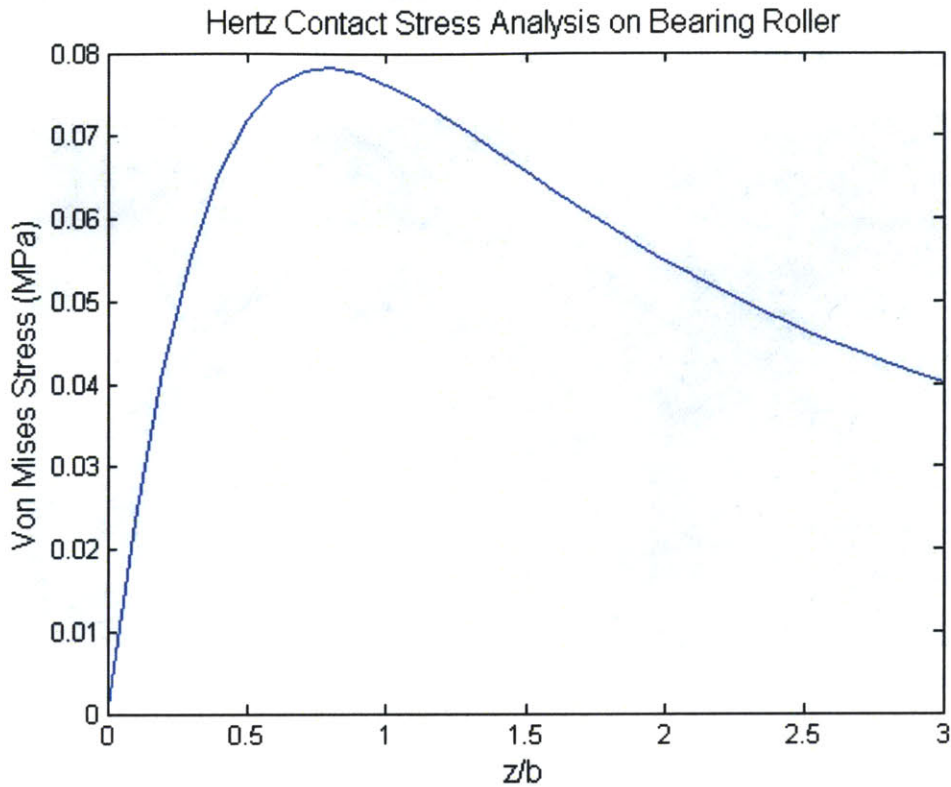


Figure 3-9 Hertz Contact Stress plotted as a function of  $n$ , where  $n$  is the ratio between the depth below contact area and the half width of the contact area.

### 3.1.3 Force and Movement Bench Level Evaluation

To test the movement of the final bearing design, a 2x scale prototype was made. The bearing required moderate force when moved by hand. Twisting the bearing when it is properly mounted on the hoop is quite difficult, proved that sufficient bearing stiffness was obtained. A bench level force test was conducted with a Logger Pro force sensor (Vernier Software and Technology, Beaverton, OR), as shown in Figure 3-10. Figure 3-11 is an example plot obtained from one of the tests. The maximum force measured over all three trials is 2.71 N, which is below maximum force specified in the functional requirements. The force plot exhibited very few force oscillations, with a standard deviation for the force measurement of 0.011 N and a range of 0.5 N. Hence, the motion

of the bearing is proved to be sufficiently smooth and it required low enough force to be actuated with small MRI compatible motors.



Figure 3-10 Bench level test of the roller bearing with Logger Pro force sensor.

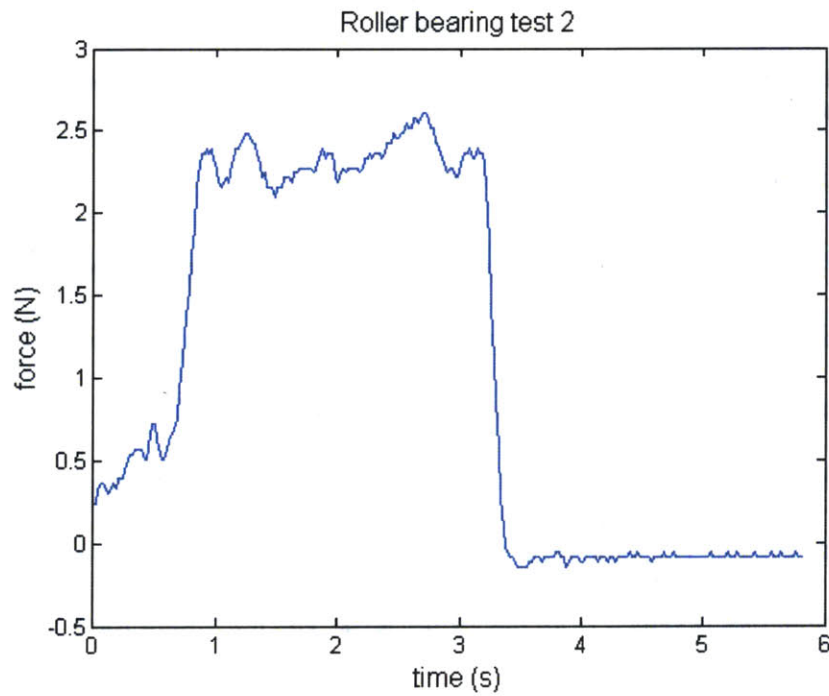


Figure 3-11 Example plot of the bench level test for the bearing prototype. A maximum force of 2.71 N was measured, with a standard deviation of 0.011 N.

## **3.2 Cable Driven Actuation**

For those actuators that cannot be cleaned with a conventional sterilization process, a sterile sheet or bag could be draped over them to ensure that they do not come into contact with sterile hands or instruments. The motors are placed on the side of the robot base, away from the moving probe, so that they could be designed into reusable modules that snap into the device in the future. A cable system is thus required to remotely transmit motion from the motor to the carriage. Section 3.2.1 describes the cable selection process. Section 3.2.2 shows the cable attachment and tensioning methods. Section 3.2.3 is on detailed hoop design which accommodates the cable drive. Section 3.2.4 models and analyzes the system. Finally, section 3.2.5 exhibits bench level experiment of the bearing moving on the hoop, actuated by the cable drive.

### **3.2.1 Cable Testing and Selection**

Plastic cables, such as Kevlar and Dyneema, should be used for MRI-compatibility. Compared to steel cables of same size, Kevlar, an aramid textile material, has higher tensile strength, longer life time, lower weight, better flexibility, and more importantly lower stretch to maintain position accuracy [20]. Dyneema, a gel span ultra-high-molecular-weight polyethylene, also has high strength, low stretch, and low weight. It can achieve yield strength comparable to high strength steel with 15 times less the mass. Its strength to weight ratio is even 40% higher than aramid and has an unnaturally high lubricity for plastic cables [21].

Figure 3-12 plots the strength of Kevlar, Dyneema, and Nylon. The sample cables are 1 ft long each and were held in an Advanced Mechanical Testing System (Instron, Norwood, MA) with pressure (70 Psi) clamps. Both Dyneema and Kevlar exhibited lower

stretch compared to Nylon and could withstand higher force. Nylon broke at about 150 N and Kevlar broke at about 250 N. The yielding point of the Dyneema was never reached. Due to its low coefficient of friction, the Dyneema cable started to slip in the clamp after over 230 N. Although the cable drive of the system does not require such high yield strength, the low creep, low stretch and especially low friction properties of the Dyneema makes it an ideal cable for this system.

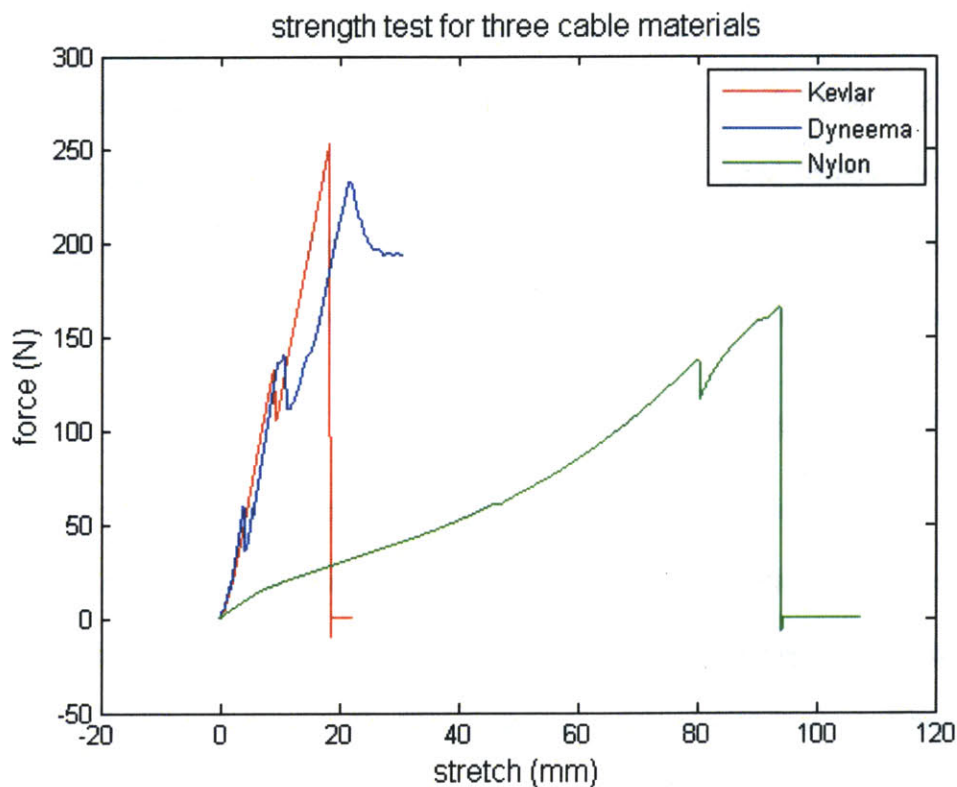


Figure 3-12 Kevlar, Dyneema, and Nylon cables are stretched in the Instron Advanced Mechanical Testing System. Dyneema exhibited high yielding strength and low stretch, ideal for the MRI compatible cable driven system.

A bench level creep test was performed to further test the stretch capabilities of the Dyneema cable. As shown in Figure 3-13, one end of the cable was tied to an aluminum block secured in a vice. The other end drops to the side of the table, weighted down with a 500 g mass. The test is conducted over the course of three days. Measurements of the

cable length are recorded at random times, reported in Table 3-1. The cable stretched about 4.5% over time, which may have been caused by slow tightening of the knots. Nonetheless, the stretch in Dyneema is much lower than that of steel cables, further verifying its usability in a cable drive.



Figure 3-13 Bench level creep test was conducted on Dyneema cable over the course of three days.

Table 3-1 Dyneema cable Creep test result

Time (hr:min)	Length (cm)	% Stretch
0	17.6	0
1:07	18.3	3.97
1:32	18.4	4.54
2:06	18.4	4.54
2:46	18.4	4.54

5:04	18.4	4.54
6:05	18.4	4.54
26:27	18.4	4.54
27:03	18.4	4.54

To find the coefficient of friction between this cable and a 3D printed plastic part, a bench level experiment was conducted where one end of the cable was tensioned with a hanging 500 g mass and the other end was tied to a force sensor (Figure 3-14). Using Logger Pro, a force vs. time plot was generated (Figure 3-15) and the average force required to drag the Dyneema cable was measured to be about 12 N when traveling around a 90 degree hoop. Based on Capstan Principle, this corresponds to a coefficient of friction of 0.57.

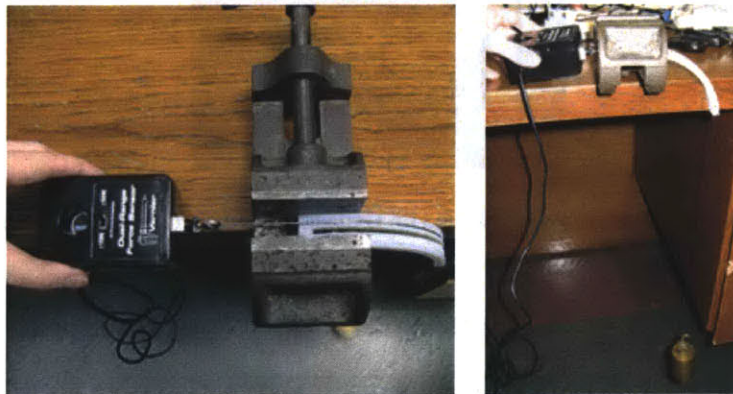


Figure 3-14 Bench level experiment was conducted to measure the coefficient of friction between the Dyneema cable and a 3D printed part.

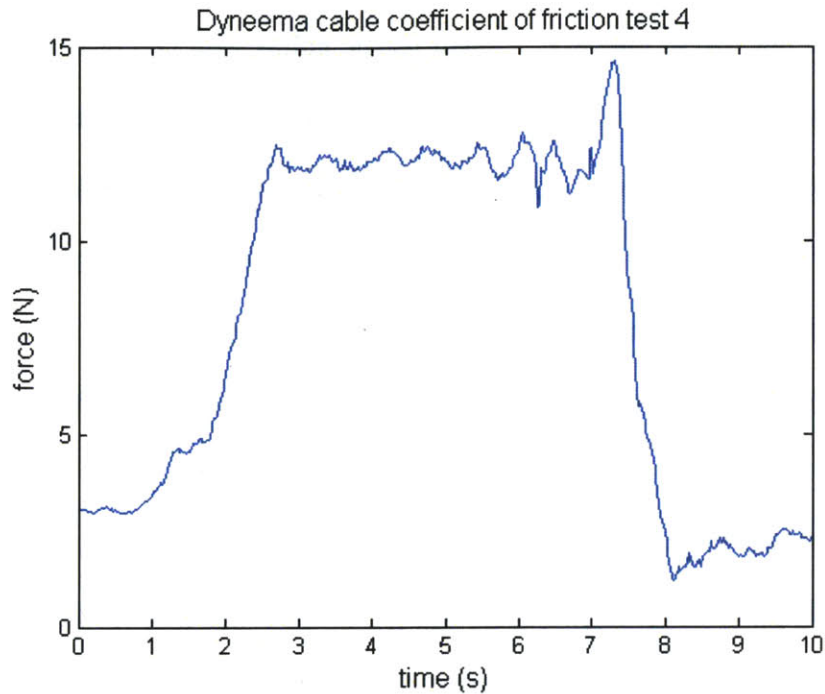


Figure 3-15 Force measured with Logger Pro to calculate the coefficient of friction between a Dyneema cable and a 3D printed part. With an average of 12 N, the coefficient is calculated to be about 0.57.

### 3.2.2 Cable Attachment and Tensioning

The schematics of the cable drive are illustrated in Figure 3-16. The cable is separated into two sections. The first section (red) comes out of the driving pulley, wrapping around the curve of the hoop, and ends on one side of the carriage. The second section of the cable (green) starts from the other side of the carriage, going around the tensioning pulley, then winds around the whole length of the hoop, and comes back to the driving pulley.

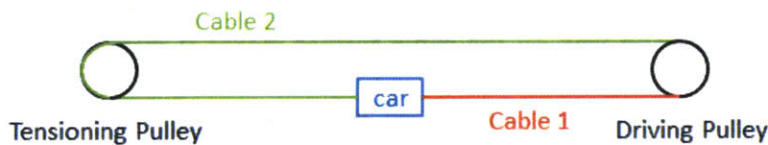


Figure 3-16 Schematics of the cable drive system.

To minimize the size of the hoop, a small plastic pulley with OD of 0.3735 in, ID of 0.32 in, and thickness 0.096 in is selected as the tensioning pulley. For the driving pulley, the thickness of the pulley, groove depth, and its ID are proportional to the length of the cable in each section. The smaller the driving pulley gets, the more rotation from the motor is required for the carriage to travel the whole span of the hoop. As a result, the more space on the driving pulley is needed to wrap the cables. A spreadsheet was used to optimize the size of the driving pulley. As shown in Figure 3-17, the pulley was eventually designed to have an OD of 0.623 in and ID of 0.538 in. The two notches on the driving pulley are 0.107 in apart, allowing the two sections of the cable to be wound up separately, decreasing rubbing friction between the cables.

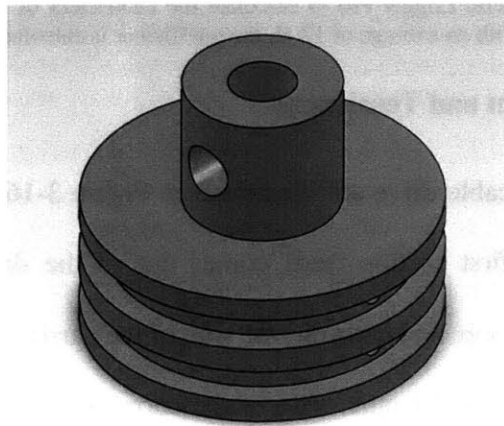


Figure 3-17 Driving pulley contains two layers, separating the outgoing and incoming cables to decrease friction.

As observed during the cable tensioning test, the Dyneema cable is very slippery when sliding against metal. The wax on the cable further makes it difficult to glue the cable securely. Since the cable was originally used as a bow string, a knot-in-hole attachment was devised to attach the cable to the driving pulley and the carriage. As shown in Figure



3-18, a knotted cable is threaded through a 90 degree hole in the part. The hole is made so the bottom end is smaller than the top end. When the knot is pulled through the hole, the knot gets stuck in the bent between the large hole and the small hole, securing the cable in place.

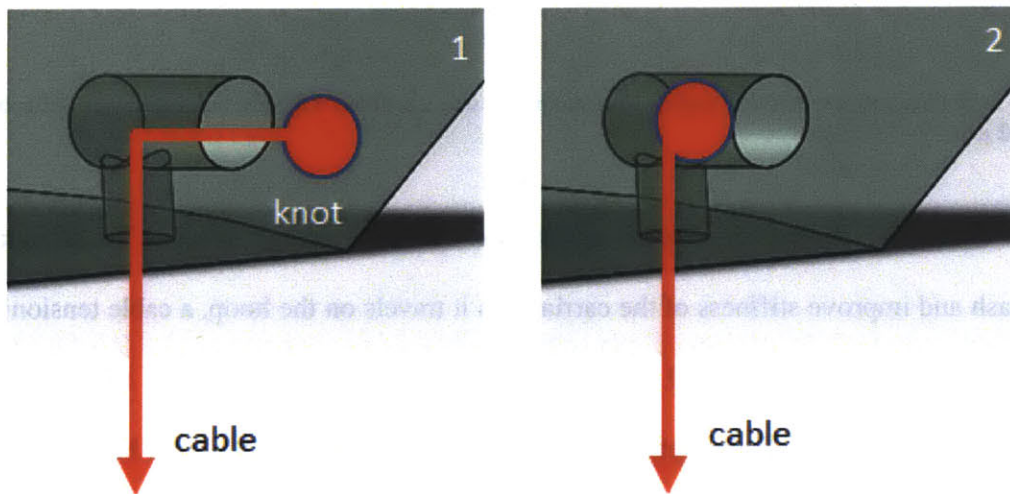


Figure 3-18 A knot-in-hole design allows for the slippery Dyneema cable to be attached to the carriage and the driving pulley.

FEA was performed on the driving pulley, assuming worst case scenario that all the forces from the cables are concentrated at the holes where the cables are attached to. The pulley is assumed to be fixed rigidly on the motor shaft. Figure 3-19 shows the result of the analysis graphically. The maximum stress in the aluminum driving pulley is about 4.8 MPa, with a maximum deflection of 0.002  $\mu\text{m}$ .

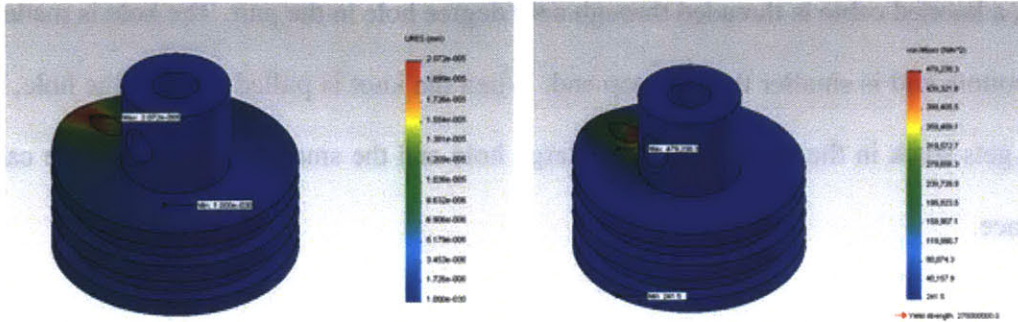


Figure 3-19 FEA result of driving pulley. The maximum stress is about 4.8 MPa and maximum deflection is 0.002  $\mu\text{m}$ .

The tension in the cable directly affects the operation of the device. To eliminate backlash and improve stiffness of the carriage as it travels on the hoop, a cable tensioning mechanism is needed. Several designs were considered, such as a rubber band constrained pulley or a turning tensioner often seen in belt drives. A plastic bolt driven u-shaped tensioning mechanism was design in the end for flexible tensioning capabilities and simplicity (Figure 3-20).

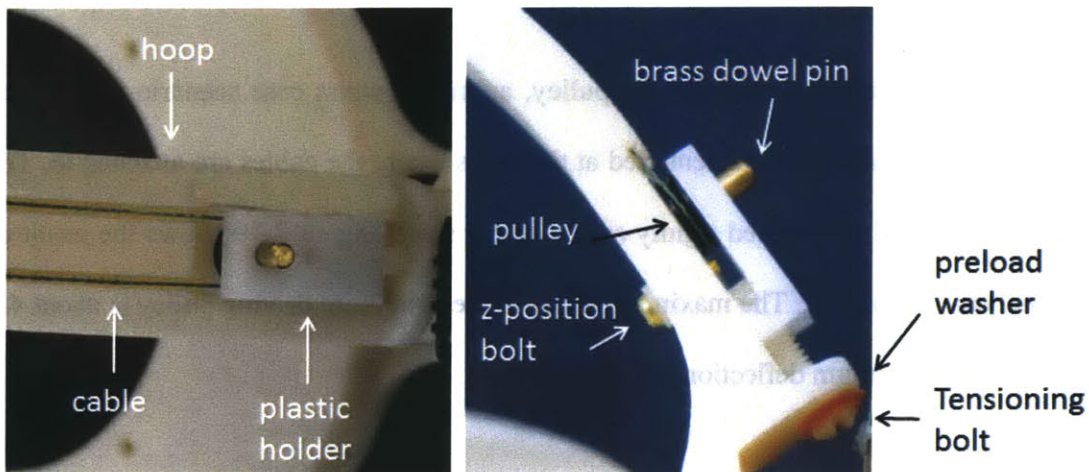


Figure 3-20 The cable tensioning mechanism uses a bolt to finely control movement of the tensioning pulley, which is held in a plastic holder with a dowel pin. Left: Top view of the mechanism. Right: Side view of the mechanism.

The u-shaped plastic holder is machined from Delrin, containing a hole to press fit a 1/8" diameter brass dowel pin. The 5/16" inner diameter tensioning pulley can be put in the holder and rotate freely about the dowel pin. The holder sits in a rectangular pocket on the hoop, constraining the movement of the plastic holder and allowing tensioning movement only along the hoop. A plastic 6-32 bolt goes through a clearance hole in the extrusion above the pocket and threads into the end of the holder. Since the bolt is kept in place with the cable and the extruded wall, rotating the bolt would cause the plastic holder to move forward or backward. A 0.07" thick Polyurethane washer is put in between the head of the bolt and the extruded wall to provide some preload, compensating for small amount of slack in the cable caused by creep. On the bottom of the plastic holder, there is a tapped hole for a M2 bolt. The slot on the bottom of the pocket allows the M2 bolt to travel with the holder. Tightening the M2 bolt would ground the holder in the pocket and reduce stress in the thread of the 6-32 bolt caused by tension in the cable.

The dowel pin in the tensioning mechanism experiences 3 point bending. First order analysis with the equation below shows a flexural stress of about 2.77 MPa, which is well within the capabilities of the brass pin (Yielding Strength 200 MPa).

$$\sigma = \frac{PL}{\pi r_{pin}^2} \quad (3.11)$$

### 3.2.3 Hoop Detailed Design

As mentioned in section 2.2, the device is designed to be mounted on a loop imaging coil. Being constrained by the size of the loop and the wall thickness of the base, the minimum distance between the two legs of the hoop is 142 mm. Adding 1 mm on each

side to provide enough clearance for the hoop to rotate without rubbing against the base, the legs must be at least 144 mm apart. The hoop should also enable the carriage to be clear of the edge of the base when it moves to the extreme angle (45 degree). After several design iterations, a hoop with a radius of 80 mm and a thickness of 8 mm is found to be the best compromise between probe reach, hoop clearance, and aesthetics (Figure 3-21).

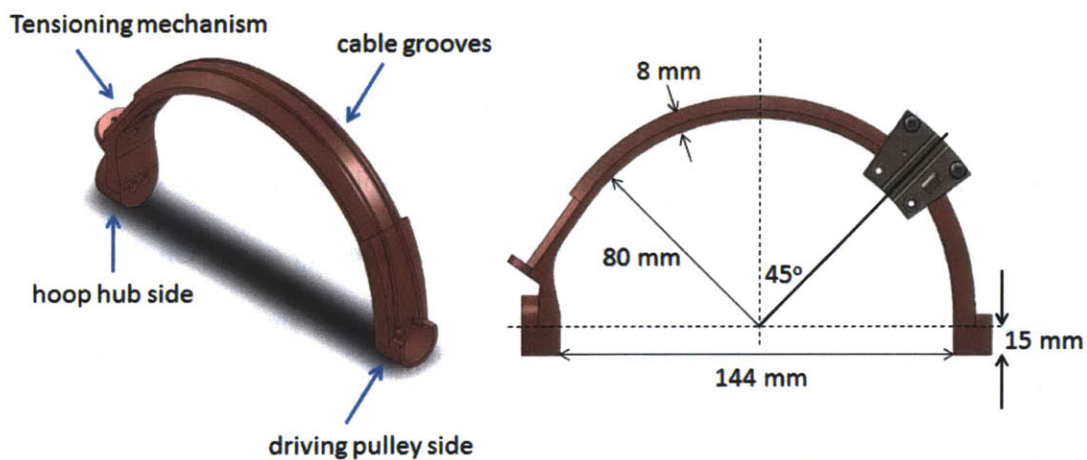


Figure 3-21 Hoop Design. Left: The hoop has a pocket for attaching the driving pulley on the right leg, a pocket to attach the hoop hub on the left leg, and a pocket for the cable tensioning mechanism. Right: Hoop dimensions.

The cross section of the hoop is shown in Fig 3-22. Simulating the triangular prism shown in previous section, the two slanted sides, 45 degree from horizontal, and the flat bottom side allow the rollers to constrain the motion of the carriage. The two grooves in the middle, squares with 2 mm long edges are for the cables to ride in. The grooves are parallel along the hoop, spaced 0.165 in apart to accommodate the size of the tensioning pulley. An aluminum hub interfaces with the round hole on the bottom of the left leg, attached to the hoop with two M2 bolts. The hub allows for more secure connection to the motor and helps distribute load. The round extrusion around the hub pocket would rest on corresponding features on the base for additional support and rotation alignment.

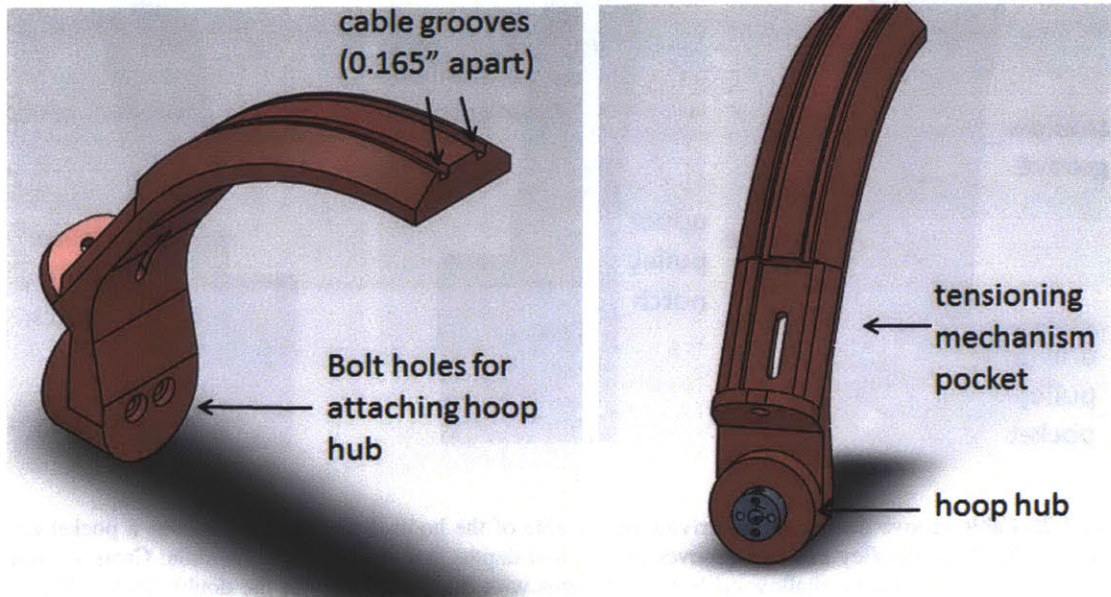


Figure 3-22 Hub side of the hoop. Left: The hoop has a triangular cross section, with the tips flattened to minimize material usage. Right: The hoop contains a rectangular pocket to hold the tensioning mechanism. An aluminum hub is designed to interface with the hoop for better alignment and support.

Illustrated in Figure 3-23, the cable grooves span outward on the right leg of the hoop to allow for smooth transition to the driving pulley. The grooves in the leg are cut to different depths, so the cable can wrap easily into different notches on the pulley. The circular pocket is deep enough to hold the double pulley within the hoop. Again, the outer wall around the pocket allows the hoop to rest on corresponding part in the base, providing extra structural support in the z direction. The knob inside the pocket helps to align the double pulley in the hoop and is not intended to take any load.

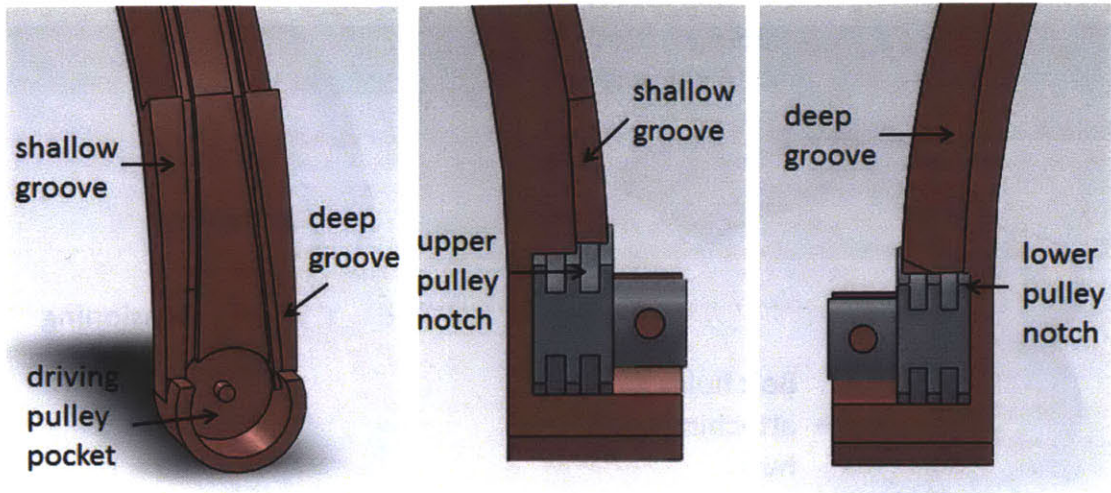


Fig 3-23 Cable groove design on the driving pulley side of the hoop. Left: The leg contains a pocket for positioning the driving pulley and two grooves of different depths that span outward. Middle: Cross section view of the leg, where the shallow cable groove aligns with the upper notch in the double pulley. Right: Cross section view of the leg, where the deeper cable groove aligns with the lower notch in the double pulley.

In modeling the loading condition of the hoop, a worst case scenario of 10 N insertion force solely applied to the middle of hoop was assumed. Figure 3-24 shows the FEA results. The max stress calculated is 1.86 MPa, and the max deflection is 0.054 mm. These values are within the capabilities of 3D printed parts.

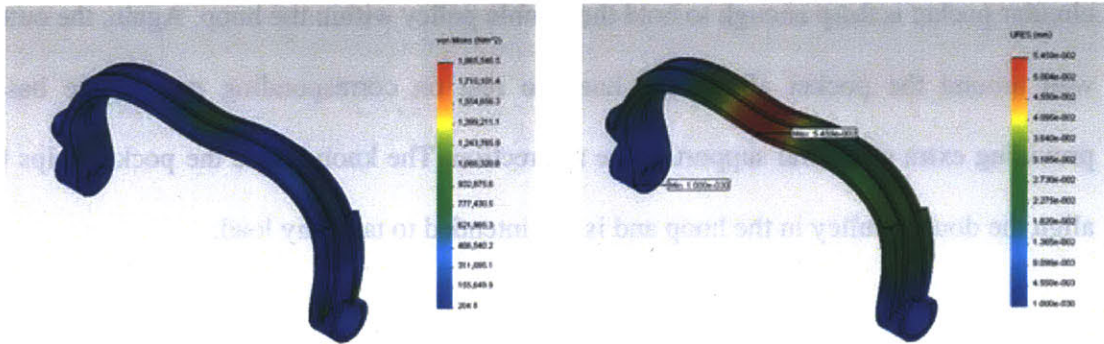


Figure 3-24 FEA result of the hoop under 10 N of load from probe insertion. The max stress calculated is 1.86 MPa, and the max deflection is 0.054 mm.

### 3.2.4 System Modeling Analysis

The Free Body Diagram (FBD) in Figure 3-25 shows the main forces acting on the cable driven system that travels on a curved surface. The torque from the motor,  $\tau_{motor}$ , is applied to the driving pulley. The cables would pull on the driving pulley with forces  $T_1$  and  $T_2$  respectively. As the cable travels on the hoop and wraps around a circular surface, the force required to move the cable increases to  $T_3$ . The tensioning pulley rotates in place, evenly distributing the forces on the cable that goes around it. The hoop, in return, provides a tensioning force,  $F_{tension}$ , on this pulley. The cable again wraps on the hoop, increasing the magnitude of tension to  $T_4$ . The carriage, being pulled on either side with forces  $T_4$  and  $T_5$ , moves to the right and experiences a friction force in the opposite direction.

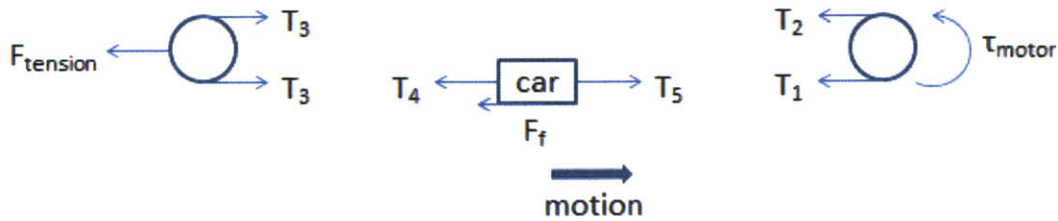


Figure 3-25 Free Body Diagram of the cable drive system.

One source of friction in the system is the sliding friction between the cable and the hoop. Based on Capstan equation, the relationship between  $T_3$  and  $T_2$  is

$$T_3 = T_2 e^{\mu\theta} \quad (3.12)$$

where  $\mu$  is the coefficient of friction between the cable and the hoop, and  $\theta$  is the angle at which the cable wraps around the hoop (90 degree in this case). This coefficient is experimentally obtained in the previous section (0.57). Therefore, the above relationship between  $T_3$  and  $T_2$  can be rewritten as

$$T_3 = T_2 e^{0.895} \quad (3.13)$$

Similar relationships between  $T_3$  and  $T_4$ , as well as  $T_5$  and  $T_1$ , can be determined as well. Here, the angles at which the cables wrap around the hoop change as the carriage travels along the hoop, and as a result, the corresponding forces would also change. For simplicity, the carriage is first assumed to be positioned at the top of the hoop and the cables would wrap about 40 degree in each direction (carriage takes about 10 degree).

$$T_4 = T_3 e^{0.4} \quad (3.14)$$

$$T_1 = T_5 e^{0.4} \quad (3.15)$$

Based on the FBD of the carriage, assuming the carriage is moving in the positive x direction, balancing all the forces yields

$$\sum F_x = T_5 - F_f - T_4 = m_{car} \alpha \quad (3.16)$$

The friction experienced by the carriage traveling on the hoop comes from the friction of the rollers in the bearing. In section 3.1.3, the average force required to move the rolling bearing was measured to be 2.34 N. With the carriage moving almost at a constant speed, this measured force is equivalent to the friction force. The mass of the carriage is about 250 g and the acceleration of the carriage is defined in the functional requirements of the bearing design ( $1 \text{ cm/s}^2$ ). Hence, the above equation can be rewritten as

$$T_5 - T_4 = 2.59 \quad (3.17)$$

The force applied to the tensioning pulley is from the tension in the cable and the force from the bolt. The summing all the forces give

$$\sum F_x = F_{tension} - 2T_3 = \frac{\tau}{kD_{bolt}} - 2T_3 = 0 \quad (3.18)$$



where  $\tau$  is the turning torque from the screw driver,  $D_{bolt}$  is the nominal bolt diameter, and  $k$  is the bolt torque coefficient, which depends on the coefficient of friction, lead and thread angle, and mean diameter of bolt. Usually 0.2 is used for  $k$  when bolt condition is not stated [22] and [23] has reported that 0.208 may suitable for both lubricated and unlubricated bolts.  $\tau$  is estimated to be about 3 Nm based on experiment conducted by [24]. For the 6-32 tensioning bolt, the nominal diameter or major diameter is about 3.5 mm. Therefore,  $T_3$  is solved to be around 2.14 N. From the force equation of the tensioning pulley and the carriage, in addition to the Capstan equations, the forces on the driving pulley,  $T_1$  and  $T_2$ , are solve as 3.86 N and 0.88 N respectively.

Summing the torque around the driving pulley yields,

$$\sum \tau = \tau_{motor} - (T_1 - T_2)r = I_{pulley} \alpha \quad (3.19)$$

where  $r$  is the diameter of the driving pulley (3.4 mm) and  $I$  is the moment of inertia of the pulley ( $1.23 \times 10^{-7} \text{ kg}\cdot\text{m}^2$ , SolidWorks Mass Properties). Based on the equation below and the acceleration of the carriage defined earlier, the rotational acceleration is calculated to be  $12.35 \text{ rad/s}^2$ . Plugging in the known values, the minimum torque required from the motor is 0.007 Nm.

$$\alpha = \frac{a}{R} \quad (3.20)$$

Similar calculation was performed for every carriage position on the hoop. Figure 3-26 shows the resulting minimum motor torque required to actuate the system. When the carriage is at its vertical position, the angle on the hoop is defined as 0 degree. The end of the hoop closer to the cable tensioning mechanism is defined as negative and the end closer to the driving pulley is defined as positive. It is observed that the torque gets larger as the carriage moves closer to the cable tensioning mechanism. This makes sense

because  $T_I$  would increase if more cables were wrapped on the hoop between  $T_I$  and  $T_5$ . The maximum torque calculated was 0.018 Nm, which can be used to find the appropriate actuators for the system.

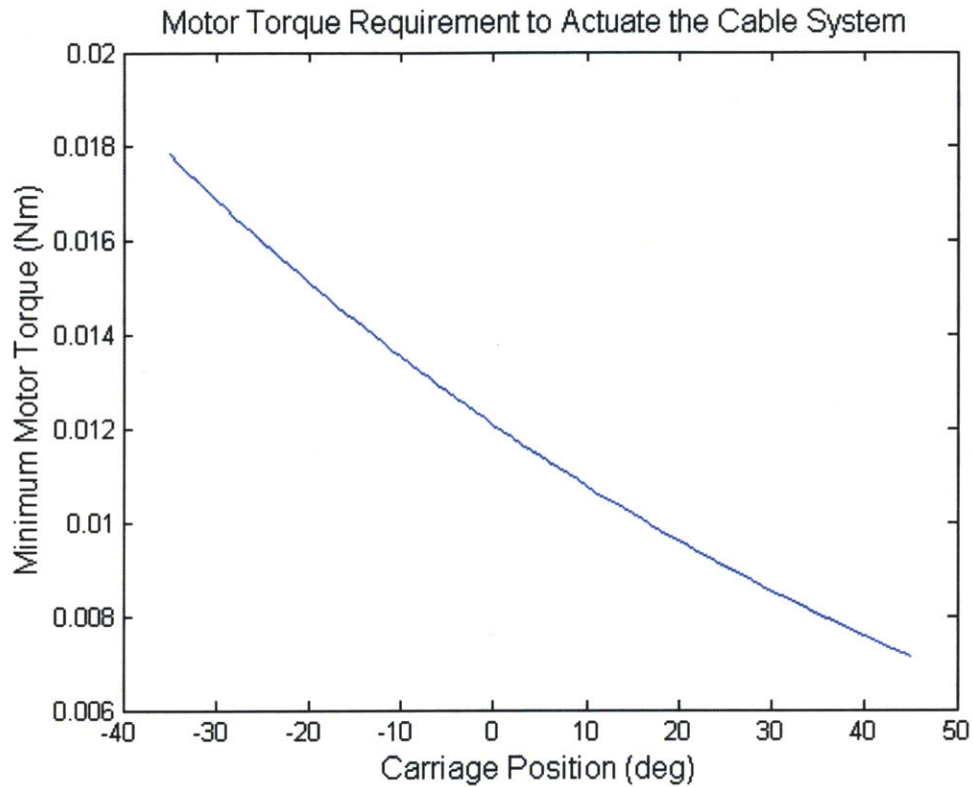


Figure 3-26 Minimum torque required to move the cable system as the carriage moves along the hoop.

### 3.2.5 Movement Bench Level Evaluation

To test the design of the cable drive system, a 2x scale hoop and carriage prototype was made. Once the tensioning mechanism had made the cables sufficiently taut, the carriage could be moved by hand with moderate force. The driving pulley rotating in response exhibited no backlash when the carriage changes direction of motion – a key design requirement. This large scale prototype was also connected to motors and drove with a step input controller, shown in Figure 3-27. The carriage responded to the rotation of the motor with fine movement resolution. Again, no backlash or motor stalling was observed.

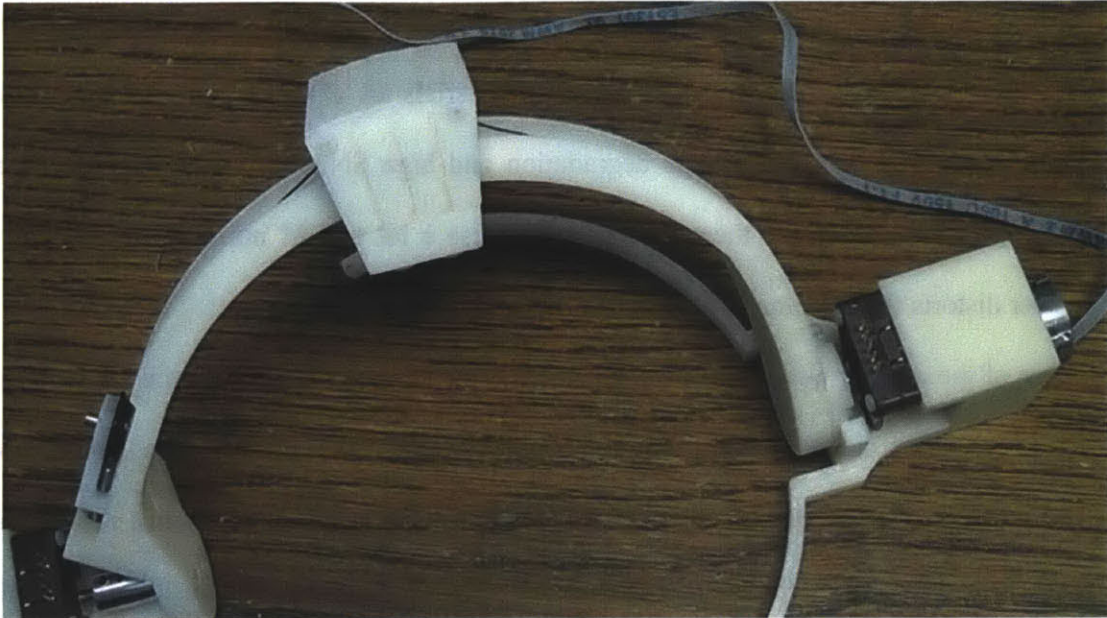


Figure 3-27 Bench level test was conducted on a large scale hoop and carriage model. The actuated movement exhibited no backlash and required relatively low force.

### **3.3 Actuator and Encoder Selection**

Conventional actuators cannot be used because they are not MRI-compatible. Therefore, special actuators must be selected to ensure that they would operate as designed in the MRI environment, cause zero or limited image distortion, and be safe to use around patients. Ultrasonic actuators are the predominant actuator used in MRI compatible manipulators, available in both linear and rotary motion. It creates movement based on resonant vibrations of non-magnetic piezo-ceramic materials [25]. It has fast response time to command and can produce precise positioning. Ultrasonic actuators are relatively light and compact, with almost no backlash. It becomes rigid during power failure, making it safe for medical usage.

On the other hand, ultrasonic actuators require high frequency power supply. The movement of these motors depends on friction, which causes their durability to be lower than other MR compatible actuators. Ferrous materials are often embedded inside these motors, resulting in severe image degradation and high SNR reduction. The electrical components used to drive these motors also cause a lot of EM noise emission, which further distorts the MR image [26].

One of the countermeasures for the above problems include turning off the motor when scanning, which prohibits real time monitoring of the device with MR image feedback. The motor and associated electronics can also be placed outside the control room or at least 1 m away from the imaging bore; but the long cable and transmission would decrease rigidity of the mechanism and introduce delays and errors. Specially designed filter and shield can help reduce SNR and EM noise.

Hydraulics has been used in certain cases for MR compatible devices. It is a closed system without a pump, using pre-pressured fluid inside of pipes to provide force and motion transmission, and has no transmission delay even over a long distance. However, it does have a high level of static and dynamic friction that vary with speed, acceleration and temperature, which may significantly affect the behavior of system. Longer hoses would also reduce system efficiency and further add to its non-linear behavior. Doctors have expressed concerns about patient safety in case of power failure or liquid leaks contaminating sterile environment. Counter measures for these risks include combining ultrasonic motor (placed outside of MRI) and hydraulics to shorten hose length and using master/slave hydrostatics for long distance motion transmission.

Pneumatics is also MR compatible. It uses air pressure to transmit force over long pipes just like hydraulics. Compressed air supply is usually available in operation rooms, and the pipe can also be lead out of the imaging room to an external air reservoir if needed. Pneumatics contains no ferrous materials, hence doesn't produce EM noise. Nevertheless, without the ability to hold position during power failure, doctors are concerned about patient safety when pneumatics is used. It is hard to achieve precision position control with pneumatics since it is pressure driven. Regulating fluid from a pressure source is also difficult to accomplish as reported by [27]. Special stepping mechanisms need to be used with pneumatics to retain fine movement control, as with the case of LPR [10].

Piezoelectric motors can provide both linear and rotatory motion. It works by acoustic or ultrasonic vibrations when electric field is applied to the ceramic material inside [28]. Piezoelectric motors are fundamentally stepper motors/nanomotion motor, with very precise position control. It also has high frequency response with virtually no delay. However, it presents higher SNR reduction in lower magnetic field (1.5T compared to 3T), which means when used in weaker magnetic field, either more scans should be done or specially designed filter should be applied to reduce SNR reduction [26].

Other exotic alternatives are Electrostatic Motor, Electrostrictive Polymer Actuators (EPAMs), which are still under development and may not be appropriate for this project. Piezo LEGS rotatory motor (Piezomotor, Sweden) and USM ultrasonic motor (Shinsei, Japan) are two widely used non-magnetic actuators that have been reliably tested by other robotic mechanisms (Figure 3-28). Based on conversation with the manufacturer and researchers from WPI who have extensive experience with MRI compatible actuators, a comparison table (Table 3-2) is made. Because of its smaller size, cheaper cost, larger

torque capacity, and shorter lead time, LEGS rotatory motor from Piezomotor was selected for this device.

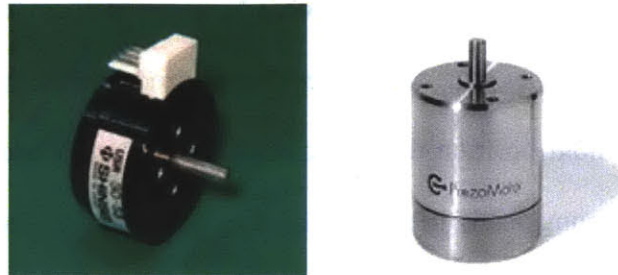


Figure 3-28 Non-magnetic actuators. Left: Shinsei ultrasonic motor. Right: LEGS rotatory piezoelectric motor.

Table 3-2 Comparing specifications between actuators from Shinsei and Piezomotor

Manufacturer	Shinsei	Piezomotor
Resolution	6.3 $\mu$ rad	<1 $\mu$ rad
Voltage	12 V	48 V
Mass	90 g	60 g
Stall torque	19.6 mNm	50 mNm
Hold torque	19.6 mNm	55 mNm
Rated speed	Min 3.33 rad/s	0-20 rpm
Size	$\varnothing$ 43 mm x 28.5 mm	$\varnothing$ 23 mm x 34.1 mm
Lead time	1.5~2 month	4 week
Unit cost	\$3562.50	\$1427.60

The piezoelectric motor does not have position control capabilities by default. Therefore, an encoder module was obtained from US Digital (Vancouver, WA) to help perform closed loop control. Illustrated in Figure 3-29, the encoder contains a

transmissive optical encoder module, a 1" diameter transmissive disk, and an incremental differential encoder cable driver. Every component in the encoder is MRI compatible, except for a 4-48 set screw for securing the disk, which can be easily replaced. The complete electrical control loop is illustrated in Figure 4-8.



Figure 3-29 Encoder module from US Digital is used with the piezoelectric motor to perform closed loop position control. Left: Optical Encoder module. Middle: 1" diameter encoder disk. Right: Incremental differential encoder cable driver.

### **3.4 Base**

The base determines the overall structure and form factor of the robot. It accommodates the shape of an imaging loop coil, houses fiducial markers to register the initial location and orientation of the device, and supports the motion of the hoop. The electrical components selected in the previous section also need to be mounted to the base. This section shows the detailed design of all the components described above.

#### **3.4.1 MRI Coil-Mounting Design**

As illustrated in section 2.2, the loop coil selected is 19 mm thick and has an OD of 137 mm. Therefore the base, a flat thin-walled structure, is designed to cover this specific coil while minimizing the space being occupied in the MR imaging bore (Figure 3-30). The wall of the base is 2.5 mm to maintain a reasonable structural support. The center of the base contains a large window, providing interventionists with enough space to perform

tasks near the probe entry point, such as making a skin incision to facilitate insertion and manually adjusting the probe after it has been released. A rectangular opening on the side of the base constrains the rotation of the base and frees the cable in the coil to be plugged into the MRI machine.

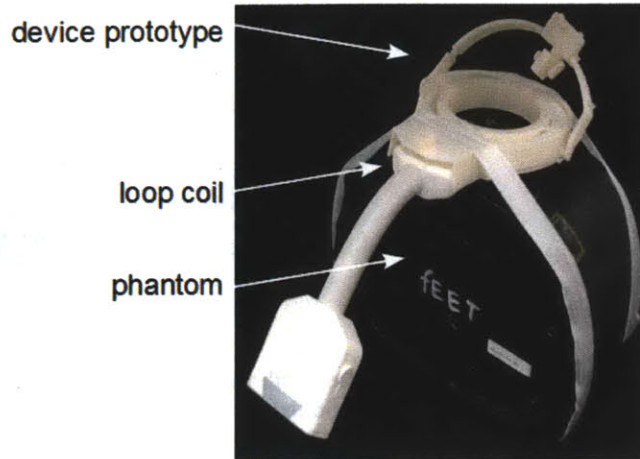


Figure 3-30 The device contains a thin walled base and mounts onto a loop coil. Here, the device is shown mounted on top of an imaging phantom.



Figure 3-31 Anchors on the side of the base are designed for attaching the robot to patient.

There are anchors on the side of the base for attaching the robot to the patient, as shown in Figure 3-31. Tape or Velcro can loop around these ear shaped anchors and pull down on the device to secure it. FEA analysis was performed on the ears (Figure 3-32). The



maximum stress experienced is 1.9 MPa and the maximum deflection is 0.018 mm, which are acceptable for the base which is 3D printed in ABS like material.

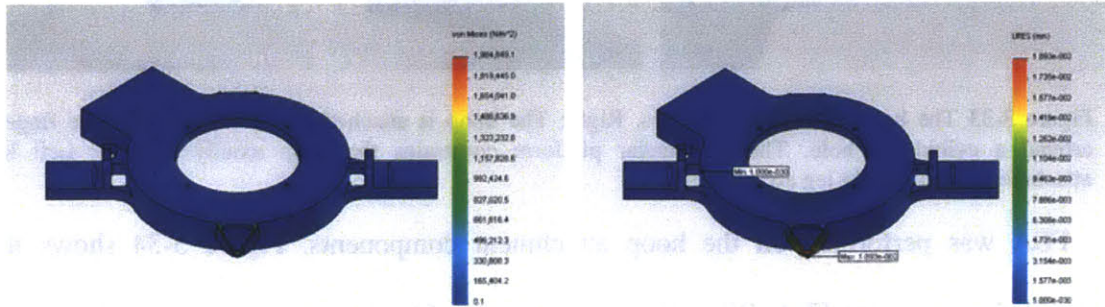


Figure 3-32 FEA analysis of the anchors on the base. Maximum stress is found to be 1.9 MPa, and the maximum deflection is 0.018 mm,

### 3.4.2 Hoop Attachment

As discussed in section 3.2.3, the hoop legs have cylindrical ends to facilitate rotation movement. The corresponding hoop attachment features on the base is illustrated in Figure 3-33. The attachment feature has a cylindrical concave surface to mate with the rounded ends of the hoop. The concave surface extends upward to two flexure fingers. The hoop can be snapped onto the attachment feature via the opening between the fingers. An 8 mm thick rectangular platform extruding out of the mating feature is used for attaching the motors. This platform interferes with the flat face of the hoop leg, constraining the hoop position axially. The two sides of attachment feature are slightly different, accounting for the space needed for tensioning the cable system on the left leg.

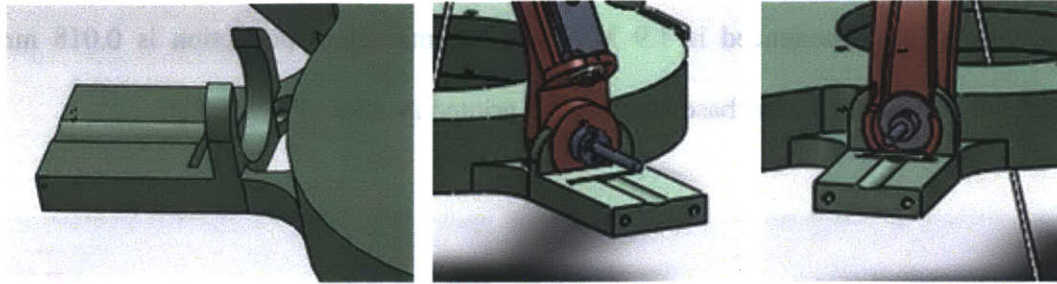


Figure 3-33 The hoop attachment features. Right: The hoop is attached to the base via flexure fingers around a cylindrical hole. The rectangular platform constrains the hoop axially. Middle: Left leg attachment. Right: Right leg attachment.

FEA was performed on the hoop attachment components. Figure 3-34 shows the detailed result of the FEA. When fixing the bottom of the base and applying 5 N from the top to each of the attachment parts (evenly distributing the needle insertion force between the two legs of the hoop), the maximum stress experienced at the bottom of this interface is about 222 KPa and the maximum deflection is about 0.06 mm. When pushing the hoop into the mating flexural fingers with 10 N, the maximum stress in the finger is 4.64 MPa and the max deflection is 0.018 mm. Both calculated stresses are well below the limit of 3D printed ABS like material. The deflection from needle insertion force is small enough to not affect the alignment of between the actuators and the hoop. The deflection of the fingers is within the movement interference designed between the hoop end and the attachment feature to create a snap fit.

The hoop attachment is rotated 45 degrees off the central axis of the base to enable the hands of the interventionist to access the center of the base from either side of the hoop. For simplicity, the coordinates of the robot are rotated as well: x-axis now coincides with the center of the hoop attachment feature, y-axis is perpendicular to it (in the direction of the anchors on the base), and z-axis points up vertically.

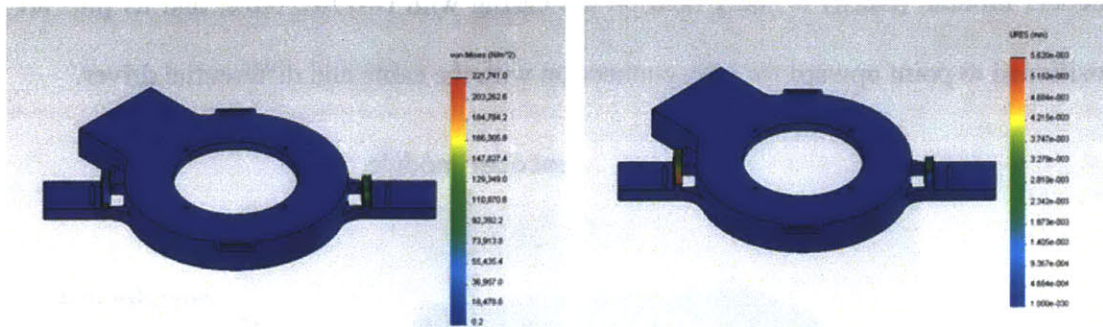


Figure 3-34 FEA conducted on the hoop attachment components. The maximum stress caused by needle insertion force on the bottom of the mating feature is about 222 KPa. The maximum deflection is about 0.006 mm. The maximum stress caused by the snapping fit in the finger is 4.64 MPa and the max deflection is 0.018 mm.

### 3.4.3 Actuator and Encoder Attachment

The actuation assembly was designed to provide sufficient structural support and enable modular attachment. Since the electronics are difficult to clean with normal hospital sterilization procedures, enclosing them in a single removable and coverable casing could help drive the cost down and ensure sterility.

Figure 3-35 shows the design of the actuation assembly on the base. A modular plastic casing (purple) can be attached to the base (green) with two M3 bolts (not shown). The motor is held inside of the plastic casing (purple) with two plastic M2 bolts. A misalignment coupling (pink) connects the motor shaft (3 mm diameter) with a 3 mm diameter aluminum extension shaft, providing stiff rotation support while being flexible if misalignment of shaft occurs. The misalignment coupling (Figure 3-36) connects to a shaft via integral clamp collars that are tightened with two socket-head cap screws. This type of collar won't damage the motor shaft like a set screw would. The extension shaft is supported by the misalignment coupling on one end and the hoop (not shown) on the other. The encoder disk (yellow) is tightened onto the shaft with a 4-48 set screw. The

encoder module (black) is being held on the casing with two M2 bolts, and its pins are positioned to point upward for easy connection with the cable and differential driver.

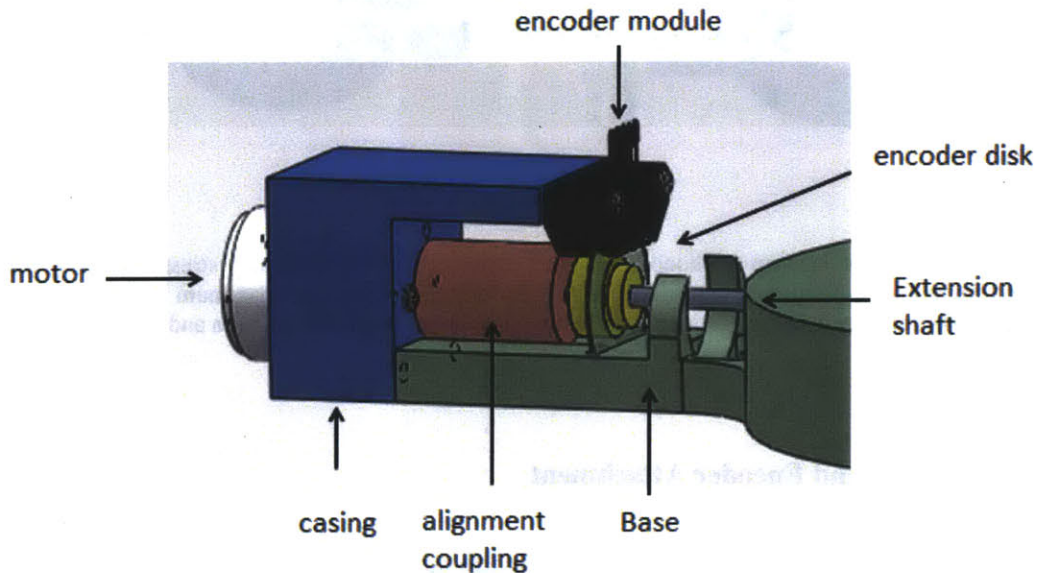


Figure 3-35 The assembly and attachment of electronic components on the base. The motor attaches to a removable casing and the shaft is extended with a flexible coupling. Encoder module is subsequently mounted on the extension shaft, with the other end of the shaft connect to the hoop or the driving pulley.



Figure 3-36 Misalignment clamp on coupling is used to connect an extension shaft to the motor shaft [<http://www.mcmaster.com>]. This type of coupling holds onto a shaft with integral clamp and won't damage the shafts like a set screw.

The motor holder casing is designed to have enough wall thickness to rigidly hold the motor (23 mm diameter) and enough space for bolt attachments to the base. It is also designed to keep the remote center of motion of the device as close to skin as possible to minimize the length of the incision. The center of the motor, or the x-axis of the robot coordinate, is positioned 15 mm above skin as a result. The rectangular platform on the

base to which the casing is attached is sufficiently thick to allow M3 holes to be tapped. However, at this height, the encoder disk and the misalignment coupling would interfere with the platform. Circular slots are cut in the platform to provide clearance for these two components to rotate, as illustrated in Figure 3-37.

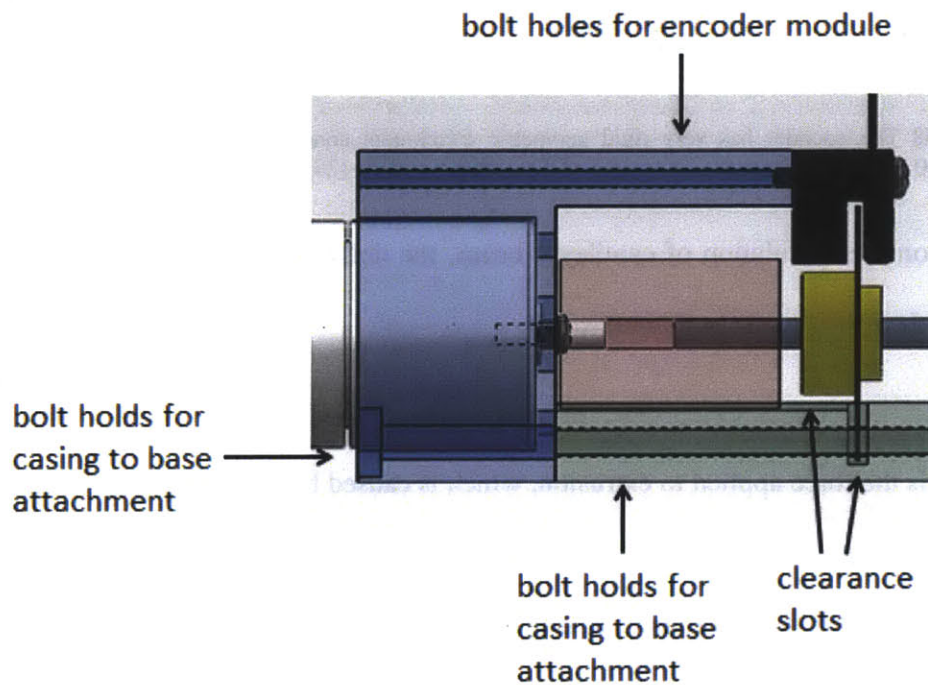


Figure 3-37 Slots for encoder disk and misalignment coupling are made on the rectangular platform to provide clearance for the parts to rotate without interference.

The size of the motor assembly is governed by the length of the misalignment coupling (15 mm), the thickness of the encoder module (0.398 in), the thickness of the encoder disk (7.8 mm), and the maximum allowable distance between the encoder disk and the encoder module specified by the manufacturer for the encoder to work properly (Figure 3-38). Hence, the casing must be 46 mm away from the hoop attachment feature, and the extruded beam on top of the casing to hold the encoder module must be 24 mm long.

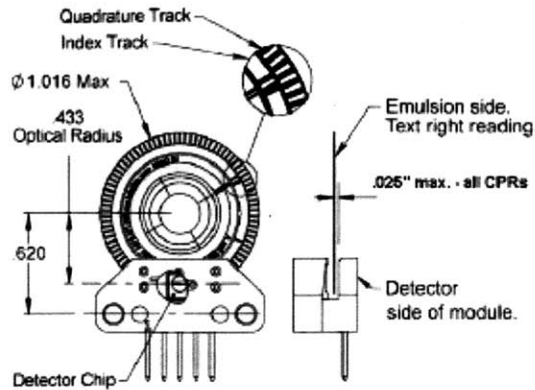


Figure 3-38 The encoder has very rigid geometric attachment constrains. The disk must be placed a maximum 0.025" away from the inner edge of the encoder module [29].

Based on the calculation of cantilever beam, the deflection of the extrusion beam for securing the encoder can be found from

$$\delta = \frac{-PL^3}{3EI} \quad (3.21)$$

where  $P$  is the force applied to extrusion, which is caused by inserting the cable and cable driver into the encoder module.  $L$  is the length of the extrusion,  $E$  is the Young's modulus of the plastic, and  $I$  is the moment of inertia of the extrusion, which is

$$I = \frac{bh^3}{12} \quad (3.22)$$

where  $b$  is the thickness of the extrusion (30 mm) and  $h$  is its height (5.588 mm). The moment of inertia is found to be  $4.36 \times 10^{-10} \text{ m}^4$ . Estimating the inserting force to be around 5 N, a maximum deflection of  $0.22 \text{ } \mu\text{m}$  is found.

The stress on the extrusion can be calculated from

$$\sigma = \frac{My}{I} \quad (3.23)$$

where  $M$  is the maximum moment on the extrusion and  $y$  is the distance from the center of the extrusion to its upper most surfaces (2.794 mm). The maximum moment is at the end of the extrusion, which is

$$M = PL \quad (3.24)$$

or 0.12 Nm. Hence, the maximum stress in the extruded beam is 0.77 MPa. The stress calculated shows the extrusion on the motor holder casing can support the force applied to it when the cable and the driver are plugged into the encoder module. The deflection of the part will not affect the encoder's sensing capabilities.

The aluminum extension shaft is also analyzed. Because the alignment coupling maintains the axial position of the shaft but allows small amount of flexing, the shaft can be modeled as a cantilever beam when the flexing angle is small. There are two external forces applied on the shaft. The weight of the encoder disc,  $P_1$ , applies a downward force on the shaft. Depending on which side of the hoop the shaft is attached to,  $P_2$  can be a downward force from the weight of the hoop or an upward force from the cables pulling up on the driving pulley. The weight of the encoder disc and the weight of the shaft are negligible in comparison to the load from the moving components. In the worst case scenario, the double pulley applies 4.64 N to the shaft upward. The same equations for deflection and stress can be used, only changing the modulus of elasticity to that of aluminum (68 GPa),  $L$  to the length of the shaft (30 mm), and  $I$  to that of a round with 3 mm diameter, or

$$I = \frac{\pi r^4}{4} \quad (3.25)$$

The deflection is found to be about 0.154 mm, which is easily compensated with the misalignment coupling. Again, the maximum moment on the shaft is on the fixed end farthest away from the load or the end connected to the alignment coupling, which is 0.14 Nm. The highest stress occurs on the edge of the shaft, or  $y=r$ . The stress calculated is 52

MPa, much less than the aluminum yield strength of the shaft or the alignment coupling.

Hence, a 3 mm diameter aluminum shaft is appropriate for this application.

### 3.4.4 Registration Marker Placement

The inner wall of the base contains three layers. Six 6 mm spherical PinPoint fiducial markers from Beekley (Bristol, CT), exhibited in Figure 3-39, are sandwiched between the layers as registration markers. The distance between any two fiducial capsules is unique, enabling a registration algorithm, being developed by Atsushi Yamada from BWH, to quickly identify the orientation and location of the device in the image coordinate system. Figure 3-40 shows the placement of each fiducial marker in the three layers of the base.

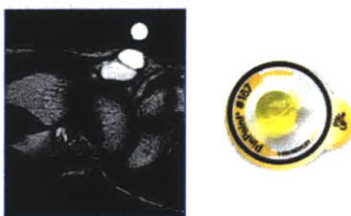


Figure 3-39 PinPoint Fiducial marker used for registration. Left: The fiducial shines brightly in MR image to work as a registration marker. Right: The 6 mm spherical marker from Beekley [<http://www.beekley.com>].



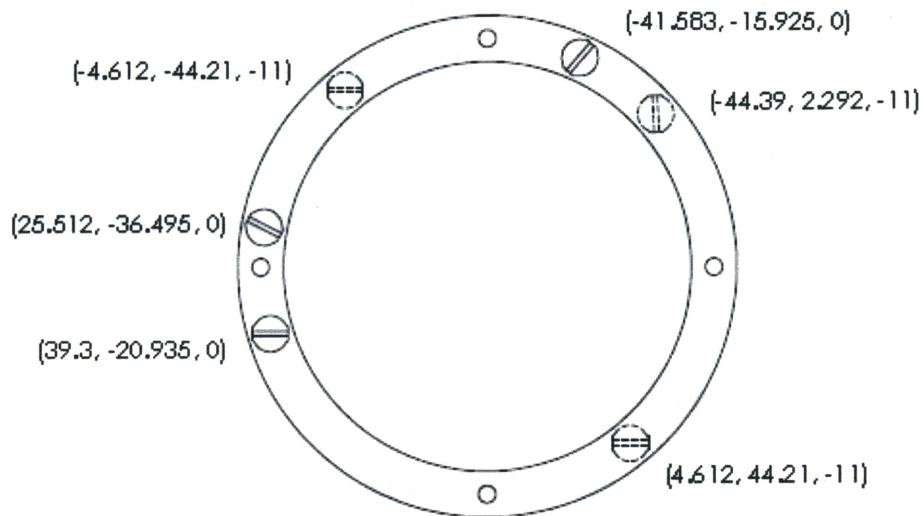


Figure 3-40 Fiducial marker placements in the base. Fiducial placed between the top layer and the middle layer is illustrated in solid lines and fiducial between the middle layer and the bottom layer is indicated with dotted lines. The distance between any two points is unique, enable registration algorithm to pick up the position and orientation of the device.

A prototype of the base embedded with registration markers was made and scanned in MRI and CT to test the registration module written to interface with medical imaging software. Figure 3-41 shows the testing set up. For CT, the fiducial markers do not show up in the image. Spheres of other material were tested. Glass and aluminum spheres were found to shine very brightly in the CT image without causing significant distortion.

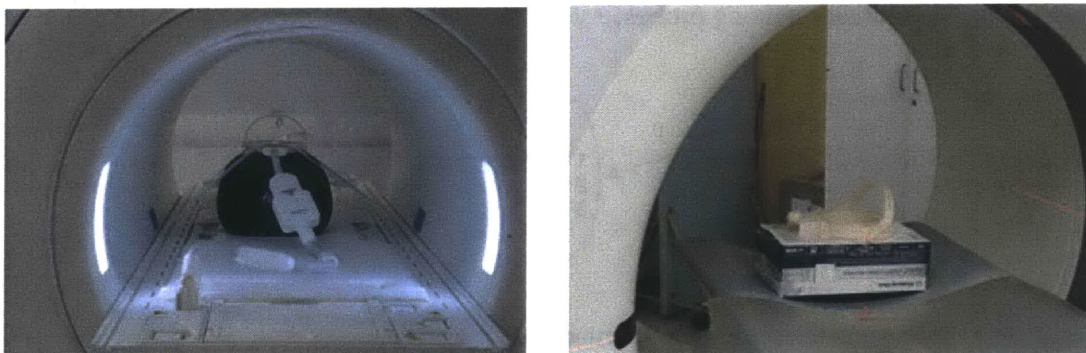


Figure 3-41 A prototype base embedded with registration markers as tested in MRI and CT to obtain images for analyzing registration algorithm and implementing the registration module into medical imaging software. Left: MRI scan. Right: CT scan.

### 3.5 Needle Holder

On the carriage, special features need to be designed to hold and release the probe. The needle holder should be able to accommodate up to three probes and be easily manipulated with gloved hands. At this stage, interventionists prefer to manually insert the probe for patient safety; hence a passive probe holder and release mechanism as made.

#### 3.5.1 Probe Track Design

Since probes cannot physically intersect, the remote center of motion only can coincide with one of the probes, while other probes must have guides that are slightly shifted to the side of the first probe. Furthermore, the probes should line up along the incision on skin (Figure 3-42), following conventional procedure practice. The needle holder, therefore, is designed to contain three needle tracks to guide the paths of different probes (Figure 3-43). The middle track points toward the origin of the device coordinate system, so the probe going through it would pivot about the intersection of the rotation axes. The first and third tracks are shifted 3 mm from the middle track in opposite directions to avoid possible collision among probes.

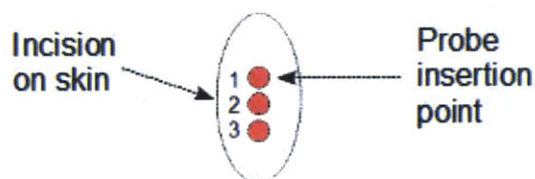


Figure 3-42 Probes are positioned to allow insertion along the incision.

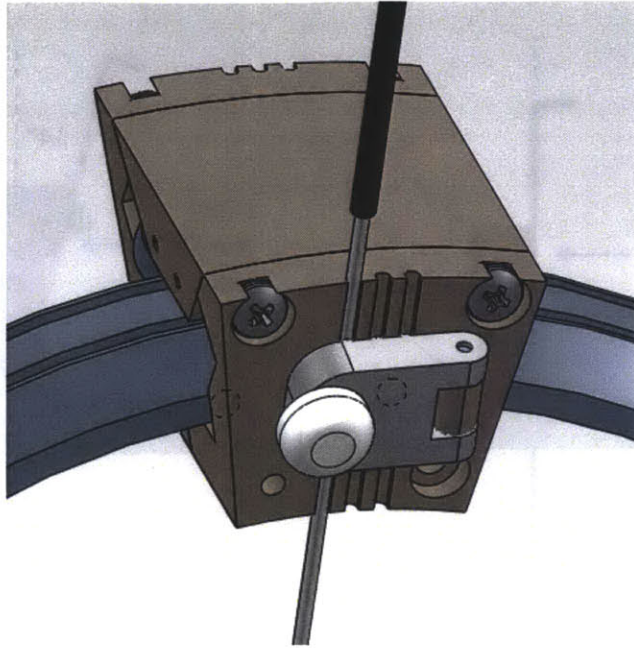


Figure 3-43 There are three tracks on the carriage separating the probes in order to prevent them from intersecting or colliding. A thumbscrew and latch combination is used to preload and lock the probe in place.

Since the carriage and the hoop physically take up space, some offsets are needed to align the probe with the origin properly. Figure 3-44 shows two different concepts to achieve such offset. The hoop legs can be bent in one direction, so the carriage wall holding the probe would coincide with the z-axis when the hoop is upright. The other idea is to tilt the needle track to radially point towards the x-axis. When testing the cable system, it seemed to be more difficult to keep the cables in its groove if the legs of the hoop are bent. A straight hoop would require simpler geometry and groove design, and allow the hoop a larger range of motion. Therefore, the needle tracks are designed to have a tilt of 14 degree from vertical.

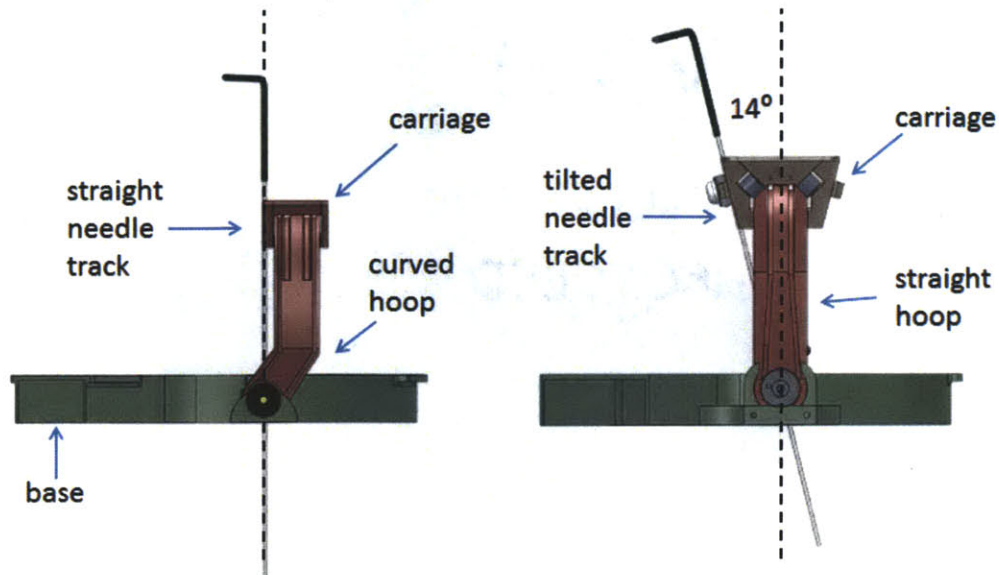


Figure 3-44 Two designs to align the needle tracks with the remote center of motion. Left: The hoop is bent so the carriage wall holding the probe coincides with the x-z plane. Right: Needle tracks point radially inward to keep a straight hoop profile. For simpler hoop design, the tilted need track idea was selected.

When a needle tilts, its projected cross sectional area relative to the X-Y plane of the device is non-circular, as shown in Figure 3-45. The same principle applies to the needle tracks. Since the carriage has round surfaces, a sweep cut was used to make the needle track feature in SolidWorks. The path of the sweep was made simply with a 2D sketched line that is 14 deg off vertical. The profile, however, was drawn on the top plane, where the remote center of motion of the device is located. The contact area between the needle and this plane would be an ellipse with a major axis proportional to the rotation angle (in case is 14 deg) and the minor axis equal to the diameter of the needle.

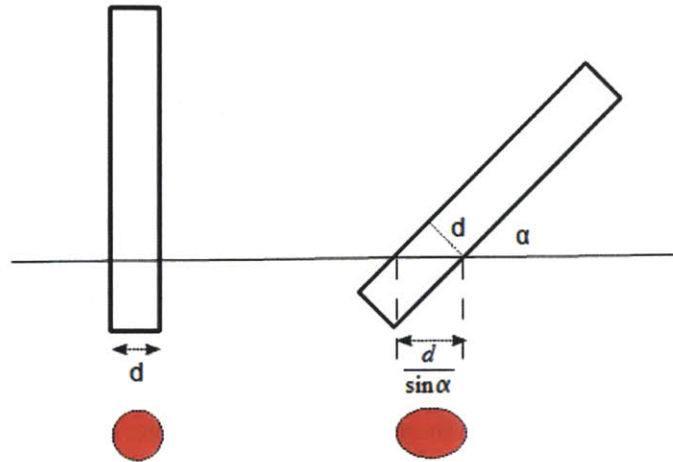


Figure 3-45 The projected cross sectional area of a needle (or needle track) varies as the needle rotates.

### 3.5.2 Needle Preload and Release

Shown in Figure 3-45, the probe release mechanism contains a latch and a thumb screw. The probes are secured to the carriage from the side, enabling them to be easily engaged and disengaged by hand. The thumb screw fastens the latch on the carriage and keeps the probes in place. Once an insertion is completed, the thumb screw loosens to open the latch completely. The probe placed in one of the needle tracks can be released simply by actuating the carriage and the hoop to the next position. The hoop should always rotate clockwise about x-axis (from the cable side of the imaging coil to the non-cable side) to avoid colliding with previously placed probes.

The inner diameter of the needle tracks are the same as the diameter of the needle. Three bumps are put on the latch to help preload the needles in the carriage. When the latch is closed, the bumps are physically inside the probe tracks, as shown in Figure 3-46 (Left). Friction and compression secures the probes inside the tracks. Estimating the

torque from the thumb screw to be around 1 Nm, the force keeping the probes in place can be calculated from

$$F_{secure} = \mu F_{bolt} = \mu \frac{\tau_{bolt}}{kD_{bolt}} \quad (3.26)$$

where  $\mu$  is the coefficient of friction between the probe and the needle holder, which is about 0.37 for ABS on steel. The force is found to be 0.65 N, which is sufficient to balance the downward force caused by the weight of the probe.

The latch is designed to be more than 10 times the diameter of the probe, to help guide the probe more rigidly and avoid possible jamming during the insertion process.

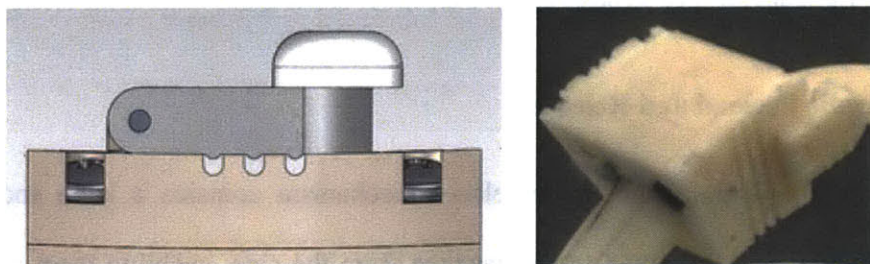


Figure 3-46 Needle release and preload mechanism. Left: The latch contains bumps to preload the needles in the holder. Right: Once the latch is opened, the probes are released simply by actuating the carriage to the next position.

### 3.5.3 Needle Holding and Releasing Bench Level Evaluation

The functionality of the needle holder was tested by inserting a 17 gauge probe in the track, as shown in Figure 3-47. When the thumb screw is fastened, the holder was able to successfully grab the probe and keep it in position. The thumb screw is small, requiring nimble hands to open and close the latch. Moving the carriage away after the latch is opened essentially released the probe without any additional effort. Inserting the probe in air along its track did not require much force and the probe was able to stay in its path, until a lateral force is applied to the tip. Probe bending in tissue cannot be avoided, which may contribute to targeting error. Increasing the height of the latch to 20 times the probe

diameter or adding additional probe guidance support at the bottom of the base may help reduce the error. Incorporating steerable ablation probes into the design would further solve the problem [30].

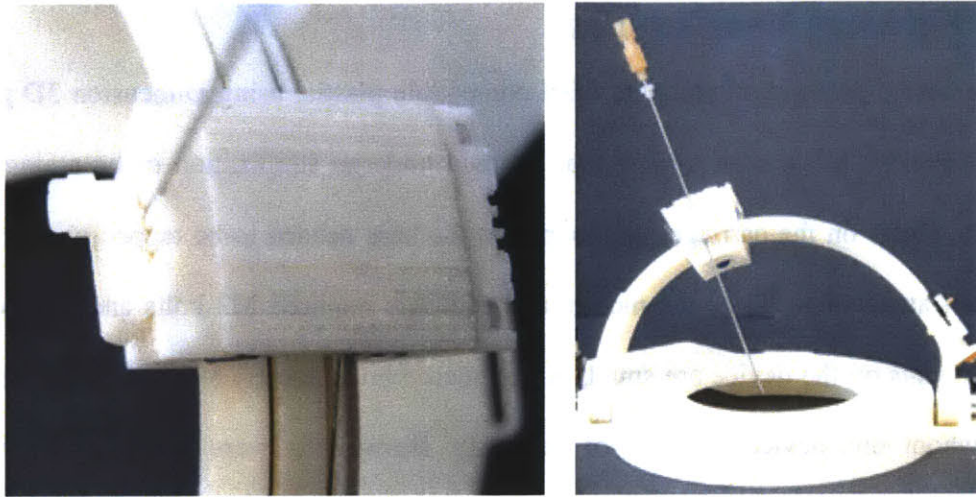


Figure 3-47 Probe holding and releasing test proved that the needle holder can keep the probe in place, guide its trajectory, and free it from restriction when insertion is completed. Left: Close up view of needle holder and the probe. Right: Probe held in place by needle holder.

# Chapter 4

## Prototyping and Control Implementation

### 4.1 Hardware Manufacturing

The device was prototyped with MRI compatible plastic, using Dimension 3D printer (Eden Prairie, MN), with a view that it could undergo sterilization or be a single-use device. Holes on the carriage, the hoop, and the base needed to be tapped post printing for bolt attachment. Since the motors and encoders required M2 bolts and most of the components on the device are small, plastic metric bolts, mostly M2 and M3, were used throughout this device for ease of assembly. Brass bolts were put in places where stronger hold is required, such as the clamping bolts that tighten the alignment coupling onto the shafts.

A clearance of 0.4 mm was generally put in between the mating 3D printed parts to create a good physical fit. For the carriage, 0.6 mm interference was designed between the roller bearings and the hoop to account for inaccuracy of the printer and guarantee that the rollers would touch the surface of the hoop. Since the bearing walls are slanted to account for the tilt in the needle path, the surface of the carriage appeared to be more porous and layered than usual. However, this porous surface did not affect the performance of the needle insertion test. A small piece of extra material at the bottom edge of all the holes was needed to be removed with a knife to properly fit the pins and bolts.

The encoder, driving pulley, and hoop hub were secured to the extension shaft with brass set screws. With a round shaft, a large amount of torque was needed to sufficiently



tighten the set screws. Brass is often too soft and the hexagonal drive head tends to strip under such load. A flat surface was machined on the shafts to increase the contact surface between the set screw and the shaft, and, as a result, decrease the torque needed to secure those moving components onto the shaft.

Assembling the cable drive was very time consuming and prone to mistakes. Two long pieces of cable were first secured to the driving pulley with the knot-in-hole technique described in section 3.2.2. Since the cable is slippery, a double, and sometimes triple, figure-eight-knot was needed to create a non-slipping and large size knot. The carriage was then moved to one end of the hoop, and the free end of one of the cables was secured to the carriage. The cable was threaded so the knot is on the vertical side of the carriage (Figure 4-1). The triangle between the cable, the carriage, and the hoop was therefore small, optimizing the force output from the cable to be mostly pointed in the direction of the carriage's motion. This cable should be at its extreme position, meaning there was a very short amount of cable wound up in the driving pulley. Then the carriage was moved to the other end, wrapping this already attached cable around the driving pulley in the process. The second piece of cable on the driving pulley was then threaded under the top wall of the carriage, around the tensioning pulley and attached to the other side of the carriage. This was the other extreme position, meaning the amount of wound up cable in the driving pulley from this section should be minimized. Once the cables were properly attached and extra cables were cut off, the pulley was put in the pocket in the hoop. The tensioning bolt was turned until the cables were taught. Finding the correct cable length for each section was an iterative process, and threading the cable through the small holes

on the pulley/carriage before making the figure-eight-knots required sharp tools and a lot of patience.



Figure 4-1 Cables are attached to both sides of the top carriage wall with double figure-eight-knot locked in 90 degree holes. The knot is on the vertical wall of the bearing, allowing most of the force of the cable to transmit to the direction of the carriage's motion.

Aligning and connecting the motor with the encoder and the hoop would also take practice. The motors were first bolted into the motor holder casing. Then the alignment coupling, already attached to the extension shaft, was clamped on the motor shaft. Next, the encoder disk was put on the extension shaft without tightening the set screw. The encoder module was then brought down from top, sandwiching the encoder disk between the module's two inner faces, and bolted onto the casing. Making sure that the encoder disk was less than 0.025" from the thinner side of the encoder module, the disk could then be tightened onto the shaft with a set screw. The extension shaft was put into the hole in the hoop hub or the driving pulley for alignment. Next, the whole motor assembly (from both sides of the hoop) was lowered onto the base, with the encoder disks sitting in the appropriate slots made in the base. Finally, the motor holder casing was attached to the base with M3 bolts and the set screws connecting the extension shaft to the moving component (hoop hub or pulley) were tightened. Figure 4-2 shows the final assembly of the 3D printed prototype.

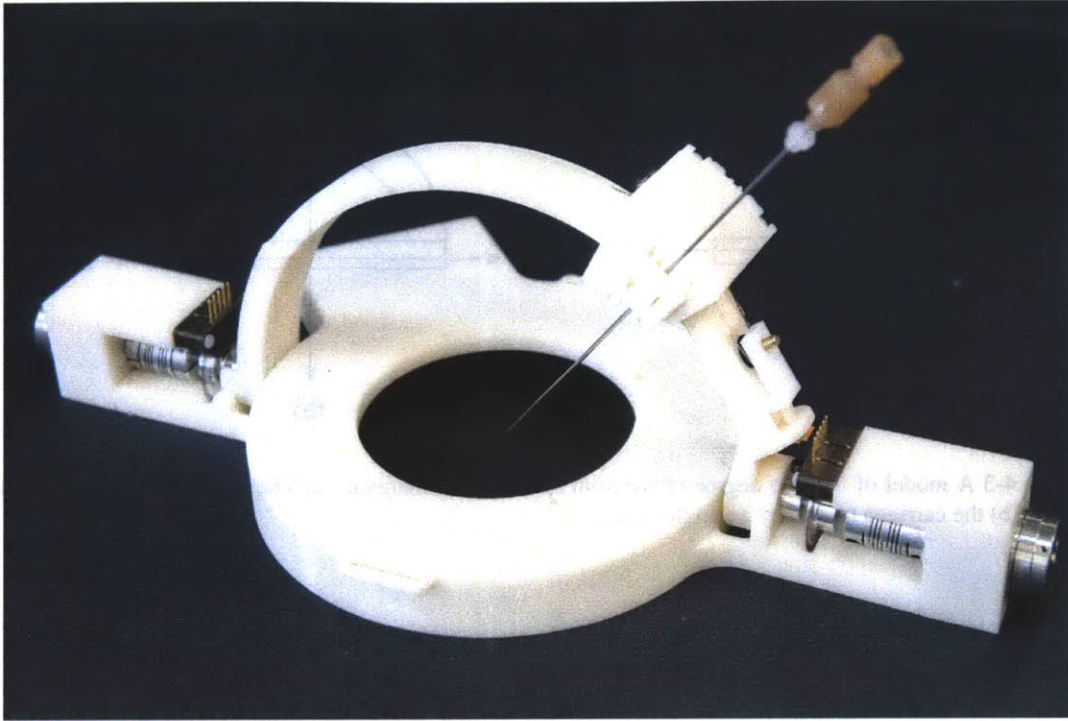


Figure 4-2 3D printed prototype of the device.

## 4.2 System Kinematics

A simple model is developed to analyze the forward and inverse kinematics of the robotic system. The model consists of a rotating arc (hoop) and a mass (carriage) that travels along the arc. The system has two degrees of freedom, as shown in Figure 4-3, with  $q_1$  being the angle of the arc from its vertical position and  $q_2$  being the angle of the mass from the center line of the arc. For both angles, rotation to the right side of the centerline is defined as positive. Figure 4-4 illustrates the two angular variables in 3D space.

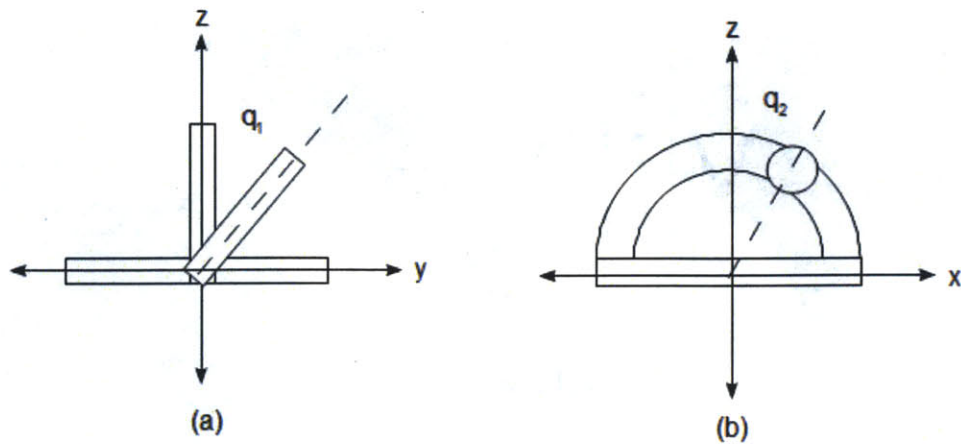


Figure 4-3 A model of the two degree of freedom spherical mechanism. (a) The arc rotates by an angle of  $q_1$  and (b) the carriage rotates by an angle of  $q_2$ .

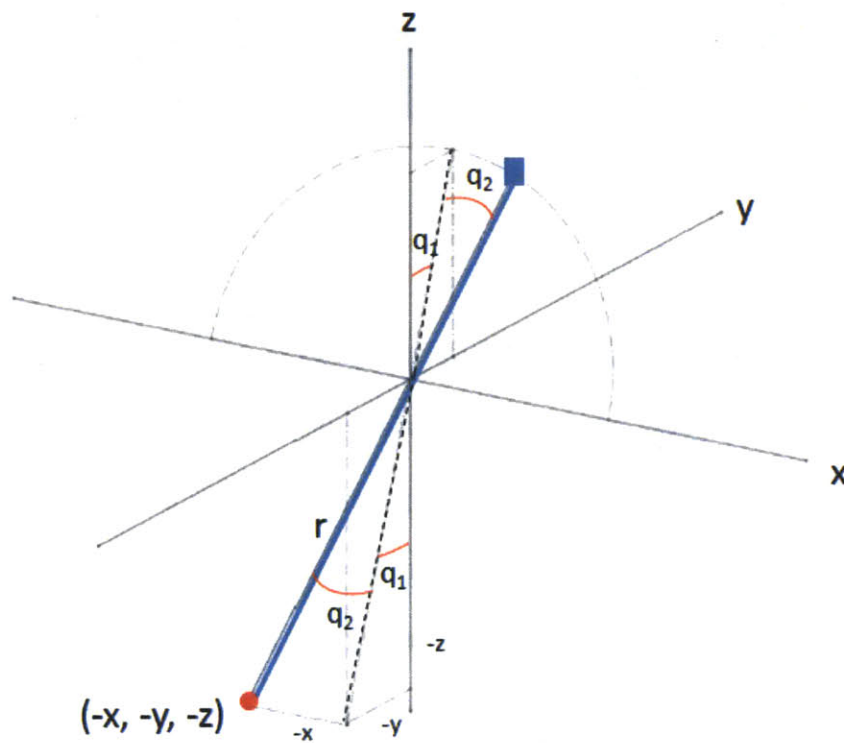


Figure 4-4 Device coordinate system. X-axis is along the center of the motor shaft. Y-axis is along the direction of the base anchors. Z-axis points up vertically.

The semicircle in Figure 4-4 represents a rotated arc and the blue square on the semicircle is the moving mass. The blue line (probe) connecting the moving mass to the

target point (red circle) goes through the remote center of motion, which is the origin of the device coordinate. According to Vertical Angle Theorem, if the arc is moved by  $q_1$  and the mass by  $q_2$ , the target point with coordinates  $(-x, -y, -z)$  would be  $q_1$  away from the z-axis and  $q_2$  from the arc center line (dotted line) in the opposite direction. The forward kinematics of the system is therefore

$$x = -r \sin q_2 \quad (4.1)$$

$$y = -r \cos q_2 \sin q_1 \quad (4.2)$$

$$z = -r \cos q_2 \cos q_1 \quad (4.3)$$

Similarly, the inverse kinematics can be expressed as

$$q_1 = \tan^{-1} \left( \frac{y}{z} \right) \quad (4.4)$$

$$q_2 = \sin^{-1} \left( \frac{-x}{r} \right) \quad (4.5)$$

$$r = \sqrt{x^2 + y^2 + z^2} \quad (4.6)$$

This simple model only describes the most basic kinematics of the mechanism. To truly determine the angular movement of the two motors based on target point coordinates, the above equations need to be modified to take into account of specific design features. For example, the needle tracks are tilted 14 degree to the left of the hoop's center line to allow the probes to go through the remote center of motion, while still maintaining a straight hoop profile. This 14 degree should be subtracted from  $q_1$  to get the actual angular position of the probe on the hoop. Additionally, because the motor is directly mounted to the hoop, the angular rotation of the hoop can directly translate to the motor shaft rotation,  $q_{m1}$ , as

$$q_{m1} = \tan^{-1}\left(\frac{y}{x}\right) - 14 \quad (4.7)$$

To convert  $q_2$  found Equation (4.5) to the motor output angle, more adjustments need to be made. First, the carriage needs to rotate an extra angle to compensate for the needle track shift. Demonstrated by Figure 4-5, if a probe in track 2 (upper dotted line) lines up with the target, then the probe in track 3 (lower dotted line) would end up somewhere to the right side of the target. If track 2 is unavailable and a probe must be inserted into track 3, rotating the probe paths clockwise by an additional compensation angle,  $\delta q_2$ , would allow the probe in track 3 to reach the target (lower solid line).

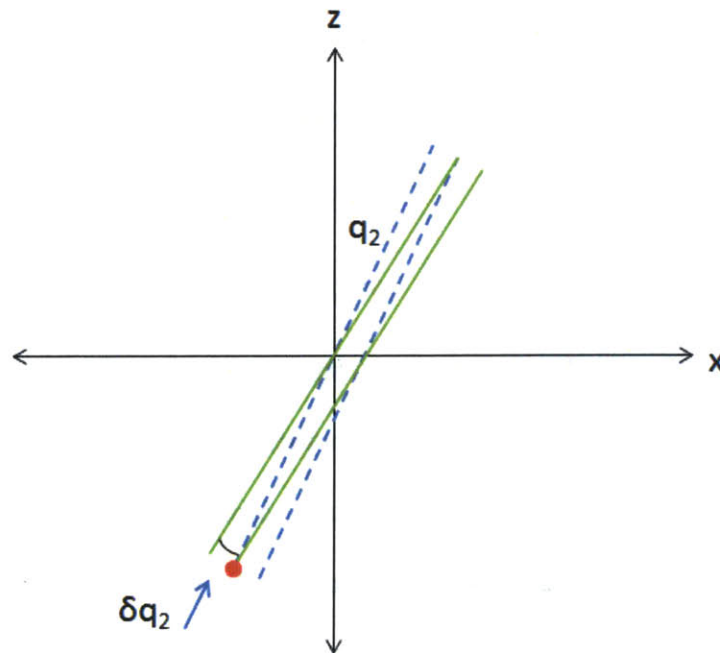


Figure 4-5 Angle compensation for probes placed in other tracks.

Figure 4-6 is a close up view of the probe paths shown in Figure 4-5. Again, the dotted line represents the probe in track 2 when it coincides with the target (red dot). The upper solid line is the probe in track 2 when the carriage rotates by a compensated angle of  $\delta q_2$

so the probe in track 3 (lower solid line) would reach the target. The probe tracks are a distance  $d$  apart, and the target is a distance of  $R$  radially away from the origin. The chord with length  $L$  can be calculated from

$$L = \sqrt{d^2 + (R - s)^2} \quad (4.8)$$

where  $s$  is

$$s = \sqrt{R^2 - d^2} \quad (4.9)$$

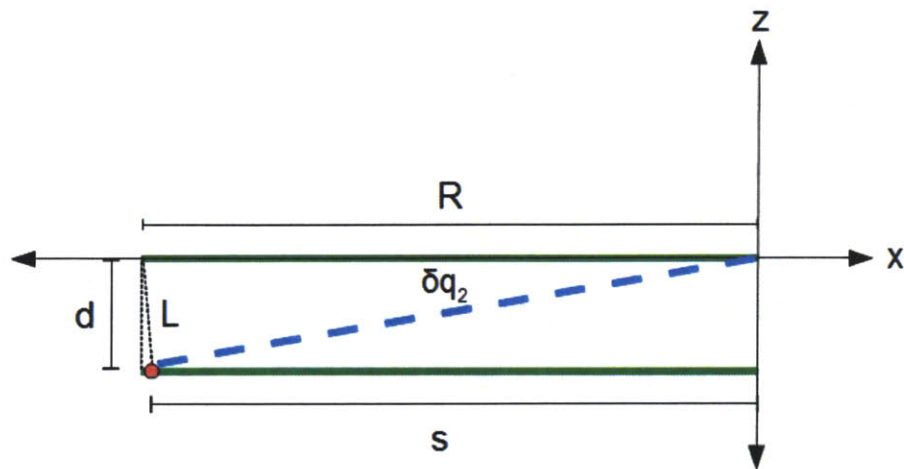


Figure 4-6 Close up of angle compensation. The carriage needs to rotate backward by  $\delta q_2$  in this case to account for track shift.

$L$  can also be calculated with trigonometry

$$L = 2R \sin \frac{\delta q_2}{2} \quad (4.10)$$

Linking the two equations for  $L$ , the compensation angle can be found as

$$\delta q_2 = 2 \sin^{-1} \left[ \frac{\sqrt{2R^2 - 2R(R^2 - d^2)^{\frac{1}{2}}}}{2R} \right] \quad (4.11)$$

For the probe groove to the right (track 3), the carriage needs to rotate further clockwise

$$q_2 = \sin^{-1} \left( \frac{-x}{r} \right) + \delta q_2 \quad (4.12)$$

And for the groove to the left (track 1), the carriage needs to rotate counterclockwise by  $\delta q_2$

$$q_2 = \sin^{-1}\left(\frac{-x}{r}\right) - \delta q_2 \quad (4.13)$$

The ratio between the radius of the driving pulley and the radius of the hoop should be used to convert  $q_2$  to the corresponding motor angle,  $q_{m2}$ .

$$q_{m2} = \left[ \sin^{-1}\left(\frac{-x}{r}\right) + (Track - 2)\delta q_2 \right] \frac{r_{hoop}}{r_{pulley}} \quad (4.14)$$

Furthermore, it was often observed that when the hoop moves, there is a small parasitic motion in the carriage. Illustrated in Figure 4-7, different pieces of the cable were wrapped around the pulley as the hoop rotates, and the carriage, being controlled by the absolute position of the cable, is moved as a result. To account for this motion, the motor driving the carriage needs to rotate a small angle equal to the hoop rotation in the opposite direction, as shown in the equation below.

$$q_{m2} = \left[ \sin^{-1}\left(\frac{-x}{r}\right) + (Track - 2)\delta q_2 - q_{m1} \right] \frac{r_{hoop}}{r_{pulley}} \quad (4.15)$$

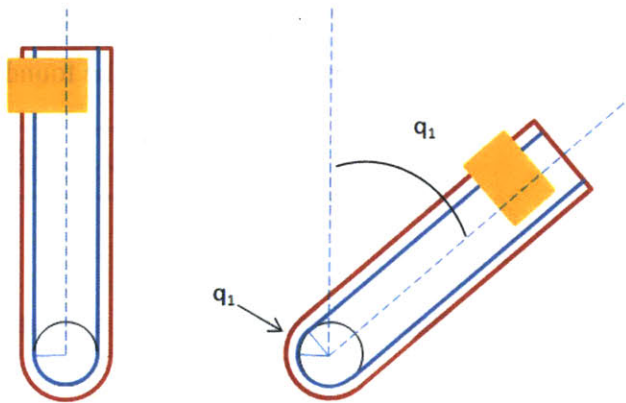


Figure 4-7 Parasitic motion of the carriage during hoop movement is caused by cable passively wrapping on the driving pulley.



A MATLAB script was written to simulate the operation of the device and verify the kinematics equations found above. Operations that are easily performed by the interventionists, such as target selection and device placement, now needed to be generated based on known physical conditions of cryoablation. Assuming the lesion (circle) is positioned as shown in Figure 4-8 in 2D space, the probe insertion site should be at the center of the base. The largest angle of insertion for a probe,  $\beta$ , would occur when the target is at the top edge of the lesion.

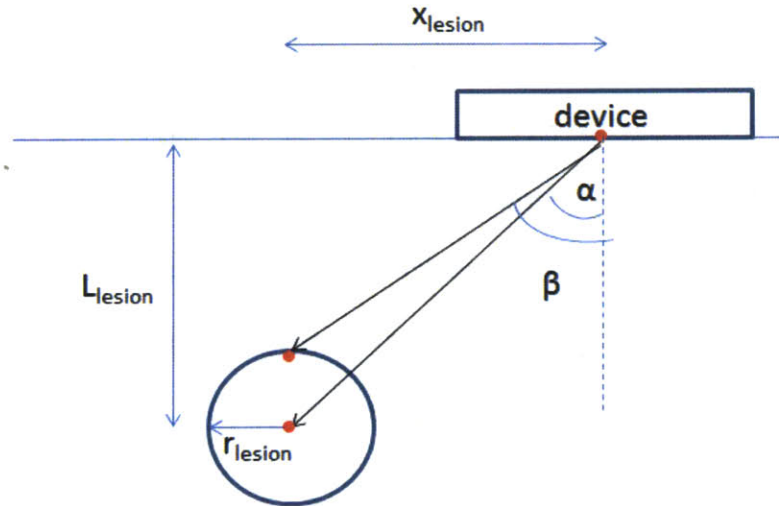


Figure 4-8 The largest probe insertion angle,  $\beta$ , would occur when the target is at the top edge of the lesion.

Since

$$\tan \beta = \frac{x_{lesion}}{L_{lesion} - r_{lesion}} \quad (4.16)$$

and the largest allowable insertion angle is 45 degree, when generating the location of the center of the lesion, the following condition must be satisfied.

$$x_{lesion} \leq L_{lesion} - r_{lesion} \quad (4.17)$$

Based on the lesion size and probe location criteria detailed in section 2.1, in addition to the lesion center location condition found above, three random target points can be generated. It is assumed that device registration and calibration was already completed, thus the targets are generated in device coordinates.

Since the hoop can only move from negative  $q_1$  to positive  $q_1$  to passively release the probes once insertion is completed and avoid colliding with previously placed probes, the order at which the targets are reached must be optimized. A simple sorting function reorders the randomly generated target points from the largest ratio between y and z to the smallest. Then, the adjusted inverse kinematics equations (Equation 4.6, 4.7, and 4.15) are used to calculate the motor angles, with the first target being reached by the probe placed in track 1, second target reached by the probe in track 2, and so forth. The MATLAB script outputs the motor angles and the minimum distances between the probes. The results are used to verify that the device movement is within its designed limit and the probes do not intersect with one another. See Appendix B for the detailed script.

### **4.3 Electrical Wiring and Motor Control**

The Worcester Polytechnic Institute (WPI) Automation and Interventional Medicine Lab developed a MRI compatible controller and software that allows the motor to move during scanning without compromising image quality [31]. This controller makes real time MR image tracking of robot movement possible. Software and hardware were bought from WPI to work specifically for this robot. The system architecture is illustrated in the Figure 4-9. Inside of 3D Slicer, a MR imaging software widely used by doctors to monitor lesion during intervention, registration and calibration modules (currently being developed at BWH, Figure 4-10) converts the image coordinates to the robot coordinates.

The doctor then selects the targets and sends the target points via OpenIGT Link (a module inside of 3D Slicer) to a Java program running in the background. This Java program was developed at WPI and can directly interface with 3D Slicer and the robot controller. In the Java program, the inverse kinematics equations found in section 4.2 would convert the targets to motor angles. The motor driver would then send a signal to move the motor. A PID controller uses the encoder data to perform closed loop position control and sends the robot to the correct position. In the meantime, the encoder data is also converted to target positions with forward kinematics equations in the Java program, and these points are sent back to 3D Slicer via OpenIGT Link. A virtual needle or target point would then move on the screen, helping the user to visualize the current position of the robot.

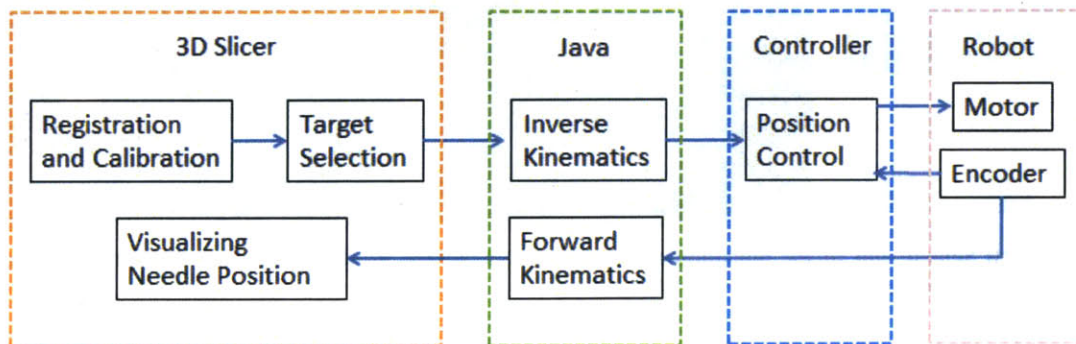


Figure 4-9 Block diagram of system architecture.

Figure 4-11 shows the electrical set up of the MR compatible controller. The black box is the controller, which contains Ethernet converter and fiber optics. It was equipped to run 5 sets of actuator and encoder pairs. This controller is completely shielded and can be put in the scanning room at a minimum distance of 1 m away from the imaging bore. A fiber optics cable connected the controller to the interface box (blue), which should be placed in the control room. This box contains the control computer to run the Java

program, wireless router, fiber optics, and Ethernet converter. Another computer already connected with the MRI would receive image data in 3D Slicer and send the target points to this control computer in the interface box for processing. On the robot side, encoders and motors were plugged into a PCB board, which in turn was connected to the controller. Figure 4-12 is a screen shot of the graphical user interface of the Java program. Appendix C contains the commented Java code.

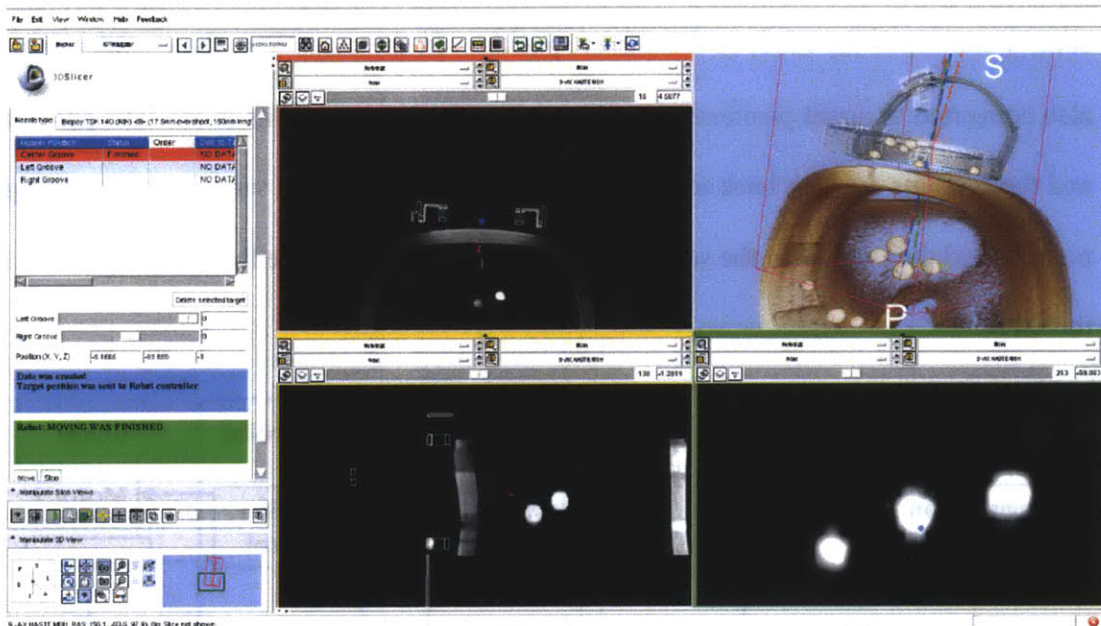


Figure 4-10 Screen shot of the registration and calibration module inside of 3D slicer to work with the robot. It is currently being developed at BWH.

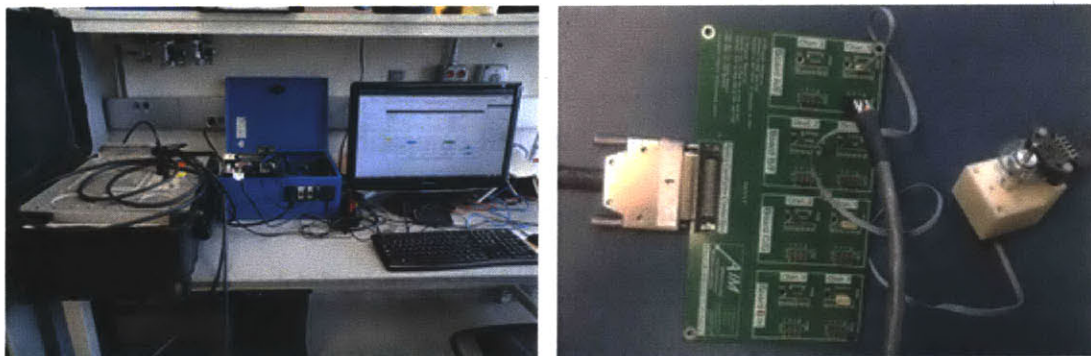


Figure 4-11 MRI Compatible controller set up and electrical connection to motor. Left: The controller (black box) is equipped to run 5 sets of motor/encoder pairs independently. The interface box (blue) can receive image data from another computer running 3D slicer. It then runs the Java software to convert target points into motor angles and sends command to the controller to actuate the motor and read encoder data. Right: the motors and encoders are plugged into a PCB board that interfaces with the controller.

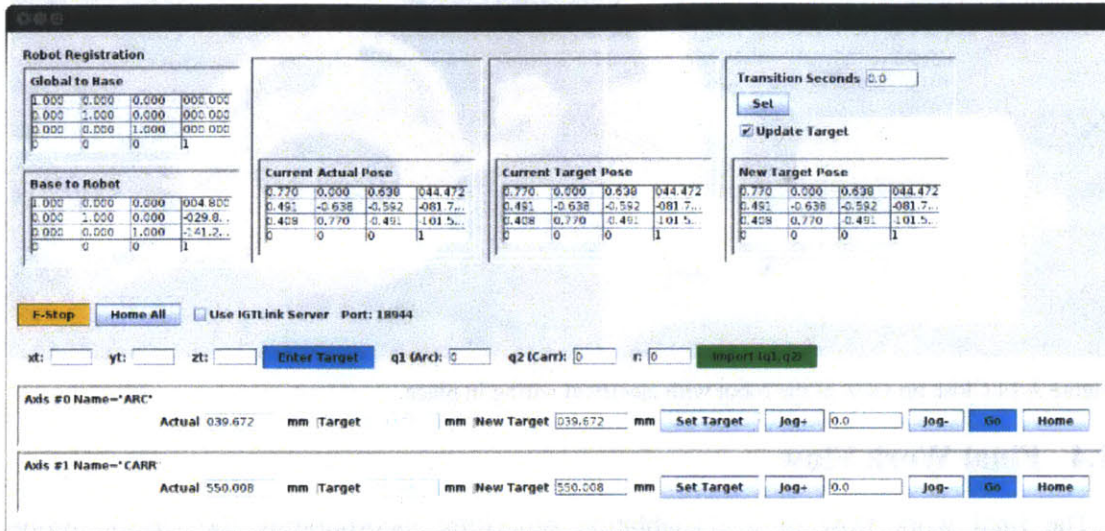
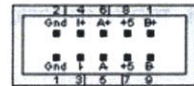


Figure 4-12 Java user interface for converting target points into motor angle and monitoring robot movement.

The cables supplied by the motor manufacturer could be directly plugged into the PCB board. The encoder cable, however, required rewiring. The pins on the PCB board for the encoder and the pin output for the encoder driver module are shown in Figure 4-13.

Figure 4-14 is a close up view of the robot with all the wiring in place.

**PC4-H10 Output Connector**



Pin	Description
1	Ground
2	Connected to pin 1
3	Index-
4	Index+
5	A- channel
6	A+ channel
7	+5VDC power
8	Connected to pin 7
9	B- channel
10	B+ channel

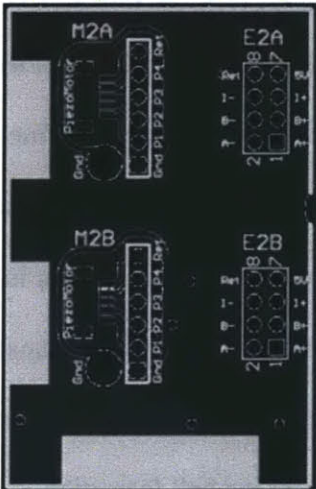


Figure 4-13 The encoder cable needs to be rewired to interface with the PCB board of the controller. Left: Pin output of the encoder differential driver [http://www.usdigital.com]. Right: PCB layout, M for motor input pins, and E for encoder input pins.

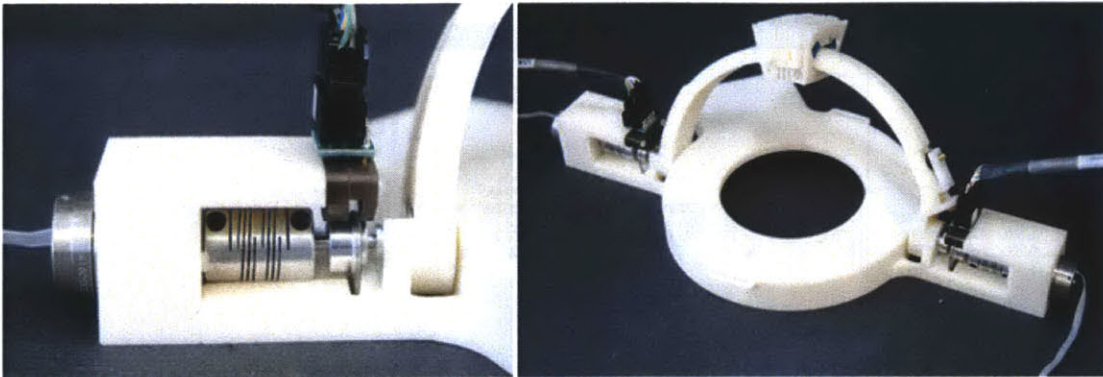


Figure 4-14 Close up view of the robot with electrical wiring in place.

#### **4.4 Final Work Flow**

The final work flow of a cryoablation procedure incorporating the robotic probe guidance system is as follows:

1. Pre-scan patient to determine the general area of interest, approximate needle entry point, and select target points offline.
2. Place fiducial capsule on the approximate needle entry point on patient's skin. Strap MRI loop coil and the robot on patient with Velcro so that the Fiducial capsule is at the center of loop coil.
3. Determine the location of the fiducial capsule in scan, move robot/coil assembly and capsule together to fine tune probe entry point.
4. Make a mark on patient's skin where the capsule is located. Remove capsule.
5. Prepare and drape patient in sterile fashion. Strap patient to MRI bed tightly.
6. Perform initial scan to register and calibrate the device in 3D Slicer.
7. Put local anesthesia at the entry site and check ablation probe in water to ensure proper ice ball formation.
8. Make small incision (5-6 mm) at the center of the device.

9. Start probe guidance module in 3D Slicer. Click on the image to select the previously chosen target points. Send target coordinates to Java software and command robot to move to the first position.
10. Insert first needle (placed in track 1) about 6 cm deep.
11. Scan and double check needle trajectory.
12. Insert needle completely.
13. Release latch on the needle holder and command the robot to move to the next position.
14. Repeat step 10, 11, 12, and 13.
15. Remove device, make any final small adjustment by hand.
16. Start cryoablation.

The final workflow is very similar to current procedure, making it easier for doctors to shift from their old work habits. The needle insertion process may be reduced to 1-3 steps with the guidance of the device. An increase level of confidence in the device's accuracy and precision would further decrease the number of MRI scans required for the procedure.

# Chapter 5

## Device Characterization and Evaluation

Due to time constraints, the final prototype was not tested in an MRI machine. Rather, the accuracy, repeatability, and resolution of the device movement were evaluated with image analysis software. For the test set up, shown in Figure 5-1, the robot was securely fixed to a table and markers in the shape of circular disks were placed on the robot, with black felt taped behind the markers to increase contrast. A digital camera was placed approximately 4 ft away and raised to about the same level as the robot. With the camera being far away but zoomed in optically, most of the light reflecting off the robot would be coming from the same direction, eliminating 3D effects and making movement tracking with a 2D images more accurate. A lamp was put next to the robot to shine more light onto it and improve image quality. A piece of paper marking the trial number was put next to the robot, so the motor command recorded manually can be matched with the picture took and be compared with the actual angle moved during analysis.

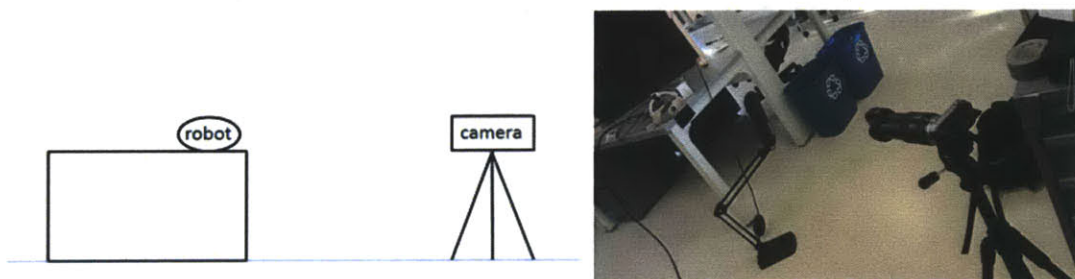


Figure 5-1 2D images taken with digital camera were used to evaluate the performance of the device. Left: Schematic of the test set up. Right: A digital camera is placed approximately 4 ft away and zoomed on the robot for least 3D effects in the image. Markers are put on the robot for tracking purposes.

The hoop and the carriage are each commanded to move at a predetermined angle independently. Each moving component moved back and forth throughout its full range



of motion at 5 and 10 degree intervals. By measuring the actual displacement with the image analysis software and comparing to the command sent to the controller, the accuracy of each component's displacement can be evaluated. The hoop and the carriage were also sent to the same angular position multiple times to measure the repeatability of the mechanism. Finally, incremental movements at 1 degree, 0.5 degree, and 0.1 degree were performed to determine control resolution.

Figure 5-2 shows an example picture obtained from testing. Image J (NIH, USA) is an open-source software that can perform many tasks related to image processing and analysis, such as tracking markers and measuring angles. The line overlaying on the image in Figure 5-2 is a built-in tool of Image J to find the angle. The line is manually drawn between the centroid of the two markers several times. Many photos were zoomed in 10 times or more to accurately locate the marker's centroid. The average from these different measurements is used for final analysis to reduce the human error.

Figure 5-3 and 5-4 shows the accuracy of the hoop and carriage movement.

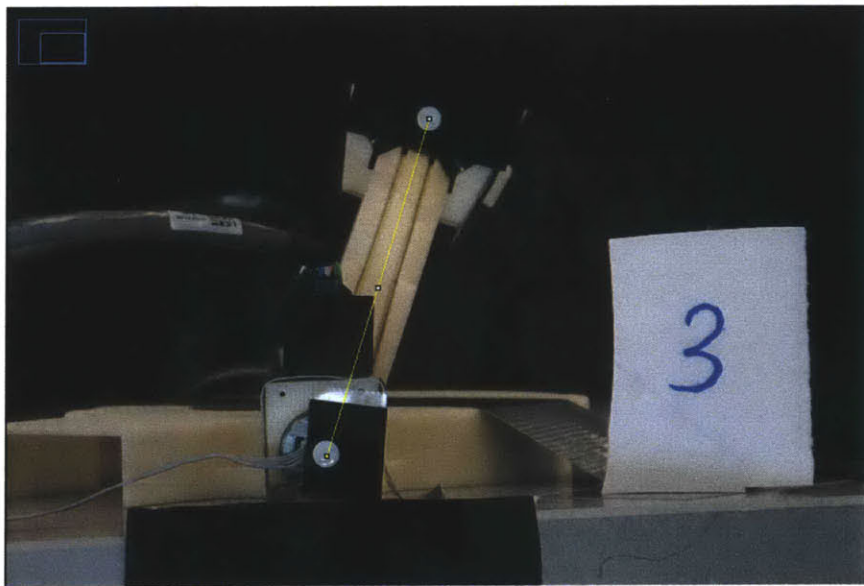


Figure 5-2 Image J was used to analyze the picture took with camera to determine the actual angle of the device has moved.

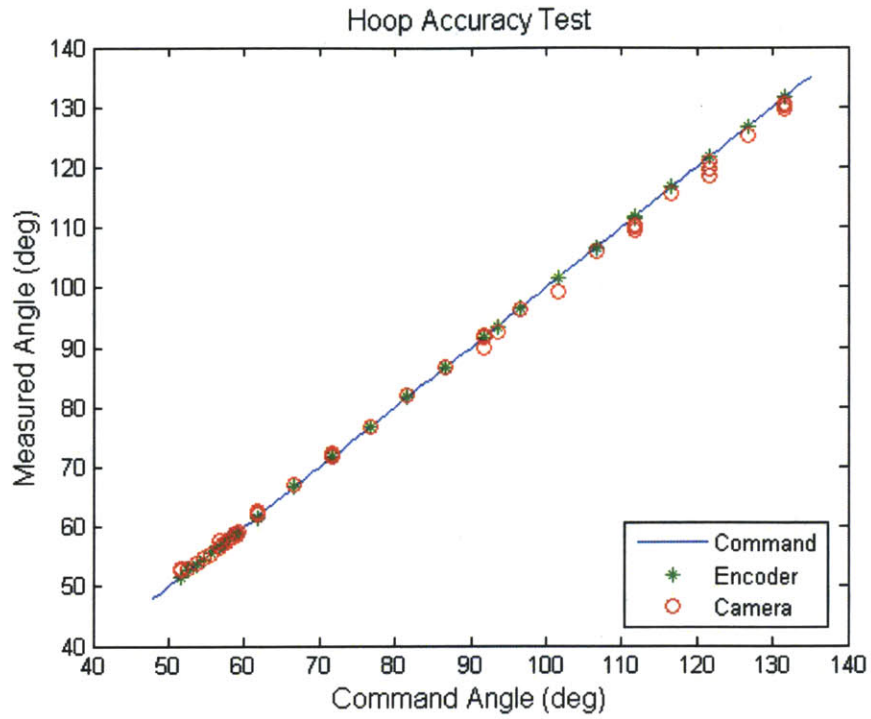


Figure 5-3 Accuracy test result of the hoop movement. Both the encoder and camera data are compared with the command angle.

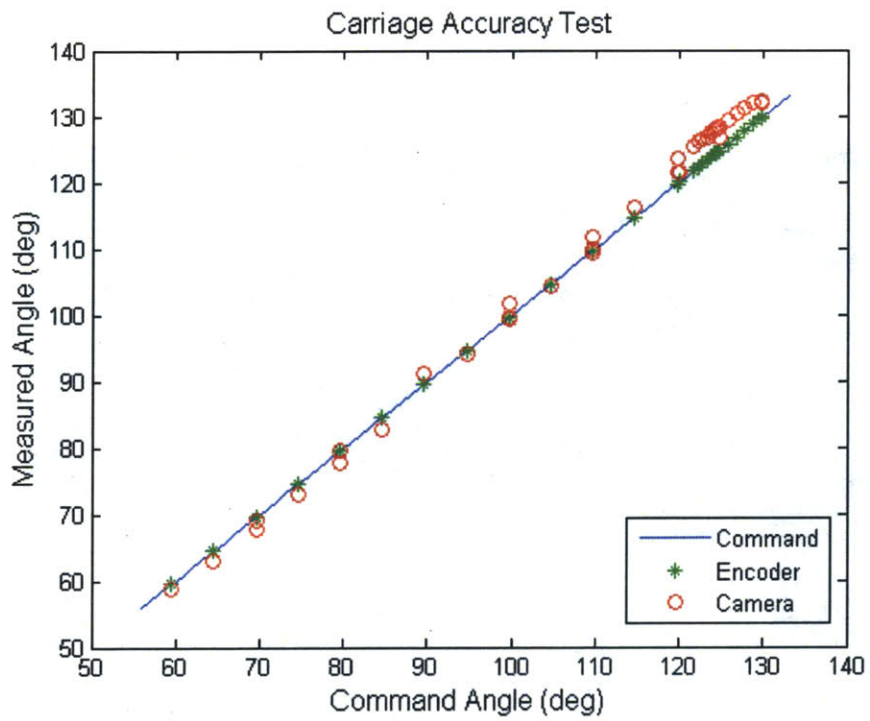


Figure 5-4 Accuracy test result of the carriage movement.

Table 5-1 summarizes the encoder performance. The encoder readings are compared with the command angle sent to the motor to determine its accuracy and repeatability. For the carriage, the encoder data seems to be closer to the command than that of the hoop. This is because the motor driving the carriage has to rotate more times to get the same angular output due to the ratio between the driving pulley and the hoop. Converting carriage angle to motor angle, the average error in the encoder is 0.0276 degree and the standard deviation is about 0.0492 degree, which is close to the hoop encoder error. This small error in the encoder can be eliminated by adjusting the calibration index between the tics on the encoder and the rotation of the motor.

Table 5-1 Encoder accuracy results

Test	Hoop Accuracy (deg)	Carriage Accuracy (deg)
Average Encoder Error	0.0309	0.0023
Standard Deviation, Encoder Error	0.0331	0.0041

The actual error between the measurements obtained from photographs and the command angle is much more than what the encoder claims. Average error and the root-mean square (RMS) errors, which is usually used to evaluate the accuracy of machine system [32], are shown in Table 5-2, where each RMS error is calculated with

$$\epsilon_{rms} = \left( \frac{1}{N} \sum_{i=1}^N \epsilon_i^2 \right)^{\frac{1}{2}} \quad (5.1)$$

Table 5-2 Accuracy test results

Test	Hoop Accuracy (deg)	Carriage Accuracy (deg)
Average Error	0.3348	-1.7049 [0.1754]
RMS Error	1.8105	2.5777 [1.2528]

The max error in the hoop movement is 3.3570 degree and the maximum error in the carriage movement is -3.9102 degree. The carriage appears to have a much larger average and RMS error compared to the hoop. Closer examination of the data showed that most of the error occurred when the carriage is in the vicinity of the tensioning mechanism. When excluding those data, the average and RMS errors for the carriage (shown in square brackets in Table 5-2) are more reasonable and closer to the average errors obtained for the hoop.

Figure 5-5 shows how the hoop and carriage error would affect the probe tip error. The dotted line represents the path of the probe. If the angular movement of either hoop or the carriage is off by  $\epsilon$  and the probe is manually inserted to a depth of  $r$ , then the distance between the probe tip and the intended target (red dot) can be calculated with the chord formula (Equation 5.2). Assuming an average probe reach of 125 mm, Table 5-3 shows the average and RMS tip errors caused by each moving component.

$$\epsilon_{tip} = 2r \sin \frac{\epsilon}{2} \quad (5.2)$$

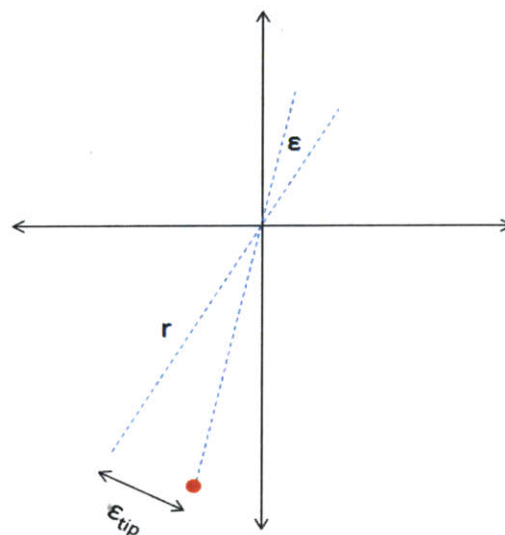


Figure 5-5 A rotation error in the hoop and the carriage would cause a large error in the probe tip.

Table 5-3 Probe tip error

Error Caused by	Hoop (mm)	Carriage (mm)
Average Error	0.7304	-3.7194 [0.3827]
RMS Error	3.9497	5.6232 [2.7331]

Again, the numbers in the square brackets are calculated excluding the data collected near the cable tensioning mechanism. In general, the tip errors are well within the accuracy limit listed in the functional requirements in Chapter 2.

The large error in the carriage movements when the carriage is near the tensioning mechanism could have been a result of the specific design of the mechanism. The tensioning pulley was designed to be on the same level as the cable groove on the hoop. Most of the time, the cable would come to the tensioning pulley from a direction tangent to the hoop, perpendicular to the rotational axle of the pulley. Since the bottom of the carriage is offset from the surface of the hoop, the cable coming out of it would also be lifted off the groove. The tension in the cable would pull the cable down into the groove and not affect the performance of the carriage in general. However, as the carriage gets closer to the tensioning mechanism, the lifted piece of cable also gets closer to the pulley. It thus becomes harder for the cable to arrive at the tensioning pulley in that tangent direction. When the carriage is near the extreme end of the hoop, the cable can no longer be pulled into the groove. The tensioning pulley therefore experiences an upward force from the lifted cable directly, causing un-modeled behavior in the cable driving system. Such an error can be reduced when the tensioning mechanism is placed further away on the hoop from the extreme carriage angle (45 degree). Since the current hoop design is

already optimized for the furthest possible tensioning mechanism placement, a larger hoop would be necessary to help reduce the above mentioned error.

The PID coefficients are set to very low values to allow for slow and steady movement. However, they are not currently optimized to the performance of the device. Better tuned controller coefficients could improve the overall error. Other solutions may include more finely controller cable tensioning and better attachment method for securing the hoop and driving pulley to the motors.

Figure 5-6 and Figure 5-7 plots the repeatability of the hoop and carriage respectively. The average for each angle is also shown in the plot in red.

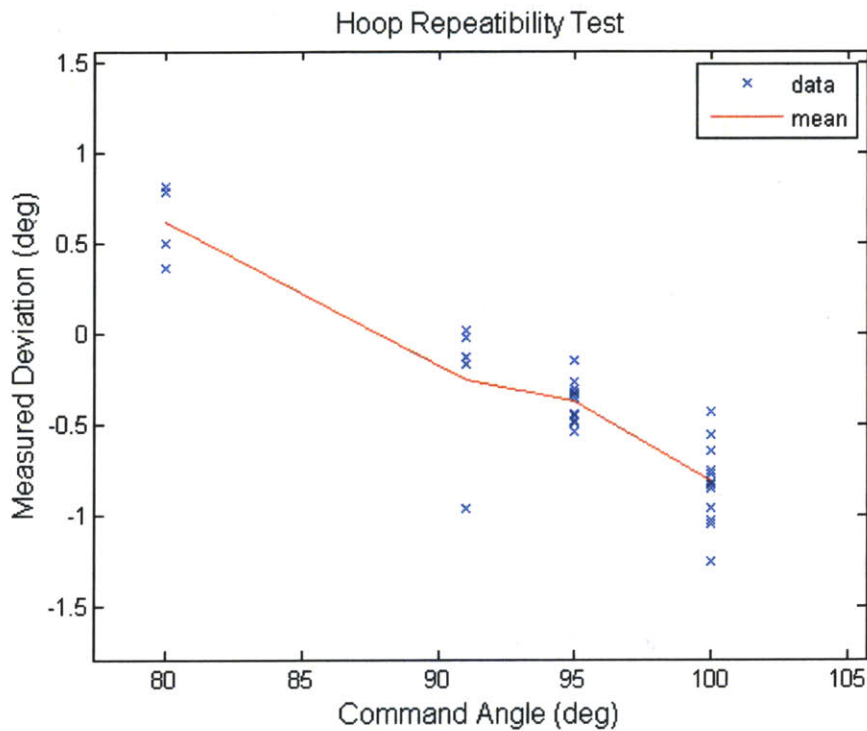


Figure 5-6 Hoop movement repeatability test.

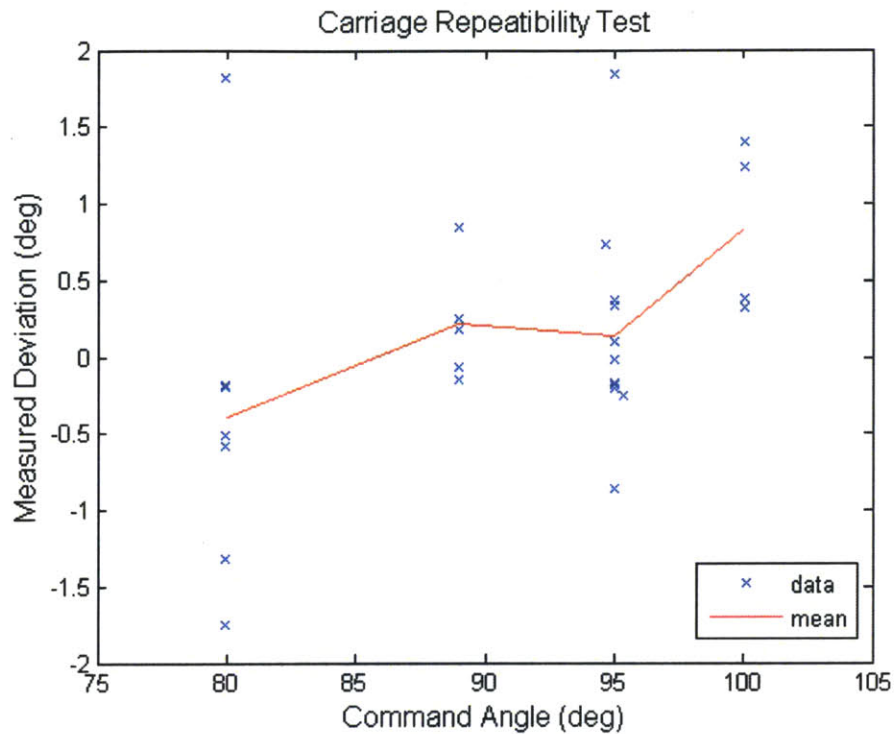


Figure 5-7 Carriage movement repeatability test.

Defining the upright angle as absolute 90 degree, the hoop is moved to 80 degree (14 trails), 91 degree (5 trails), 95 degree (14 trails) and 100 degree (5 trails). For each angle, 6 to 15 trials were conducted to measure repeatability. Table 5-4 shows the average and standard deviation of the errors obtained from the hoop repeatability tests.

Table 5-4 Hoop repeatability test results

Tested at	80 deg	91 deg	95 deg	100 deg
Average Actual Error	0.6148	-0.25	-0.3728	-0.80815
Standard Deviation	0.2210	0.4049	0.1	0.2198

The hoop movement tends to be more repeatable when it is closer to being upright. Perhaps there is less gravity effect in those positions, reducing random error in the

system. The photographs taken at those sections were also more focused and exhibited less 3D effects. With more defined edges, it was also easier to make more repeatable measurements.

The carriage was measured at 80 degree (7 trails), 89 degree (5 trails), 95 degree (11 trails) and 100 (5 trails) degree. Table 5-5 shows the results of the carriage repeatability tests. Again, more repeatable measurements were obtained when the carriage is near 90 deg.

Table 5-5 Carriage repeatability test results

Tested at	80 deg	89 deg	95 deg	100 deg
Average Actual Error	-0.3875	0.2145	0.1319	0.8303
Standard Deviation	1.049	0.3488	0.635	0.485

For the resolution test, each moving component was moved a 1 degree, 0.5 degree, and 0.1 degree interval. Table 5-6 shows the hoop resolution test results. For 0.1 degree movement interval, the standard deviation is about the same as the step itself. This means either the hoop cannot be actuated to move in such fine steps or the camera system used to measure the movement did not have enough resolution to capture the movement. Similar numbers are measured for the carriage movements, with a larger standard deviation. Table 5-7 shows the results of the carriage resolution test. At 0.1 degree interval, the standard deviation is larger than the step, which is likely caused by the imprecise measurement with the photographs or the limitations of the camera.



Table 5-6 Hoop movement resolution test result

Tested at Interval	1 deg	0.5 deg	0.1 deg
Average Actual Movement	0.9277	0.4728	0.954
Standard Deviation	0.0893	0.0965	0.085

Table 5-7 Carriage movement resolution test result

Tested at Interval	1 deg	0.5 deg	0.1 deg
Average Actual Movement	0.948	0.4925	0.067
Standard Deviation	0.1885	0.1292	0.1394.

In summary, the probe positioning robot is able to achieve sub-degree accuracy (less than 1 mm displacement at the probe tip) in most cases and can follow command at incremental steps of at least 0.5 degree resolutions. When the movement of either the hoop or the carriage is near 90 degree (vertical), the measurements are quite repeatable. Further calibrating the PID controller and the encoder, as well as changing the location of the cable tensioning mechanism, may improve the accuracy of the device. As the incremental command angle gets smaller, the limitations of the still camera in capturing physical changes and the human error in making the line in Image J may have resulted in a more conservative resolution measurement than what the device is actually capable of. Further testing with more accurate measuring systems may be needed to further characterize this device.

# Chapter 6

## Conclusions and Future Work

The purpose of this thesis is to document the design and development of a compact MR compatible robot to guide the trajectories of multiple cryoablation probes. A two DOF spherical mechanism that mounts to the Siemens 110 mm loop coil was constructed out of MRI compatible plastic. The mechanism consists of a rotating hoop and a carriage, which pivots the interventional probes about a remote center of motion located 15 mm above the skin. The carriage, constrained by a custom designed low friction roller bearing and pulled by strong and low stretch cables, travels on the hoop and holds up to 3 probes. A thumbscrew fastened latch on the carriage allows a probe to be engaged or disengaged in one of the three needle tracks, which guides the probe along a specific trajectory. Small MRI compatible piezoelectric motors are used to actuate the movement of the hoop and the cable system. The form factor of the device was greatly influenced by the current procedure work-flow and the ease of sterilization.

Bench level evaluation demonstrated that each component of the device works according to the design specifications. Initial characterization of the device's overall performance was conducted by analyzing still images taken before and after commanded movement. The results show that the device can achieve sub-degree accuracy (less than 1 mm probe tip displacement), sub-degree repeatability near vertical position, and an incremental step resolution of at least 0.5 degree.

This prototype robot is a proof of concept that demonstrates the feasibility of positioning multiple probes for MRI guided percutaneous intervention. Such a device offers a practical and cost-effective approach in improving the placement of multiple

ablation probes to match a treatment plan determined a priori. By mounting it on an MRI coil, the device becomes part of the procedure work-flow. The two actuators could be integrated into a reusable module that snaps into a single-use base to assist with maintaining a sterile field.

Although many components of the device have been proved to function inside of MRI, verifying the MR compatibility of the whole mechanism is still needed. A high speed motion capturing system that can track the movement of the device in real time can help further test the accuracy of probe placement and calibrate the mechanism for optimal performance. A user-interface that is based on 3D Slicer is under development and will enable semi-automatic registration as well as point and click targeting. Experiments in a phantom model in an MRI machine are planned and will yield additional useful information for improving the design. Other possibilities include an automated insertion mechanism and steerable ablation probes, which could further simplify the probe positioning problem and reduce targeting error caused by probe bending in tissue. Ultimately, this robot is envisioned to perform automatic probe placement and ablation inside of any medical imaging machine, enabling faster, safer, and cheaper interventional treatments.

## References

1. Zhang Q, Chung YC, Lewin JS, Duerk JL, A method for simultaneous RF ablation and MRI. *Journal of Magnetic Resonance Imaging*, 1998;8:110 -114
2. Rukstalis D and Katz AE, A Handbook of Urologic Cryoablation, Informa Healthcare, Feb 13, 2007.
3. Doll N, et al., Intraoperative Cryoablation with a new Argon Probe, *Ann Thorac Surg* 2004;77:1460–2.
4. Gage AA. History of cryosurgery. *Semin Surg Oncol* 1998; 14:99 -109
5. Lindsey H, Percutaneous Cryoablation Effective for Select Patients with Kidney Tumors, *Oncology Times*, June 2007 - Volume 29 - Issue 11 - p 35-36
6. Georgiades CS, Hong K., Bizzell .C, Geschwind J.-F., Rodriguez R.: Safety and Efficacy of CT Guided Percutaneous Cryoablation for Renal Cell Carcinoma, *JVIR* 2008; 9: 1302-1310.
7. Opel A, Murray S, Kamath N, Dhinoja M, Abrams D, Sporton S, Schilling R, Earley M. Cryoablation versus radiofrequency ablation for treatment of atrioventricular nodal reentrant tachycardia: cryoablation with 6-mm-tip catheters is still less effective than radiofrequency ablation. *Heart Rhythm*. 2010;7:340–343.
8. Deisenhofer I, et al., Cryoablation versus radiofrequency energy for the ablation of atrioventricular nodal reentrant tachycardia (the CYRANO Study): results from a large multicenter prospective randomized trial. *Circulation*, 2010 Nov 30;122(22):2239-45. Epub 2010 Nov 15, American Heart Association.
9. Rasmus M, Dziergwa S, Haas T, Madoerin P, Huegli R, Bilecen D, and Jacob AL, “Preliminary clinical results with the MRI-compatible guiding system INNOMOTION,” *Int J CARS*, 2, pp. S138–S145, 2007.
10. Taillant N, Avila-Vilchis JC, Allegrini IB, and Cinquin P, “CT and MR compatible light puncture robot: architectural design and first experiments,” *Proceedings of 2004 International Society and Conference Series on Medical Image Computing and Computer-Assisted Intervention*, Vol. 2, pp. 145–154.
11. Hata N., et al. Needle Guiding Robot for MR-guided Microwave Thermotherapy of Liver Tumor using Motorized Remote-Center-of-Motion Constraint. in *Robotics and Automation, 2005. ICRA 2005. Proceedings of the 2005 IEEE International Conference on. 2005.*
12. Walsh C, Hanumara N, Slocum A, Shepard J, and Gupta R, “A patient-mounted telerobotic tool for CT-guided percutaneous interventions,” *ASME Journal of Medical Devices*, 2(1): 2008.
13. Muntener M, Patriciu A, Petrisor D, Mazilu D, Bagga H, Kavoussi L, Cleary K, and Stoianovici D, “Magnetic Resonance Imaging compatible robotic system for fully automated brachytherapy seed placement,” *Urology*, 68(6), pp. 1313–1317, 2006.
14. Su H, Camilo A, Cole GA, Hata N, Tempny CM, and Fischer GS, “High-field MRI-compatible needle placement robot for prostate interventions,” *Stud Health Technol Inform*. 2011;163:623-9. PMID: 21335868.

15. Larson BT, et al., Design of an MRI-Compatible Robotic Stereotactic Device for Minimally Invasive Interventions in the Breast. *Journal of Biomechanical Engineering*, 2004. 126(4): p. 458-465.
16. Chen X, "Instrument guide for MRI-guided percutaneous interventions," Bachelor Thesis, Massachusetts Institute of Technology, 2010.
17. Gillespie TD, *Fundamental of Vehicle Dynamics*, SAE International, Edition 1, February 1992, p117
18. Gafford, J., Schneider, J., Tao, G., Wiltsie, N., Wong, K.W., Gupta, R., Kumar, A., A Mobile Optical Tomography System to Integrate with Computed Tomography Scanners for Image Co-registration, MIT 2.75 Final Paper, 2010 (unpublished).
19. Slocum A. FUNdaMENTALS of Design. In: <http://web.mit.edu/2.75/resources/FUNdaMENTALS.html>, 2008.
20. Tanner D, Fitzgerald JA, and Phillips BR, "The Kevlar story—an advanced materials case study," *Angewandte Chemie International Edition in English*, 28: 649–654. 1989,doi: 10.1002/anie.198906491.
21. Stein H L, Ultrahigh molecular weight polyethylenes (uhmwpe). *Engineered Materials Handbook*, 1998 (2), 167–171.
22. Shigley JE, Mischke CR. *Mechanical Engineering Design*. 6th Ed, McGraw-Hill, pp. 470-473, 2001.
23. Blake JC, Kurtz HJ. The Uncertainties of Measuring Fastener Preload. *Machine Design*, vol. 37, pp. 128-131, 1965
24. Hemmati Vand E, Oskouei RH, Chakherlou TN, An Experimental Method for Measuring Clamping Force in Bolted Connections and Effect of Bolt Threads Lubrication on its Value, *World Academy of Science, Engineering and Technology*, vol. 46, pp. 457- 460, 2008
25. Nanomotion HR8 ultrasonic motor user manual. In: <http://www.nanomotion.com/data/docs/HR8.pdf>
26. Fischer GS, Krieger A, Iordachita I, Csoma C, Whitcomb L, and Fichtinger G, MRI Compatibility of Robot Actuation Techniques – A Comparative Study, MICCAI 2008, Part II, LNCS 5242, pp. 509–517, 2008.
27. Verdirame J, *Characterization of a Hydraulic Actuator for a Functional Magnetic Resonance Imaging Robot*. BSME Thesis, Massachusetts Institute of Technology, June 2000.
28. Piezomotor Piezo LEGS Rotary 50 mNm motor user manual. In: [http://www.piezomotor.se/documents/150062-00\\_LR5012.pdf](http://www.piezomotor.se/documents/150062-00_LR5012.pdf)
29. EM1 Transmissive Optical Encoder Module User Manual. In: [http://www.usdigital.com/assets/general/149\\_em1\\_datasheet\\_0.pdf](http://www.usdigital.com/assets/general/149_em1_datasheet_0.pdf)
30. Sears P, Dupont P. A Steerable Needle Technology Using Curved Concentric Tubes. *Intelligent Robots and Systems*, 2006 IEEE/RSJ International Conference on, 2006; 2850-2856.
31. Cole G, Harrington K, Su H, Camilo A, Pilitsis J, Fischer GS, Closed-Loop Actuated Surgical System Utilizing Real-Time In-Situ MRI Guidance, 12th International Symposium on Experimental Robotics - ISER 2010, December 2010
32. Slocum, A.H., *Precision Machine Design*, Society of Manufacturing; illustrated edition, January 1, 1992.

33. Udroi, R, Nedelcu, A. Optimization of Additive Manufacturing Processes Focusing on 3D Printing, Rapid Prototyping Technology - Principles and Functional Requirements. InTech, September 2011.

# Appendix A

One method to achieve low frictional constrained movement is through a sliding bearing. Modeling the device as shown in Figure 3-1, the angle between the center of the carriage and the center of the hoop is defined as  $\theta$ . The friction between the sliding bearing and the hoop is

$$F_{fr} = \mu N = 0.07 m_{bearing} g \cos \theta \quad (A.1)$$

With a 300 g mass limit and a coefficient of friction about 0.07 (Teflon), the bearing would experience maximum frictional force, approximately 0.2 N, when  $\theta=0$  or when the bearing is vertical.

The total force required to move the bearing can be calculated from

$$\sum F = F_{motor} - F_{fr} = m_{bearing} a \quad (A.2)$$

Based on the bearing functional requirements and the maximum frictional force calculated, the maximum motor force required is approximately 0.5 N, which is much less than the specified maximum limit of 3 N.

For a bench level experiment, the hoop and the four walls of the bearing are 3D printed with matte surface finish (Figure A-1). Although the matte option results in a rougher surface finish, the supporting material that covers the part surface helps protecting it from excessive UV radiation during the printing process, improving its overall accuracy [32]. The smooth contact surface was achieved by attaching a layer of Teflon shim (0.015" thick) to the inner walls of the bearing. The walls are connected to one another with plastic M2 bolts. Slots in the front and back walls, instead of plain through holes, are

used to adjust the distance between the top and bottom walls, enabling some preload in the bearing.



Figure A-1 Plane contact sliding bearing bench level test.

When moving by hand, the bearing slides quite smoothly, as expected from a contact surface made of low friction plastic. The smoothness of the motion is only limited by the matte surface finish of the 3D printed hoop and the rigidity of the tape used to secure the Teflon shim. Although the bolt-in-slot arrangement in the bearing walls allowed for preloading the bearing in one direction (up and down), in addition to the small amount of preload provided by the Teflon shim all around, the overall bearing stiffness was still less than ideal as the bearing can be wiggled by hand. Simple adjustments to the bolting arrangement may eliminate this problem (Figure A-2). Plastic with low frictional resistance, such as Delrin or Teflon, can also be used to mill out the whole bearing, improving the part precision and eliminating the need for additional shim.



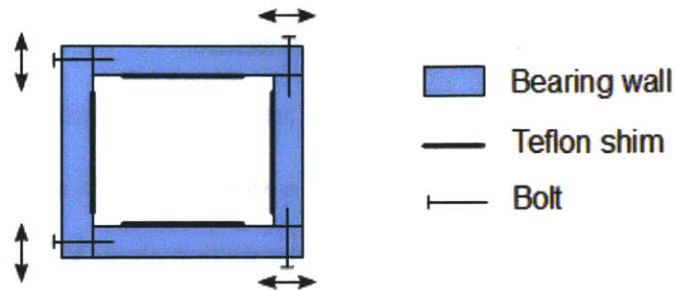


Figure A-2 Redesign of the plane contact sliding bearing to allow for more adjustments in the bearing wall position and preload the bearing to desired stiffness.

One of the disadvantages of a sliding bearing is its requirement of contacting all four sides of the hoop, introducing unnecessary friction given non-perfect kinematic alignment. The attachment of Teflon shim cannot be precisely controlled. Adding the bolt misalignment and accumulated error from 3D printed parts, this design may result in a lot of probe positioning error. Machining the bearing out of low friction plastic could eliminate such problem; however it would cost more time and money to produce.

Additionally, with the bolt-in-slot design shown in Figure A-2, a compromise must be made between the achievable friction and the stiffness of the bearing. The more preload applied to the bearing, the harder it is to slide. Granted that sacrificing friction for stiffness is a problem for all types of bearings, the sliding bearing would still suffer more losses in this case due to its solid plane contact.

A multiple point contact sliding bearing is a more flexible alternative that can help solve some of the problems stated above. Instead of having the whole bearing wall touching the sides of the hoop, stationary balls or hemispheres on the bearing wall can be used to contact the surface of the hoop. Nylon balls ( $\mu=0.34$ ) are used to embed in the bearing walls instead. With a higher coefficient of friction, the maximum resistance is

calculated as 1 N and the maximum required motor force is 1.3 N. These forces are still sufficiently small to guarantee a low frictional interface.

For an initial design, five 1/8" Nylon balls are used to constrain the five DOFs, with each ball touching the grooves on the hoop at a single point. As shown in Figure A-3, if direction X is the desired direction of motion, the motion along Y is constrained by ball 1 and 2, and motion along Z is constrained by ball 3, 4, and 5. The rotations around X and Y are constrained by balls 3, 4, and 5, and the rotation around Z is constrained by balls 1 and 2.

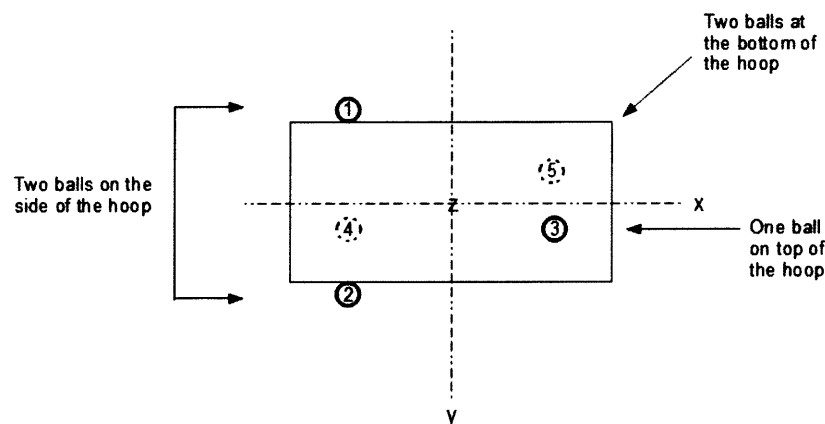


Figure A-3 Ball placement for point contact sliding bearing.

For bench level testing, a prototype carriage and hoop were 3D printed. The walls of the bearing are offset from the surface of the hoop in all four directions, avoiding sliding friction caused by direct contact between the bearing walls and the hoop. The amount of offset is adjusted manually by tightening or loosening the plastic M2 bolts connecting the walls. To secure the balls in the bearing, small holes (2.4 mm in diameter) are put in each

wall where the balls are positioned. Figure A-4 is a cross section view of the bearing mounted on the hoop.

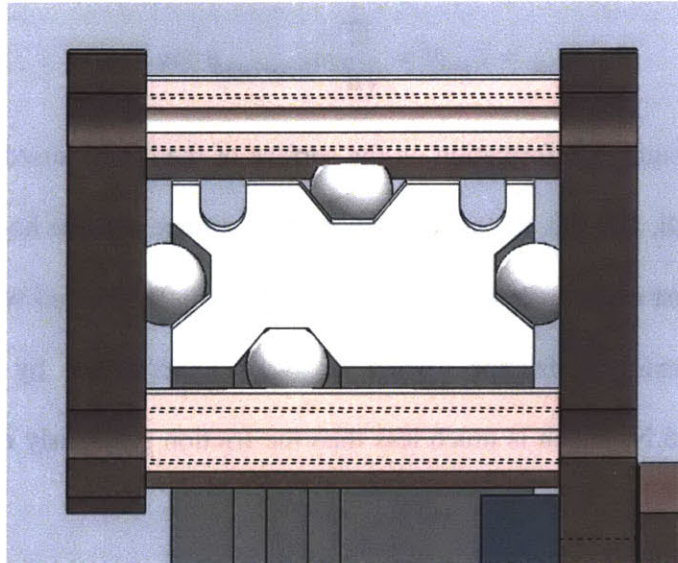


Figure A-4 Cross sectional view of the point contact sliding bearing. Nylon balls are imbedded into the bearing walls to provide the point contact needed.

When moving the prototype bearing by hand, more resistance was experienced compared to plane contact sliding bearing. In this case, without having a whole plane to average out the errors, every imperfection on the surface of the hoop can affect the bearing movement, reducing the smoothness of the travel and introducing errors. Residual supporting materials left in the grooves were difficult to clean, leaving a rougher surface finish than expected. Due to the hoop geometry and the physical nature of 3D printing process, the grooves would always become over hanging features and required supporting material. Hence, the grooves would always end up with a rough matte surface finish despite printing option selected.

The roughness of the groove surface cannot be eliminated. Other manufacturing processes may be used but would cost more time and money to achieve similar part

precision. Since rolling elements generally experience lower friction than sliding elements at a cheaper cost, a linear ball bearing design was examined next. If the ball rolls, then the friction experienced by the bearing is

$$F_{roll} = C_{rr}N = \sqrt{\frac{z}{d}} m_{bearing} g \cos \theta \quad (A.3)$$

where  $z$  is the amount of deformation on the surface of the hoop caused by the ball,  $d$  is diameter of the ball, and  $\theta$  is the angle between the carriage and the hoop (as defined in Figure 3-1). By first order analysis, over estimating  $z$  as 0.01 mm and with a ball of 1/8" diameter, the maximum friction (when  $\theta = 0$ ) experienced by the bearing is approximately 0.16 N, which is much less than the friction previously calculated for the sliding bearing.

A kinematically constrained ball bearing was designed based on schematics shown in Figure A-5. Five points of contact on each part completely constrain the five DOFs of the bearing on the hoop. The balls, resting on the two V grooves, one on the hoop and one on the top half of the bearing top, make four-point contact, which can help support axial load and moment. With similar coordinates as specified in Figure A-4, balls 1 and 2 constrain the motion in Y and rotation around Z. All three balls constrain the motion in Z and rotation around Y and Z.

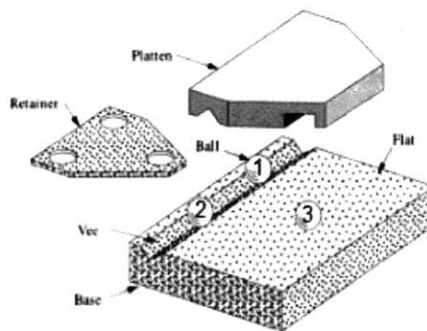


Figure A-5 A non-recirculating ball bearing utilizes Vee and flat grooves to constrain its motion [32].

The above design is picked for its simplicity and compact size. The balls are separated by the retainer, keeping them from rubbing against one another. The retainer would travel freely with respect to the base and the bearing wall. However, for a non-recirculating bearing, the rolling elements and the retainer would only move half the travel distance of the carriage (Figure A-6), which limits the range and size of the bearing. Putting balls and retainer that spans half the length of the arc would defeat the purposes of designing a compact and simple bearing.

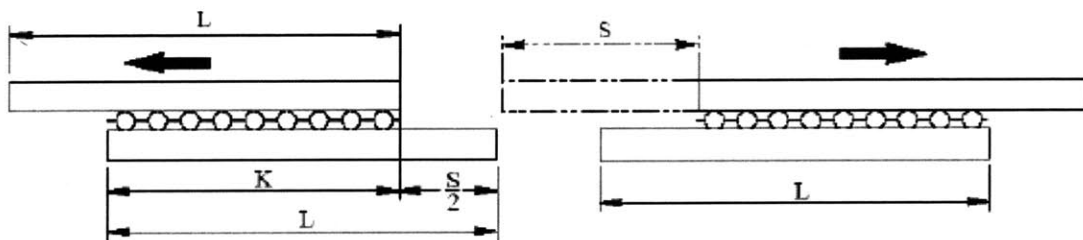


Figure A-5 In a non-recirculating ball bearing, the balls and the retainer would move half the distance of the total travel [32].

Would a smaller carriage work just as well if the retainer were to travel along with the carriage instead of being independent? The balls' movements are expected to be constrained somewhat since they cannot move as freely, but it may just be sufficient for this particular application. A bearing prototype was machined out of Delrin and one of similar dimensions was 3D printed (Figure A-7). To preload the bearing, two 6-32 bolts and compressive springs are used to connect the two sides of the bearing together. The plate on the side simulates the needle holder and its effect on the bearing stiffness is negligible. 1/16" aluminum sheet metal, taped onto the two sides of the bearing, is used to retain the three 1/4" glass balls.

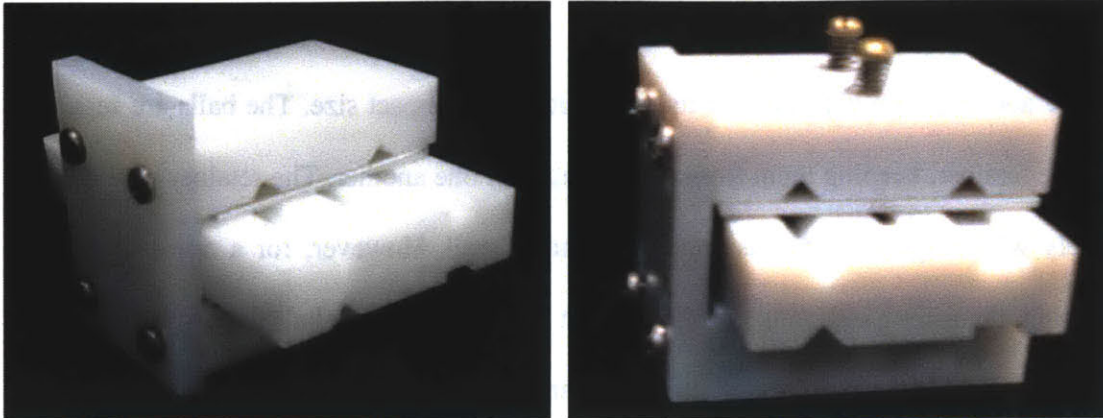


Figure A-7 Prototype non-recirculating bearings, preloaded with bolts and springs. A piece of aluminum sheet metal serves as retainer for the glass balls. Left: Bearing machined out of Delrin. Right: 3D printed bearing of similar dimension.

After preloading, the bearings can be moved easily by hand with little resistance. As expected, some sliding was observed based on the motion of the ink point marked on the balls since the retainer now does not allow for complete free rolling movement of the balls due to its attachment to the bearing sides. When twisted by hand, the Delrin model exhibited sufficient stiffness in the constrained directions.

As shown in Figure A-8, the force required to move the bearing was measured with a Logger Pro force sensor (Vernier Software and Technology, Beaverton, OR). A force vs. time plot was generated (Figure A-9). The maximum force was measured to be 4.43 N, with a typical force required for movement (averaging the force measured from the beginning of the bearing motion to the end of the bearing motion) of 3.64 N.

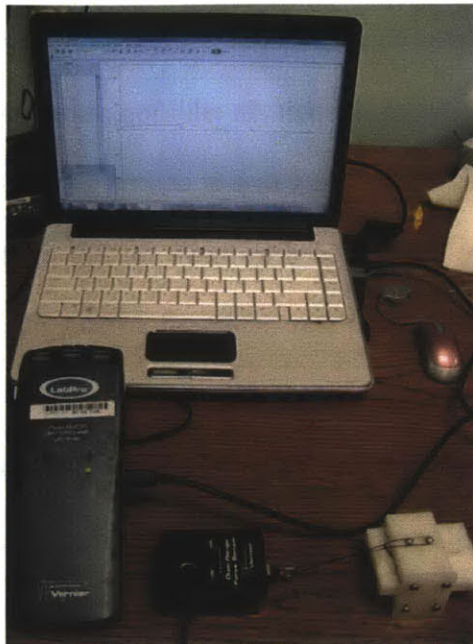


Figure A-8 Bench level set up to test the force required to move the Delrin non-recirculating ball bearing.

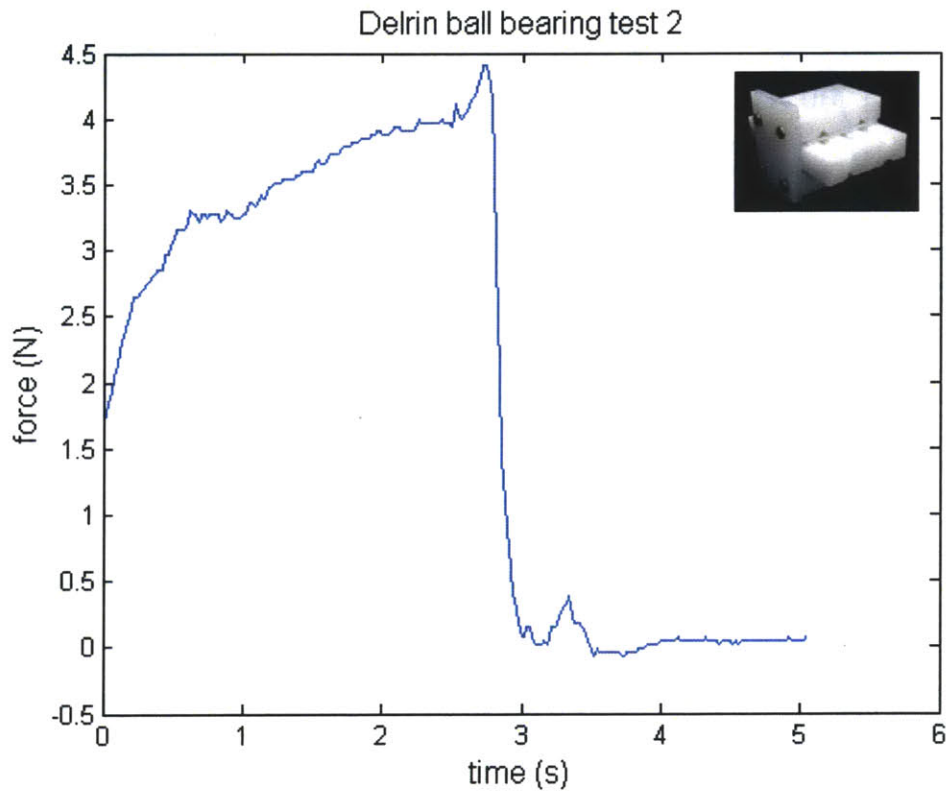


Figure A-9 Example force measurement of the Delrin non-recirculating ball bearing. Average force required to move the bearing is 3.64 N, with a maximum measurement of 4.43 N.

The motion of the 3D printed bearing model felt less smooth than the Delrin model due to the surface finish limitation of the part. In addition, more preload (i.e. turning of the bolt) was needed to maintain a stiffness that is comparable to the Delrin. With similar bench level test set up, the force needed to move the 3D printed model was measured (Figure A-10). The maximum force was measured around 3.1 N and the average force was about 2.65 N. These bench level measurements are very close to the force limit defined in the functional requirements. This model proved that at least on a large level, a rolling ball bearing can be 3D printed and acquire movement with low frictional force.

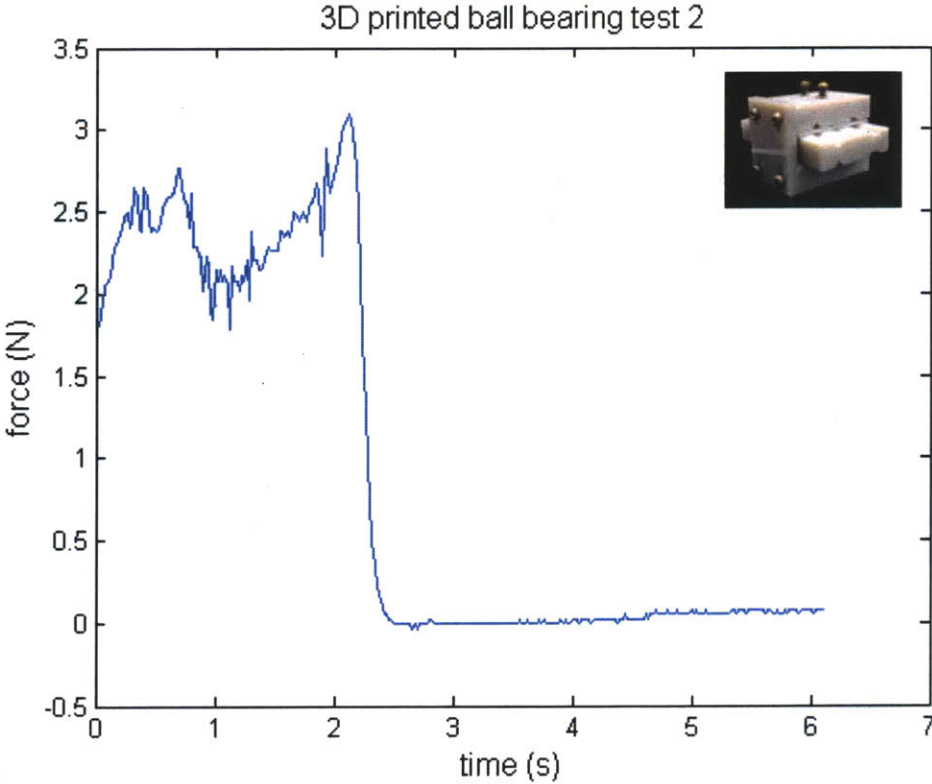


Figure A-10 Example force measurement of the 3D printed non-recirculating ball bearing. Average force required to move the bearing is 2.65 N, with a maximum measurement of 3.1 N.



A real scale non-recirculating rolling ball bearing was 3D printed to examine its performance on curved surfaces. 1/8" diameter glass balls are used in the bearing as the rolling element. The retainer, made of Teflon shim, was taped on the inner walls of the bearing. Because most of the components are quite small, assembling the bearing required careful and meticulous labor. This prototype was tested on an Advanced Mechanical Testing System (Instron, Norwood, MA) to obtain more accurate force measurements (Figure A-11). A brace made of 1/8" aluminum sheet metal is used to limit the cantilever deflection of the curved hoop. Dyneema bow string (low wax) is used to simulate the cable drive system which actuates the movement of the bearing.

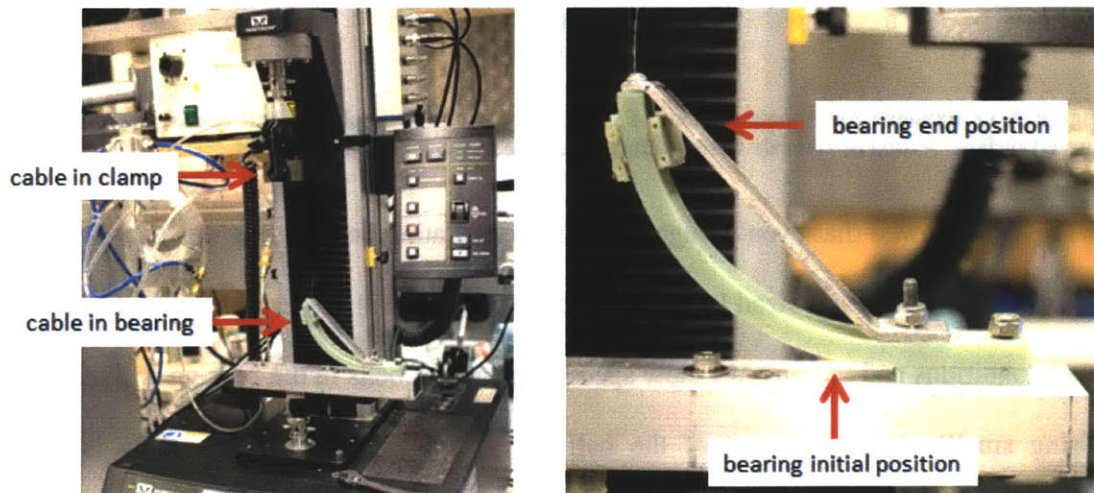


Figure A-11 Force test of the non-recirculation ball bearing on a curved hoop with an Advanced Mechanical Testing System from Instron.

A total of ten trials were performed, with an example plot shown in the Figure A-12. The average force necessary to move the bearing on a curved hoop over all ten trials is about 12.5 N.

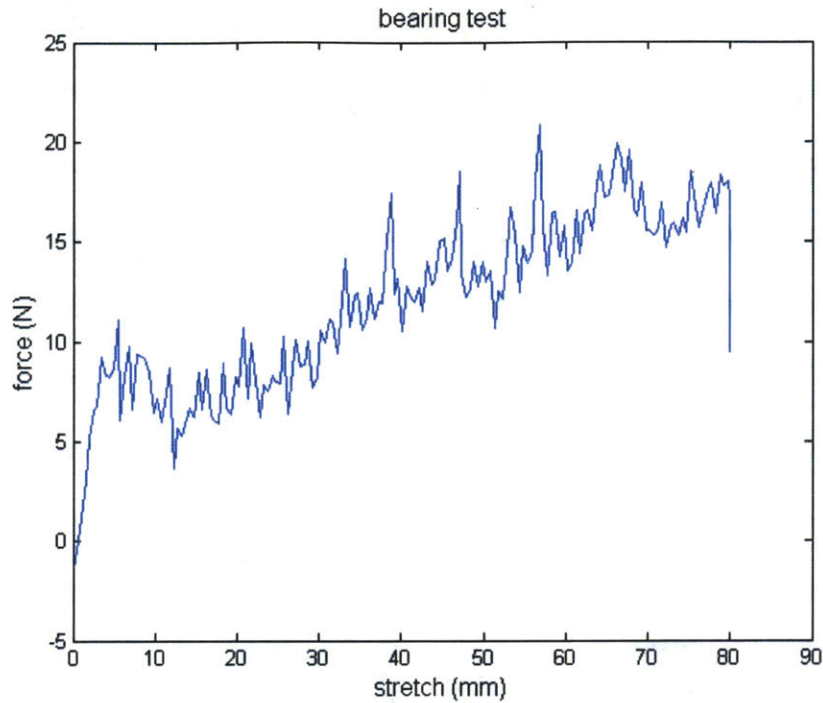


Figure A-12 Example force measurement of the real scale non-recirculating ball bearing traveling on a curved surface. A total of 10 trials were conducted and the average force was 12.5 N.

This test showed that even though the non-recirculating ball bearing design worked on a large scale, the actual sized bearing still does not perform as desired. Even under low-load conditions and moving at a slow speed, slippage of balls in the bearing is significant. Using smaller balls, the part of the ball being constrained by the bearing is larger percentage wise. The balls are therefore more affected by the rough surface finish of the groove and the handmade retainer, resulting in more frequent cycles, observed as high frequency noise as large as 7 N in magnitude in Figure A-12, between rolling and sliding. Uneven preloading and external load distribution may also restrict the rolling movement of the balls. Significant cantilever deflection of the hoop, in addition to change of bearing orientation as it is moves along the arc, further causes increase in force measurement as the bearing is being pulled up the hoop.

One of the purposes of this test is to examine how the cable would work on the hoop when attached to a bearing. During the test, there is a tendency of the cable crossing over to the ball groove. Two out of the ten trials had such problem. When the cable skips to the ball groove, it not only encounters obstacles such as bumps on hoop and the walls of the bearing, but also gets in the way of the balls' motion, resulting in extremely high forces. Solutions to this problem include enclosed cable track, deeper grooves for the track, and further separation between the cable track and the ball groove.

# Appendix B

## KinematicsSimulation.m

```
clear all; close all; clc;
```

```
testfval=[1,1];
```

```
%simulate target points
```

```
while (abs(testfval(1))>1e-10 || abs(testfval(2))>1e-10)
```

```
    targetSimulation;
```

```
    testfval(1)=fval(1);
```

```
    testfval(2)=fval(2);
```

```
end
```

```
%set up probe parameters
```

```
needleD=1.473; %mm
```

```
needleL=175; %mm
```

```
minD=2; %mm
```

```
d=3; %mm, distance between needle tracks
```

```
%optimize targets order so the hoop moves from negative q1 to positive q1
```

```
P1=[x1 y1 z1];
```

```
P2=[x2 y2 z2];
```

```
P3=[x3 y3 z3];
```

```
[P1, P2, P3]=sortMatrix(P1, P2, P3);
```

```
%inverse kinematics to calculate motor angles
```

```
[q11, q12, r1]=inverseKinematics(P1(1), P1(2), P1(3), d, 1);
```

```
[q21, q22, r2]=inverseKinematics(P2(1), P2(2), P2(3), d, 2);
```

```
[q31, q32, r3]=inverseKinematics(P3(1), P3(2), P3(3), d, 3);
```

```
%define insertion point coordinates
```

```
I1=d/sin(q12);
```

```
I3=d/sin(q32);
```

```
%define first insertion point;
```

```
O2=[0 0 0];
```

```
O1=[I1, 0, 0];
```

```
O3=[I3, 0, 0];
```

```
OP1=O1-P1;
```

```
OP2=O2-P2;
```

```
OP3=O3-P3;
```

```
OP12=cross(OP1, OP2);
```

```
OP23=cross(OP2, OP3);
OP13=cross(OP1, OP3);
```

```
n1=OP12/norm(OP12);
n2=OP23/norm(OP23);
n3=OP13/norm(OP13);
```

```
dist1=abs(dot((P1-P2), n1));
dist2=abs(dot((P2-P3), n2));
dist3=abs(dot((P1-P3), n3));
```

### **targetSimulation.m**

```
close all; clear all;
```

```
%define variables
```

```
depthA=30; %mm
```

```
depthB=150; %mm
```

```
diameterA=20; %mm
```

```
diameterB=25; %mm
```

```
maxEdge=5; %mm
```

```
maxDist=17; %mm
```

```
minDist=1.473; %mm
```

```
baseCenter=10; %mm, remote center of motion to skin center distance
```

```
%generate random cancer radius, target to edge distances, target to target
%distances, and first target point depth in mm and first angle in deg(hoop,
%carriage)
```

```
r=(diameterA/2)+(diameterB/2-diameterA/2)*rand;
```

```
a1=maxEdge*rand;
```

```
a2=maxEdge*rand;
```

```
a3=maxEdge*rand;
```

```
d1=minDist+(maxDist-minDist)*rand;
```

```
d2=minDist+(maxDist-minDist)*rand;
```

```
d3=minDist+(maxDist-minDist)*rand;
```

```
h=-((depthA+baseCenter+r)+((depthB+baseCenter-r)-(depthA+baseCenter+r))*rand);
```

```
angle=360*rand;
```

```
%generate first point
```

```
z1d=-(r-a1)+(r-a1)*2*rand;
```

```
z1=h+z1d;
```

```
x1=sqrt(((r-a1)^2-z1d^2)/(1+(tand(angle)^2)));
```

```
y1=x1*tand(angle);
```

```

%generate depth for second point
z2d=-(r-a2)+(r-a2)*2*rand;
z2=h+z2d;

%Solve for target point 2 and 3
x0=[1,1,1,1,1];
options=optimset('display','off','MaxFunEvals',5000,'maxIter',2000);
[x,fval]=fsolve(@getTarget,x0,options,x1,y1,z1,z2,r,a2,a3,d1,d2,d3,h);
x2=x(1);
y2=x(2);
x3=x(3);
y3=x(4);
z3=x(5);

```

### **sortMatrix.m**

```

function [Po1, Po2, Po3]=sortMatrix(P1, P2, P3)

xMatrix=[P1(2)/P1(3), P2(2)/P2(3), P3(2)/P3(3)];
[C, I]=sort(xMatrix);

```

```

switch I(1)
case 1
    Po1=P1;
case 2
    Po1=P2;
case 3
    Po1=P3;
end

```

```

switch I(2)
case 1
    Po2=P1;
case 2
    Po2=P2;
case 3
    Po2=P3;
end

```

```

switch I(3)
case 1
    Po3=P1;
case 2
    Po3=P2;
case 3
    Po3=P3;
end

```

end

### **inverseKinematics.m**

**function** [q1, q2, r]=inverseKinematics(x, y, z, d, track)

rhoop=80; %hoop radius (mm)

rpulley=0.269/2\*25.4; %driving pulley radius (diameter 0.269in)

r=sqrt(x^2+y^2+z^2); %probe reach (mm)

dq2=2\*asind(sqrt(2\*r^2-2\*r\*sqrt(r^2-d^2))/(2\*r)); %compensation angle

q1=atand(y/z)-14; %motor connected to the hoop (deg)

q2=(asind(-x/r)+(track-2)\*dq2)\*rhoop/rpulley; %motor conected to the driving pulley (deg)

# Appendix C

## SampleProjectMain.java

```
package edu.wpi.robotics.aim.sample.gui;

import java.awt.event.ActionEvent;
import java.awt.event.ActionListener;
import java.io.IOException;
import javax.swing.ImageIcon;
import javax.swing.JButton;
import javax.swing.JFrame;
import javax.swing.JPanel;
import net.miginfocom.swing.MigLayout;

// import software for connecting to the MRI compatible controller
import com.neuronrobotics.sdk.common.BowlerAbstractConnection;
import com.neuronrobotics.sdk.network.BowlerTCPClient;
import com.neuronrobotics.sdk.ui.ConnectionDialog;
import com.neuronrobotics.sdk.ui.TCPConnectionPanel;
import edu.wpi.robotics.aim.core.robot.AbstractKinematics;
import edu.wpi.robotics.aim.core.robot.MRIController;

public class SampleProjectMain {

    /**
     * @param args
     */
    public static void main(String[] args) {
        try{
            final SampleGui gui = new SampleGui();
            final JFrame frame = new JFrame();
            JPanel starter = new JPanel(new MigLayout());
            JButton connectReal = new JButton("Connect Robot");
            JButton connectVirtual = new JButton("Connect Virtual");
            connectReal.addActionListener(new ActionListener() {

                @Override
                public void actionPerformed(ActionEvent arg0) {
                    /**
                     * First create the Bowler device connection
                     */
                    TCPConnectionPanel.setDefaultServer("192.168.0.
                    100");
                    System.out.println();
                    BowlerAbstractConnection connection=null;
                }
            });
        }
    }
}
```



```

try {
    connection = new
        BowlerTCPClient("192.168.0.100", 1965);
} catch (IOException e) {
    e.printStackTrace();
}

//Create the controller object
MRIController mcon = new
MRIController(connection);

if(!mcon.connect()){
    throw new RuntimeException("Not a bowler
        Device on connection:" + connection);
}

//Add the controller to the kinematics model
//All access to the robot should now be through the
kinematics is engineering units

AbstractKinematics model = new
SampleProjectKinematicsModel(mcon);

gui.setKinematicsModel(model);

//GUI clean up
frame.pack();
frame.setLocationRelativeTo(null);
}
});

connectVirtual.addActionListener(new ActionListener() {

@Override
public void actionPerformed(ActionEvent arg0) {
    /**
     * First create the Bowler device connection
     */
    gui.setConnection((BowlerAbstractConnection)null
    );
    frame.pack();
    frame.setLocationRelativeTo(null);
}
});

starter.add(connectReal);

```

```

        starter.add(connectVirtual);
        gui.add(starter);
        frame.getContentPane().add(gui);
        frame.setIconImage( new
        ImageIcon(SampleGui.class.getResource("middle.gif")).getImage(
        ));
        frame.setSize(640, 480);
        frame.setDefaultCloseOperation(JFrame.EXIT_ON_CLOSE);
        frame.setLocationRelativeTo(null);
        frame.setVisible(true);

    }catch(Exception ex){
        ex.printStackTrace();
        System.exit(1);
    }
}
}
}

```

### **SampleProjectKinematicsModel.java**

```

package edu.wpi.robotics.aim.sample.gui;

import java.io.InputStream;
import Jama.Matrix;
import com.neuronrobotics.addons.driving.virtual.VirtualGenericPIDDevice;
import com.neuronrobotics.sdk.addons.kinematics.LinkFactory;
import com.neuronrobotics.sdk.genericdevice.GenericPIDDevice;
import edu.wpi.robotics.aim.core.math.Rotation;
import edu.wpi.robotics.aim.core.math.Transform;
import edu.wpi.robotics.aim.core.robot.AbstractKinematics;

public class SampleProjectKinematicsModel extends AbstractKinematics {

    double deg2rad=Math.PI/180;

    public SampleProjectKinematicsModel(InputStream
    configFile,GenericPIDDevice device ){
        super(configFile,new LinkFactory( device));
    }
    public SampleProjectKinematicsModel() {
        this( new VirtualGenericPIDDevice(1000000));
    }
}

```

```

public SampleProjectKinematicsModel(GenericPIDDevice dev){
    this(SampleProjectKinematicsModel.class.getResourceAsStream("Sample
    Kinematics.xml"), dev);
}

```

@Override

```

public Transform forwardKinematics(double[] jointSpaceVector) {
    double x = jointSpaceVector[0];
    double y = jointSpaceVector[1];
    double z = jointSpaceVector[2];

    Matrix rotX= new
    Matrix(Rotation.getRotationX(jointSpaceVector[3]).getRotationMatrix());

    Matrix rotY= new
    Matrix(Rotation.getRotationY(jointSpaceVector[4]).getRotationMatrix());

    Matrix rotZ= new
    Matrix(Rotation.getRotationZ(jointSpaceVector[5]).getRotationMatrix());

    Matrix rotAll = rotX.times(rotY).times(rotZ);

    Transform back =new Transform(x,y,z,new Rotation(rotAll));
    return back;
}

```

@Override

```

public double[] inverseKinematics(Transform cartesianSpaceTransform)throws
Exception {
    double [] inv = new double[getNumberOfLinks()];
    //Dump from cartesian to joint space, used as an example
    inv[0]= cartesianSpaceTransform.getX();
    inv[1]= cartesianSpaceTransform.getY();
    inv[2]= cartesianSpaceTransform.getZ();

    Matrix rotationMatrixArray = new
    Matrix(cartesianSpaceTransform.getRotation().getRotationMatrix());

    //X rotation
    inv[3]=Math.atan2(-rotationMatrixArray.get(1, 2),
    rotationMatrixArray.get(2, 2))*180/Math.PI;
    //Y rotation
    inv[4]=Math.asin(rotationMatrixArray.get(0, 2))*180/Math.PI;

    //Z rotation

```

```

    inv[5]=Math.atan2(-rotationMatrixArray.get(0, 1),
rotationMatrixArray.get(0, 0))*180/Math.PI;

    return inv;
}
}

```

### SampleKinematics.xml

```

<root>
  <link>
    <name>HoopRotation</name>
    <type>pid</type> <!-- Board type used by the LinkFactory -->
    <index>0</index><!-- Board slot A-->
    <scale>0.072</scale><!-- Scaling factor between raw quadrature encoder
units to engineering units, 360deg/(1250tics*4)-->
    <upperLimit>10000000</upperLimit><!-- In encoder units-->
    <lowerLimit>-10000000</lowerLimit><!-- In encoder units-->
    <pGain>0.7</pGain> <!-- PID gains -->
    <iGain>0</iGain>
    <dGain>0</dGain>
    <isInverted>>false</isInverted><!-- convergence/divergence switching-->
    <isLatch>>true</isLatch><!-- Use the latch value at startup-->
    <indexLatch>0</indexLatch><!-- Encoder index offset value -->
    <isStopOnLatch>>false</isStopOnLatch><!-- Tells the controller to stop
the motor when latch value is reached -->
    <homingTPS>500</homingTPS><!-- Velocity in ticks per second to use
during homing procedure-->
    <upperVelocity>1000</upperVelocity><!-- Maximum motor frequency,
DO NOT exceed 3000 -->
    <lowerVelocity>750</lowerVelocity> <!-- Minimum motor frequency,
DO NOT set below 750 -->
  </link>

  <link>
    <name>CarriageRotation</name>
    <type>pid</type> <!-- Board type used by the LinkFactory -->
    <index>1</index><!-- Board slot B-->
    <scale>0.072</scale><!-- Scaling factor between raw quadrature encoder
units to engineering units, 360deg/(1250tics*4)-->
    <upperLimit>10000000</upperLimit><!-- In encoder units-->
    <lowerLimit>-10000000</lowerLimit><!-- In encoder units-->
    <pGain>0.7</pGain> <!-- PID gains -->
    <iGain>0</iGain>
    <dGain>0</dGain>
  </link>

```

```
<isInverted>>false</isInverted><!-- convergence/divergence switching-->
<isLatch>>true</isLatch><!-- Use the latch value at startup-->
<indexLatch>0</indexLatch><!-- Encoder index offset value -->
<isStopOnLatch>>false</isStopOnLatch><!-- Tells the controller to stop
the motor when latch value is reached -->
<homingTPS>500</homingTPS><!-- Velocity in ticks per second to use
during homing procedure-->
<upperVelocity>1000</upperVelocity><!-- Maximum motor frequency,
DO NOT exceed 3000 -->
<lowerVelocity>750</lowerVelocity> <!-- Minimum motor frequency,
DO NOT set below 750 -->
</link>
```

```
<!-- Registration: Transform for Global to robot fiducial -->
```

```
<ZframeToRAS>
  <x>0</x>
  <y>0</y>
  <z>0</z>
  <rotw>1</rotw>
  <rotx>0</rotx>
  <roty>0</roty>
  <rotz>0</rotz>
</ZframeToRAS>
```

```
<!-- Calibration: Transform for robot fiducial to robot zero -->
```

```
<baseToZframe>
  <x>0</x>
  <y>0</y>
  <z>0</z>
  <rotw>1</rotw>
  <rotx>0</rotx>
  <roty>0</roty>
  <rotz>0</rotz>
</baseToZframe>
```

```
</root>
```